# Biophysics of Kinetochore-Microtubule Interaction: Quantitative Measurement of NDC80 Binding in Cell Using FLIM-FRET

# Biophysics of Kinetochore-Microtubule Interaction: Quantitative Measurement of NDC80 Binding in Cell Using FLIM-FRET

A dissertation presented

by

Tae Yeon Yoo

to

John A. Paulson School of Engineering and Applied Sciences

in partial fulfillment of the requirements

for the degree of

Doctor of Philosophy

in the subject of

Applied Physics

Harvard University

Cambridge, Massachusetts

May 2017

*Dissertation Advisor:*
**Professor Daniel J. Needleman**

*Author:*
**Tae Yeon Yoo**

**Biophysics of Kinetochore-Microtubule Interaction:
Quantitative Measurement of NDC80 Binding in Cell Using FLIM-FRET**

## Abstract

Chromosome motion during cell division is driven by coupling the dynamic ends of microtubules to the kinetochore. Erroneous kinetochore-microtubule attachments frequently occur in early mitosis, but are corrected to prevent chromosome mis-segregation. However, the mechanisms of kinetochore-microtubule coupling and error correction remain poorly understood. The NDC80 complex is the predominant coupler of the kinetochore to microtubules, and is thus directly implicated in these mechanisms. The lack of techniques to quantify the attachment of the NDC80 complex to microtubules in vivo has been a major obstacle to investigate this possibility. Here, I present a method that utilizes on cell engineering, Förster resonance energy transfer measurement by fluorescence lifetime imaging microscopy (FLIM-FRET), and Bayesian analysis, for quantitative measurement of the fraction of NDC80 complexes bound to microtubules at individual kinetochores in living cells. Using this method, I found that Aurora B kinase modulates the attachment of NDC80 to kinetochore microtubules (kMTs) in a graded fashion in vivo, and that the NDC80 attachment increases from prometaphase to metaphase in the course of error correction. Measurements of NDC80 binding at the kinetochores oscillating around metaphase plate demonstrated that NDC80 complex preferentially associates with polymerizing kMTs, and that the fraction of NDC80 bound increases with the distance between sister kinetochores, a proxy for centromere tension. The positive correlation was dependent on the haspin-dependent localization of Aurora B kinase at the centromere. Taken together, these results argue that tension-dependent phosphoregulation of NDC80 by centromere-localized Aurora B is the basis of chromosome

autonomous error correction. We believe that this FLIM-FRET technique is a powerful tool to further dissect the molecular mechanisms of kinetochore function.

# Contents

# List of Tables

# List of Figures

# Acknowledgments

I would like to start by thanking my mom and dad. Without their unconditional love, support, encouragement, and sacrifice, I wouldn't have made it this far. I want to thank my wife, Juhyun, for always being with me when I struggle, empathizing with me, sharing wisdom and experiences, keeping me away from bad decisions, and encouraging me to be a better person. I am also thankful to have an amazing sister, Jungmin.

I am grateful to Bumjin, Changwook and Jihyun! The memories I have made with them during graduate school are unforgettable. I'd also like to thank all the Needleman lab members. Thanks Peter and Bryan for being amazing classmates, colleagues, and friends. It was a great fun to work with Che-hang, Maya, Hai-yin, Reza, Bez, and Tim. Thank Frank for all the administrative helps.

I thank Dan so much for being an amazing advisor for the last six years. He has influenced me in many ways to become a grown up scientist. He gave me enormous supports and advices on my research and careers. His enthusiasm always motivated me, and the way he approaches science inspired me. I'm very thankful that I chose the right advisor and the right place.

I thank Jennifer DeLuca, Luke Lavis, Mike Lampson, Iain Cheeseman for generously sharing useful reagents, and Samsung Scholarship for financially supporting my graduate studies for five years. Finally, I would like to thank Tim Mitchison, Iain Cheeseman, and Vinothan Manoharan for being my dissertation committee and giving me the friendly guidance on my research and career, and writing the recommendation letters for me.

To my wife and parents.

# Chapter 1

# Introduction

> The dream of every cell is to become two cells.
>
> *François Jacob*

We human beings all start as a single cell. Through numerous rounds of cell division, a process called mitosis, we become a cluster of tens of trillions of cells (Bianconi *et al.*, 2013). Cell division continues throughout our lives to grow, to develop, to reproduce, and to compensate for cell loss caused by damages and aging. During an average lifespan of human, the cells in the body cummulatively undergo approximately $10^{16}$ cell divisions. For us to maintain healthy lives, each round of cell division must be flawless.

During mitosis of a human cell, each of 46 chromosomes must be cleaved into two identical chromatids, and allocated equally to each daughter cell through a process called chromosome segregation. The consequence of chromosome mis-segregation results in aneuploidy, the state in which a cell has abnormal number of chromosomes. Aneuploidy is believed to entail cancer, infertility, and many genetic diseases (Santaguida and Amon, 2015; Gordon *et al.*, 2012a; Rajagopalan and Lengauer, 2004). For such reason, chromosome segregation must be carefully governed.

The motion of chromosomes is governed by a football-shaped cellular apparatus named spindle. Spindle mainly consists of microtubules (MTs), long tubular polymers of tubulins

that dynamically switch between polymerization and depolymerization state. Chromosomes are congressed (in metaphase) and segregated (in anaphase) by the interaction with microtubules. The interaction between chromosome and microtubules is predominantly mediated by kinetochore, a protein machinery built on the centromere, where two identical sister chromatids are joined together resulting chromosome in the X-shaped structure of chromosomes. The microtubules interacting with the kinetochore are referred to as kinetochore microtubules (kMTs), the number of which is approximately 15-20 kMTs per kinetochore in human cells.

The main questions of this dissertation are 1) how kinetochore drives the movement of chromosome, and 2) how the kinetochore-microtubule interaction is regulated to ensure faithful chromosome segregation. The following sections will review the prior studies on kinetochores that provided insights into these questions and motivated this work.

## 1.1 Kinetochore: Structure and Functions

Kinetochore serves two roles indispensable to successful cell division: first, it acts as a localization site of biochemical signals including that of spindle assembly checkpoint (SAC), a cell cycle surveillance pathway that delays chromosome segregation until every chromosome gains proper interaction with microtubules (Musacchio and Salmon, 2007), and that of kinetochore error correction mechanism. Second, kinetochore provides a physical link between centromere and the dynamic ends of kinetochore microtubules, thereby driving the motion of chromosomes. These two functions are closely related to each other; SAC is activated by the kinetochores lacking microtubule attachment or tension (Musacchio and Salmon, 2007), and on the other hand, kinetochore attachment is regulated by the Aurora B kinase concentrated at the centromere (Lampson and Cheeseman, 2011).

Kinetochore is a hierarchical protein complex composed of nearly hundred different types of proteins. Electron microscopy revealed that kinetochores have a multi-layered structure, leading to the division of the kinetochore into distinct regions: the *inner kinetochore*, which forms the interface with chromatin; *outer kinetochore*, which forms the interaction

surface for spindle microtubules; and *inner centromere*, which refers to the chromatin that is located between the two sister kinetochores (Cheeseman and Desai, 2008; McEwen *et al.*, 2007; Brinkley and Stubblefield, 1966). A combination of immunofluorescence-based screening of antibodies, genetics, RNA interference (RNAi)-based screens, biochemistry, and mass-spectrometry-based proteomics have determined a large number of proteins that function at kinetochore, and have grouped the kinetochore proteins into defined subcomplexes (Earnshaw and Rothfield, 1985; Yen *et al.*, 1991; Cooke *et al.*, 1987; Cheeseman *et al.*, 2006; Obuse *et al.*, 2004; Wigge and Kilmartin, 2001). In this study, I will introduce and focus on two kinetochore protein subcomplexes that play major roles in kinetochore-microtubule attachment and its regulation: NDC80 complex and chromosomal passenger complex (CPC), particularly Aurora B kinase.

### 1.1.1 NDC80 Complex: kinetochore-microtubule coupler

Nuclear division cycle 80, or NDC80 complex is a four-protein complex composed of Ndc80p[1], Nuf2p[2], Spc24p, and Spc25p[3]. With kinetochore null protein 1 (KNL1) and mis-segregation 12 (MIS12) complex, NDC80 complex form a kinetochore machinery referred to as the KMN network, which is essential for the attachment of microtubule plus-ends to kinetochores. Close homologs of the proteins in NDC80 complex are found in all eukaryotes examined so far, from yeast to humans (Wigge and Kilmartin, 2001; Howe *et al.*, 2001; Zheng *et al.*, 1999; Bharadwaj *et al.*, 2004; McCleland *et al.*, 2004), implicating a crucial role of NDC80 in the kinetochore-microtubule attachment mechanism across different species.

Biochemical methods and electron microscopy revealed that NDC80 complex is a long rod[4] with globular "heads" at either end of an $\alpha$-helical coiled-coiled shaft. Ndc80p and Nuf2p contribute to one head mediating microtubule binding and to the intervening shaft;

[1]It is also called Hec1p in humans, which stands for 'highly expressed in cancer'.

[2]Stands for 'nuclear filament-containg protein'.

[3]Stands for 'spindle pole component'.

[4]The length of the NDC80 complex is measured to be 51 nm (Wei *et al.*, 2005).

and Spc24p and Spc25p complete the shaft and contribute to the other head toward the centromere mediating kinetochore association (Cheeseman *et al.*, 2006; Wei *et al.*, 2005; DeLuca *et al.*, 2006; Ciferri *et al.*, 2008b). Both Ndc80p and Nuf2p have CH domain at their N-termini, which is present in other microtubule binding proteins such as EB1 (Slep and Vale, 2007), suggesting their capability of directly binding to microtubules. Indeed, the Ndc80p/Nuf2p head of NDC80 complex binds the microtubule with a tubulin monomer repeat, recognizing $\alpha$- and $\beta$-tubulin at both intra- and inter-tubulin dimer interfaces, revealed by biochemical assays and subnanometer-resolution cryo-EM reconstruction of the human NDC80 complex bound to microtubules (Alushin *et al.*, 2010; Cheeseman *et al.*, 2006; Wilson-Kubalek *et al.*, 2008; Sundin *et al.*, 2011). The unstructured, positively charged 80-amino-acid N-terminal tail of the Ndc80p was found to be required for high-affinity microtubule binding, presumably by the interaction with the negatively charged C-terminal tails of tubulins, or 'E-hooks' (Cheeseman *et al.*, 2006; DeLuca *et al.*, 2006; Ciferri *et al.*, 2008b; Guimaraes *et al.*, 2008; Miller *et al.*, 2008).

The N-terminal tail of the Ndc80 protein contains multiple phosphorylation sites of Aurora B kinase[5]. Previous studies with purified NDC80 complexes in vitro demonstrated that the Ndc80 tail can modulate the NDC80-MT binding; multiple phosphorylations or introduction of phosphomimetic substitutions[6] reduce the binding affinity of NDC80 complexes for MTs in a graded fashion. The phosphorylation of Ndc80p tail changes over time during mitosis; in early mitosis the tail is heavily phosphorylated, and the phosphorylation decreases down to zero to one phosphate in metaphase (Zaytsev *et al.*, 2014), suggesting that the phosphoregulation of Ndc80p by Aurora B is involved in the regulation of kinetochore-MT attachment during mitosis. However, the molecular mechanism of the phosphoregulation of the NDC80 complex binding still remains unclear.

[5]nine phosphorylation sites mapped in vitro, six sites have been confirmed to be phosphorylated in vivo (DeLuca *et al.*, 2006; Ciferri *et al.*, 2008b)

[6]Phosphomimetics are the amino acid substitutions that mimics a phosphorylated protein. Aspartic acid was used as a phosphomimetic substitution of phospho-serine in the Ndc80 tail.

### 1.1.2 Aurora B kinase: key regulator of mitosis

Aurora B is one of the most intensively studied kinases, and is essential for accurate cell division (Adams *et al.*, 2000; Kaitna *et al.*, 2000). In conjunction with the three regulatory and targeting components — borealin, survivin, and INCENP[7] — the enzymatic component Aurora B forms chromosomal passenger complex (CPC). Like NDC80 complex, CPC is also well-conserved throughout eukaryotes from yeast[8] to human. The phosphorylation of Aurora B substrates is involved in several important process in mitosis including: chromosome condensation, correction of erroneous kinetochore-microtubule attachments, activation of SAC, and cytokinesis (Carmena *et al.*, 2012).

The localization of Aurora B changes dynamically in the course mitosis. From prometaphase to metaphase, CPC is enriched at centromere, and this enrichment requires the mitosis-specific phosphorylation of two histone tails: histone H3T3 by haspin kinase (Kelly *et al.*, 2010; Wang *et al.*, 2010) and histone H2AT120[9] by Bub1 kinase (Yamagishi *et al.*, 2010). Phosphorylated H3T3 is enriched along the length of chromosomes between paired sister chromatids, but is the most prominent at the inner centromere, as it is generated by haspin kinase associated with cohesin. Phosphorylated H3T3 provides a binding site for survivin, thereby recruiting CPC to the inner centromere. Phosphorylated H2AT120, on the other hand, is enriched near the kinetochores since Bub1 kinase is recruited by KNL1 (which is a part of KMN network) through direct association (Yamagishi *et al.*, 2012). Shugoshins Sgo1 and Sgo2 are recruited to phosphorylated H2AT120, and in turn promotes the targeting of the CPC to the centromeres through borealin[10] phosphorylated by Cdk1 (Tsukahara *et al.*, 2010).

At the onset of anaphase, the CPC relocates from the centromeres to the central spindle through the interaction with Mklp2 (mitotic kinesin-like protein 2), a kinesin-6 that binds

[7] inner centromere protein

[8] In yeast, Aurora B is called Ipl1p, which stands for "increase in ploidy".

[9] H2AS121 in fission yeast

[10] survivin in fission yeast

microtubules at the central spindle (Gruneberg *et al.*, 2004). This localization is responsible for the formation of CPC substrate phosphorylation gradient at anaphase (Tan and Kapoor, 2011), which is supposedly important in coordinating the spatio-temporal dynamics needed for successful anaphase and cytokinesis.

Aurora B can activate itself *in trans* via phosphorylation of its activation loop and of a conserved TSS motif in the C-terminus of INCENP (Bishop and Schumacher, 2002; Honda *et al.*, 2003; Sessa *et al.*, 2005; Zaytsev *et al.*, 2016). Conversely, phosphatase inactivates Aurora B by deposphorylating Aurora B and INCENP. The localization density and the interaction with phosphatase are, therefore, closely related to the activity of Aurora B and its spatio-temporal dynamics.

## 1.2 Kinetochore-microtubule Attachment

Broadly speaking, kinetochore-microtubule attachment is classified into two categories: lateral attachment and end-on attachment. Lateral attachment refers to the state in which a kinetochore is attached to the side wall of microtubule. Lateral attachment happens frequently, but briefly observed in prometaphase when the spindle is not fully formed and the chromosomes are dispersed. Previous studies suggested that centromere-associated protein E (CENP-E), a kinesin-like motor protein, delivers the laterally attached kinetochore to the plus-end of microtubule, and then converts the lateral attachment to end-on attachment. This process is thought to play an important role in chromosome congression at the spindle equator (Kapoor *et al.*, 2006).

End-on kinetochore-MT attachment has been extensively studied, but it is still unclear how kinetochore couples the force generation to the dynamics of kMT plus ends. It is common that intracellular force is generated by ATP-consuming motor proteins walking on the cytoskeleton. However, that is not the case for the force generated by MT ends attached to kinetochore; chromosomes are pulled by the shortening end of microtubules even in the absence of ATP in vitro (Coue *et al.*, 1991; Koshland *et al.*, 1988), and the deletion or depletion of the motor proteins does not detach the chromosomes from the MTs (Grishchuk

and McIntosh, 2006). A major question is the mechanism by which the kinetochore-MT "couplers" attached to the microtubules translates MT depolymerization into work. Two classes of models have been proposed: conformational wave model and biased diffusion model.

In the conformational wave model, the conformational change in the depolymerizing plus ends directly produces a poleward "power stroke" on the kinetochore (Mitchison, 1988; Koshland *et al.*, 1988; Asbury *et al.*, 2011). In this model, kinetochore uses the strain energy in the tubulin dimer produced by hydrolysis of GTP that is stored in the microtubule lattice and only released at the depolymerizing plus end of microtubule. Initial enthusiam for this model comes from the cryo-EM studies showing that the protofilaments of disassembling microtubule are curled inside out (Mandelkow *et al.*, 1991; Tran *et al.*, 1997) due to the conformation change in GDP-tubulin. A theoretical work predicted that the maximal force generated by the conformational change is $\approx 75pN$ per MT (Molodtsov *et al.*, 2005), suggesting that only ≈10 MTs are required to achieve the chromosome stall force of 700 pN measured in a grasshopper meiotic cell in anaphase (Nicklas, 1983).

The conformational wave model requires kinetochore-MT couplers with high affinity for MTs which can withstand and transmit such high force. Dam1 protein has been proposed as a candidate for such strong kinetochore-MT coupler, based on the discoveries that (1) Dam1 protein purified from the kinetochores of budding yeast oligomerizes to form a ring around the MTs (Miranda *et al.*, 2005; Westermann *et al.*, 2005); (2) it can processively track the disassembling tip of the MT in vitro (Westermann *et al.*, 2006); and (3) it can harness the microtubule dynamics to produce force alone (Akiyoshi *et al.*, 2010), and cooperatively with Ndc80 complex (Asbury *et al.*, 2006). Metazoan homolog of Dam1 complex has not been identified, but Ska1 has been suggested to play the corresponding role in vertebrate kinetochore-microtubule interaction (Welburn *et al.*, 2009). Whether Dam1 can form the same ring structure in cell, and how this ring is physically connected to other kinetochore components are still under investigation.

In the biased diffusion model, on the other hand, the kinetochore has weakly binding

couplers that bind and unbind on the microtubule rapidly, and the force is generated by energetics involved with maximizing the number of weak attachment sites (Hill, 1985). This model is based on the assumption that the diffusion of the couplers is fast and the total binding energy of the couplers is large enough. NDC80 complex is a strong candidate for the coupler in the biased diffusion model, since there is a large number of NDC80 complexes per kinetochore in human cell (estimated to be $\sim 244$ (Suzuki *et al.*, 2015)); NDC80 complex in vitro displays random walk on the MT away from the tip; and can form a load-bearing attachment to the disassembling MT tip (Powers *et al.*, 2009).

The discovery of Dam1 structure in vitro stimulated the enthusiasm for the conformational wave model. In the same sense, the biased diffusion model earned supports from the studies of ultrastructure of kinetochores in cells (McEwen and Dong, 2010; Dong *et al.*, 2007). However, the knowledge in the structure doesn not answer the mechanistic question of how the kinetochore-MT coupling is achieved. For example, even though Dam1 ring is very convenient in the conformational wave model, it is also equally likely that this ring produces force through biased diffusion. Conversely, the absence of Dam1 ring structure does not rule out the conformational wave model, since any strong coupler in any structure can serve as a power stroke transmitter.

The key factor that discriminates two models is therefore not the structure of the coupling machinery, but the dynamics of binding and unbinding of the couplers at the interface of kinetochore-MT interaction. In the biased diffusion model, the dynamics must be fast enough that the couplers may do random walk on the MTs. In the conformational wave model, on the other hand, the dynamics needs to be slow enough to efficiently transmit the force generated by conformational change to the kinetochore and to the chromosome. This dissertation introduces a novel technique to monitor the dynamics of the couplers' binding and unbinding, which would resolve the controversies over the kinetochore-MT coupling mechanism.

## 1.3 Regulation of Kinetochore-microtubule Attachment

Different types of end-on attachment occurs in mitosis. These include: *monotelic attachment* (in which one kinetochore is attached to a spindle pole while its sister is unattached), *syntelic attachment* (in which both kinetochores are attached to the same spindle pole), and *merotelic attachment* (in which one kinetochore is attached to both poles), and *amphitelic attachment* (or biorientation, in which each kinetochore is attached to each spindle pole). Among these, only amphitelic attachment is regarded as correct attachment, and the others are regarded as erroneous attachments, which frequently occur in prometaphase but are corrected to amphitelic attachment by the dynamic turnover of kinetochore-MT attachments. If not fixed before the anaphase onset, the erroneous attachments may cause chromosome missegregation, leading the daughter cells to aneuploidy. The mechanism by which kinetochore-microtubule attachments are regulated to fix the erroronenous attachments is highly controversial.

It has been proposed that individual chromosome autonomously stabilizes the correct bi-oriented attachments and destabilizes erroneous attachments, and that tension across the centromere provides a mechanism to discriminate between correct and erroneous attachments (Nicklas and Ward, 1994; Liu *et al.*, 2009; Welburn *et al.*, 2010; Lampson and Cheeseman, 2011). This concept was first motivated by Bruce Nicklas's finding of tension dependency of kinetochore-MT attachment (Nicklas and Koch, 1969); his classic micromanipulation experiments with grasshopper spermatocyes demonstrated that artificial tension applied to chromosomes maintains the erroneous syntelic attachments over 5 hours, which in the absence of tension are corrected to bi-orientation within 16 minutes. Tension-dependency of kinetochore-MT attachment was also demonstrated by in vitro optical tweezer assay (Akiyoshi *et al.*, 2010). Tension is greater across the centromere in bi-oriented attachments than erroneous attachments because sister kinetochores are being pulled towards opposite spindle poles. Therefore, these findings naturally led to the rise of the "tension-sensing error correction model", which states that kinetochore-MT attachment errors are corrected by selectively destabilizing erroneous attachments under lower tension while stabilizing proper attachments under higher tension.

The centromere-localization of Aurora B (see 1.1.1 and 1.1.2) has been proposed to be responsible for the tension-dependent kinetochore-MT attachment. Even though this possibility has not been explicitly proved, the finding that Aurora B differentially phosphorylates the substrates in the kinetochore depending on the physical position of the substrate relative to Aurora B localization site offered support for the possibility (Welburn *et al.*, 2010; Liu *et al.*, 2009; Salimian *et al.*, 2011). This finding led to 'spatial separation' model in which the force exerted on bi-oriented kinetochores extends the centromere and kinetochore, positioning the Aurora B substrates (including Ndc80 protein) in the outer kinetochore away from the Aurora B localization site, and therefore stabilizing the kinetochore-MT attachment.

The spatial separation model as well as tension-dependent regulation mechanism is still debatable. It has been shown that the removal of Aurora B by truncating INCENP subunit in budding yeast nevertheless supports proper chromosome segregation (Campbell and Desai, 2013), proposing that tension induces the change in the structure of kinetochore and the accessibility of the Aurora B substrates. Moreover, measurements of fluorescence dissipation after photoactivation has shown that the turnover of kinetochore microtubules is independent of the attachment state of kinetochores, but changes in a coordinated manner among all chromosomes during phase transitions in mitosis (Kabeche and Compton, 2013), which argues against the tension-dependent regulation. Furthermore, there is no evidence to indicate that centromere 'breathing' associated the chromosome oscillations in metaphase alters the kinetochore-MT attachment as centromere distance transiently lengthens and shortens.

Recent studies suggested other error correction models involving Aurora A (Ye *et al.*, 2015) and cyclin-CDKs (Kabeche and Compton, 2013), but the number of supporting evidences is small relative to the Aurora B-dependent models yet.

## 1.4 Contents of this dissertation

One of the greatest difficulties in investigating the kinetochore-microtubule attachment and its regulation has been the limitation of current experimental approaches: in vitro

biochemical assays are informative, but extrapolating the obtained results to understand in vivo behaviors can be challenging; in vivo measurements have been highly indirect, making their interpretation contingent on myriad assumptions that are difficult to verify.

In this dissertation, I present a method that fulfills the deficiencies of previous approaches by providing real-time quantitative measurement of the binding of NDC80 to microtubules at individual kinetochores in human tissue culture cells. This interdisciplinary method combines the use of fluorescence lifetime imaging microscopy (FLIM), Bayesian statistical analysis, and CRISPR engineered cell lines. In Chapter 2, I introduce FLIM and exaplain how FLIM is utilized to quantify Förster Resonance Energy Transfer (FRET) in the study of kinetochores in live human cells in culture. Estimating the parameters of interest from FLIM data with fewer number of photons is difficult, but unavoidable when the measurement is intended for obtaining high spatio-temporal information from biological sample. Conventional curve fitting alorithms produce significant bias in the estimation when stochastic noise in the FLIM data is significant. For that reason, I developed Bayesian statistical analysis of FLIM data. Chapter 3 describes Bayesian analysis of FLIM data, and demonstrates its capability of analyzing FLIM data with superior accuracy when there is fewer number of photons. Chapter 4 demonstrates the application of FLIM-FRET in measuring NDC80 attachment to MTs, and presents my results about how the NDC80 attachment is regulated in human tissue culture cell.

# Chapter 2

# Studying kinetochores using live-cell FLIM-FRET[1].


## Abstract

Kinetochores play essential roles in coordinating mitosis, as a mechanical connector between chromosome and microtubule and as a source of numerous biochemical signals. These mechanical and biochemical behaviors of kinetochores change dynamically in cells during mitosis. Therefore, understanding kinetochore function requires an imaging tool that quantifies the protein–protein interactions or biochemical changes with high spatiotemporal resolution. FRET has previously been used in combination with biosensors to probe protein–protein interactions and biochemical activity. In this chapter, we introduce FLIM-FRET, a lifetime-based method that quantifies FRET, and describe the use of FLIM-FRET as a method for studying dynamic kinetochore behavior in cells with high spatiotemporal resolution.


[1]Reprinted from Yoo and Needleman (2016)

## 2.1 Introduction

During mitosis, normally functioning eukaryotic cells rapidly and accurately segregate their chromosomes. Inaccurate chromosome segregation gives rise to aneuploidy, which can lead to cancer and death (Gordon *et al.*, 2012b; Rajagopalan and Lengauer, 2004). The proper attachment of microtubules to chromosomes is necessary for accurate chromosome segregation (Bakhoum *et al.*, 2009; Cimini and Degrassi, 2005). The interaction between chromosomes and microtubules is predominately mediated by the kinetochore, a highly complex protein structure located at the centromeric region of each chromatid. The main functions of kinetochores can be divided into two parts: attachment and signaling. The kinetochore can attach to microtubules even as the microtubules dynamically switch between growth and shrinking phases. These attachments can withstand significant tension, and therefore provide the physical linkage and coupling between microtubules and chromosomes (Nicklas, 1983; Inoué and Salmon, 1995). The kinetochore is also a source and target of a myriad of regulatory biochemical signals required for the correction of erroneous kinetochore-microtubule attachments and the spindle assembly checkpoint (Li and Murray, 1991; Musacchio and Salmon, 2007; Godek *et al.*, 2014a). Though both of these main functions of kinetochores are very important and have been studied extensively, many aspects of their function and behavior remain poorly understood. One difficulty is a lack of methods for measuring biochemical activities at kinetochore with high temporal and spatial resolution.

Förster Resonance Energy Transfer (FRET) has been widely used as a probe for protein-protein interactions and protein activity in vivo. FRET is the process in which a donor fluorophore transfer the energy from its excited state to an acceptor fluorophore a few nanometers in proximity to the donor. In order to utilize FRET as a probe for protein-protein interaction, one protein of interest is labeled with a donor fluorophore, and the other with an acceptor fluorophore (Figure 2.1). FRET can also be used to measure enzyme activity, by adopting FRET biosensors engineered to undergo a conformational change upon the modification by the enzyme of interest, which leads to a change in intra-molecular FRET (Figure 2.1). Many types of FRET biosensors have been developed and used in a variety of

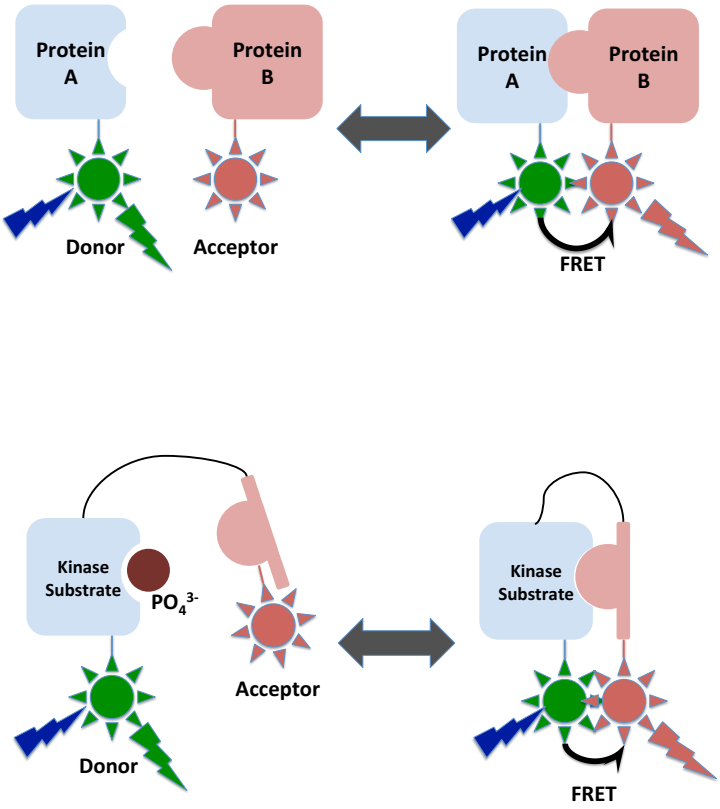


**Figure 2.1:** *The usages of FRET for studying (top) protein–protein interaction using fluorophore-labeled proteins, and (bottom) kinase activity using engineered FRET bio-sensor*

cell biology studies (Violin *et al.*, 2003; Chen *et al.*, 2014; Espenel *et al.*, 2013; Pereira *et al.*, 2011; Gavet and Pines, 2010; Fuller *et al.*, 2008).

There are two widely used approaches to measure FRET: intensity-based and lifetime-based approaches. Intensity-based approaches include sensitized emission measurements and acceptor photobleaching methods. Though the sensitized emission measurement is the simplest assay to perform, a major limitation is the requirement of complicated correction and normalization procedures and the dependence on the relative concentration of donor and acceptor fluorophores, which is hard to control in practice. The acceptor photobleaching method, on the other hand, doesn't require the complicated correction procedures, but is difficult to use for time-varying measurements, and is also prone to artifacts due to the motion of acceptors and photodamage from the use of high intensities required for photobleaching. Therefore, this method is not suited for the study of dynamic kinetochores.

Fluorescence Lifetime Imaging (FLIM) provides a lifetime-based approach to measure FRET (Festy *et al.*, 2007). The fluorescence lifetime refers to the average time that a fluorophore spends in the excited state before relaxing and emitting a photon. The lifetime depends on both its intrinsic photo-physical properties and on its microenvironment, including the local pH, temperature, viscosity, and the presence of quenching, such as by FRET. FLIM-FRET is an imaging and analysis technique that probes fluorophores' lifetimes and quantifies FRET using the measured lifetimes. FLIM-FRET provides a highly quantitative measure of FRET, which is difficult to achieve with intensity-based measurements, because FLIM-FRET uncouples two factors that contribute to the overall FRET signal: the FRET efficiency of an individual FRET pair and the number of FRET pairs. Moreover, FLIM-FRET doesn't require irreversible reaction, such as acceptor photobleaching, and combined with Bayesian analysis, it is capable of measuring FRET with a high spatio-temporal resolution. These advantages make FLIM-FRET suitable for the study of dynamic kinetochores in live cell.

Here we describe the Bayesian analysis of FLIM-FRET as a tool to study kinetochore function in live cell at up to sub-millisecond time scales with single kinetochore resolution.

## 2.2 Materials

### 2.2.1 Fluorescence Lifetime Imaging (FLIM)

There are several variants of FLIM, which differ in how the fluorescence lifetime is measured and fluorophores are excited. We use time-domain FLIM (vs. frequency-domain) for more straightforward analysis, and two-photon excitation (vs. single-photon excitation) for the flexibility and low photon-induced damage.

(a) Femtosecond Ti:sapphire pulse laser (Mai Tai DeepSee, Spectral Physics)

In time-domain FLIM, an ultrashort pulsed laser is used as an excitation light source. The desired period of the laser is ≈10 ns so that the nanosecond-scale fluorescence decay is well captured in a single laser period. Ti:sapphire lasers are particularly convenient when used for two-photon excitation because they are tunable between 690 nm to 1040 nm, allowing for the use of many different fluorophores.

(b) Time-Correlated Single Photon Counting module (SPC-150, Becker & Hickl GmbH)

Time-Correlated Single Photon Counting (TCSPC) is a technique that detects a single photon and measures the timing of the photon arrival with picosecond time resolution. 16 TCSPC determines the time between the laser pulse and the arrival of the emitted photon at the detector, for each photon detected. After accumulating a number of photons, their arrival times can be used to construct a histogram, called the 'fluorescence decay' or 'FLIM curve'. (Figure 2.2)

(c) Laser scanning system (DCS-120, Becker & Hickl GmbH)

(d) Detector (HPM-100-50, Becker & Hickl GmbH)

Time-domain FLIM requires detectors with single-photon sensitivity and fast response.

(e) Optics

All the optics in the excitation light path, including the objective, lenses, and mirrors should be suitable for near-infrared wavelength pulsed laser. For the study of kinetochores, an objective with high Numerical Aperture (NA) is highly preferred because

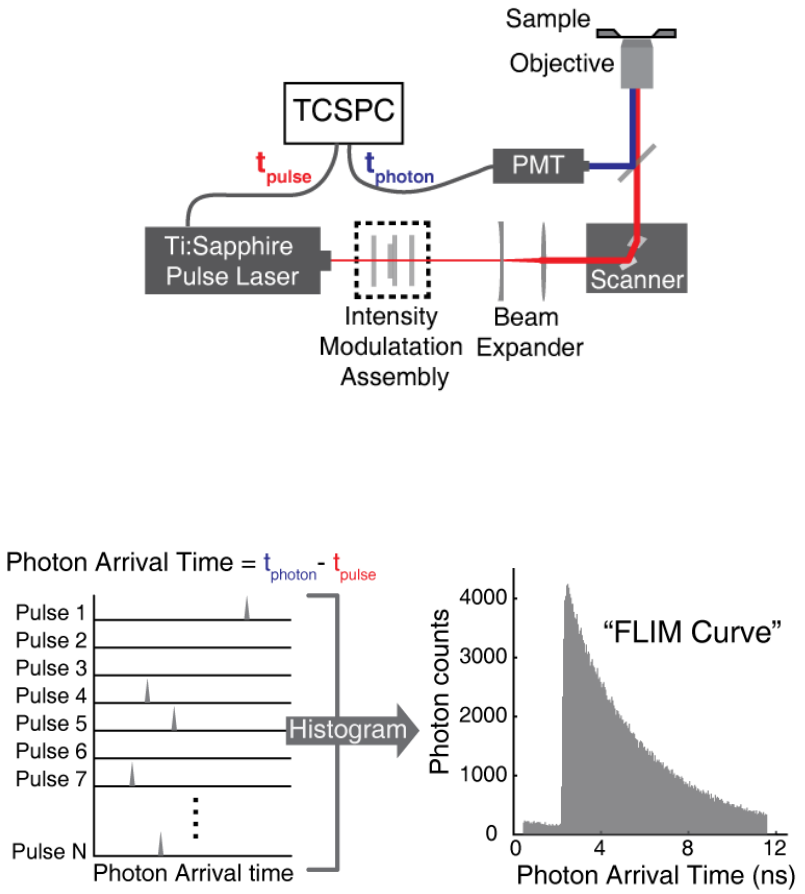


**Figure 2.2:** *(top) Arrangement and connections of major components in FLIM system. Red and blue arrows indicate the path of the excitation laser beam and that of emission photon, respectively. (bottom) Construction of FLIM curve by TCSPC*

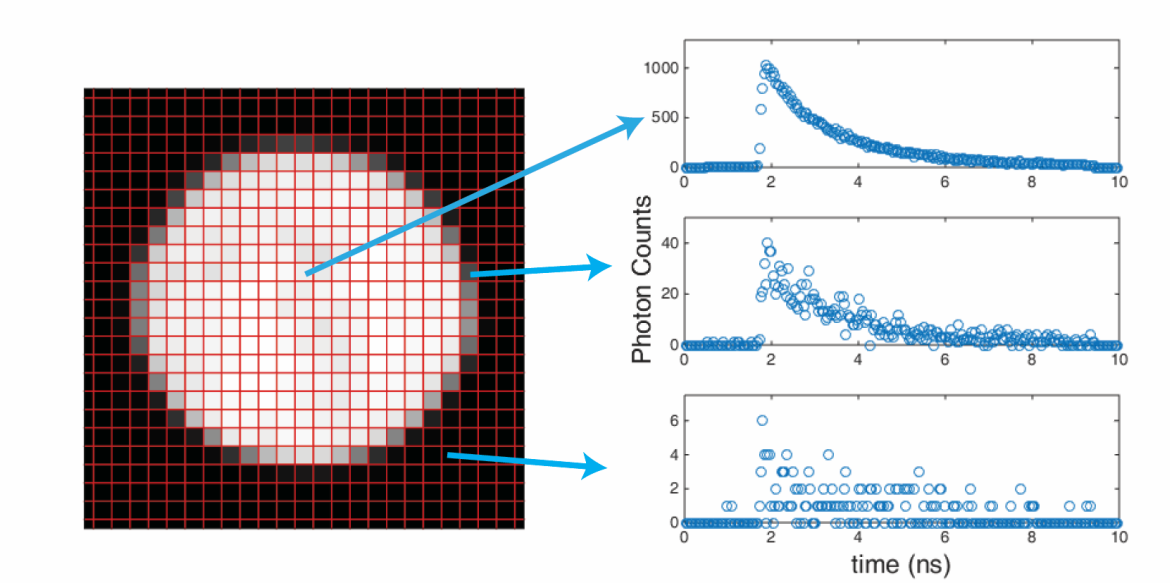


**Figure 2.3:** *Example of FLIM image. (left) Intensity image obtained by integrating FLIM curve at each pixel over the arrival time. (right) FLIM curves at three different pixels with different number of photons*

it allows a more compact point spread function (PSF), which results in better spatial resolution as well as more efficient two-photon excitation. It is also necessary to have appropriate optics to modulate the excitation intensity. This can be achieved by the combination of polarization optics, neutral density filters, or opto-electronic elements such as a Pockels cell.

(f) FLIM software (SPCM, Becker & Hickl GmbH)

To generate a FLIM image, FLIM software, either custom built or purchased, controls the scanning of the excitation laser over the region of interest and the pixel location and records the arrival time of each emitted photon using TCSPC. A FLIM curve is then generated for each pixel in the image (Figure 2.3). These FLIM curves could be analyzed separately or photons from multiple pixels, such as all the pixels from a given kinetochore, could be grouped and analyzed together.

### 2.2.2 Mitotic Live Cell Imaging

We use U2OS tissue culture cells, but the protocol can be generalized to any type of cells.

(a) Imaging media (FluoroBrite™ DMEM, Life Technology)

Imaging media should be carefully selected such that it does not contain significant autofluorescence, while still ensuring cell viability during imaging. The amount of serum should be reduced to a minimal amount, and vitamins such as riboflavin and pyridoxal can be removed completely (Bogdanov *et al.*, 2012). Imaging media suited to human tissue culture cells is commercially available. If $CO_2$ control is unavailable, the imaging media should be supplemented with 10 mM HEPES to buffer the cells against changes in the pH.

(b) Sample coverglass (GG-25-pdl, Neuvitro)

Poly-D-lysine coating enhances the attachment and viability of adherent tissue culture cell.

(c) Temperature-controlled microscope sample chamber

We use an open microscope chamber that has electrical temperature control and an aperture where 25 mm round coverglass can be mounted.

(d) Objective heater (Bioptechs)

Objective Z-stage (PIFOC, Physik Instrumente), if 3D imaging is needed.

## 2.3 Methods

We will briefly describe the instrumentation, protocol, and analysis for FLIM-FRET measurement of kinetochores in vivo. More detail on the instrumentation and theory of FLIM-FRET is available in several other publications (Becker, 2012a; Festy *et al.*, 2007; Ebrecht *et al.*, 2014).

### 2.3.1 Two-photon FLIM Instrumentation

The essential components of a time-domain FLIM system are described in Figure 2.2. The optics between the pulse laser and scanning system should be carefully examined and aligned before each experiment, as they influence the spatial resolution and the uniformity of

the excitation intensity over the scanning area. The two most important optical components to optimize are the telescope, the combination of lenses that expands or reduces the size of the excitation beam, and the periscope assembly, the combination of mirrors that translates the beam. In order to fully utilize the numerical aperture of the objective, the telescope needs to be adjusted such that the excitation beam is well collimated when entering the objective and large enough to overfill the back aperture of the objective. The periscope assembly should be adjusted such that the beam is perpendicular and centered when entering the objective[2].

### 2.3.2 Live Cell Kinetochore FLIM-FRET Imaging

This section provides step-by-step instruction on live cell kinetochore FLIM-FRET imaging. We will present an example using a FRET biosensor for Aurora kinase B activity fused to Hec1, an outer kinetochore protein, in U2OS cells. See Fuller *et al.* (2008) for more information on the Aurora kinase B FRET biosensor.

1. Choice of fluorescent proteins.

   The most important factor to consider when choosing a donor fluorescent protein is the complexity of the donor's fluorescence decay. Some fluorescent proteins, such as ECFP and EYFP, exhibit multiexponential fluorescence decay. Multiexponential fluorescence decay greatly complicates the analysis and interpretation of FLIM data. Therefore, it is essential to verify a mono-exponential fluorescence decay of the donor fluorescent protein through negative controls. A proper negative control is the donor fluorescent protein targeted to the same protein as the FRET probe, so that the local environmental effects on the fluorescence decay can be investigated in advance

[2]Some alignment tools can facilitate the adjustment and alignment of the periscope and telescope assembly. Fluorescing alignment disks (such as VRC2RMS, Thorlabs), which can be mounted on the nose piece of microscope, is particularly useful as it can be used to visualize the size and position of the beam entering the objective. We also use a fluorescing alignment disk in combination with a long lens tube (such as SM1E60, Thorlabs) to ensure the perpendicularity and collimation of the excitation beam. To achieve perpendicularity, we adjust the periscope assembly such that the beam is centered on the alignment disk when the disk is mounted on the nose piece and when it is mounted on a lens tube that is installed on the nose piece (i.e. the alignment disk is positioned away from the nose piece by the length of the lens tube). To achieve collimation, we adjust the telescope assembly such that the size of the beam is the same at the nose piece and away from the nose piece.

of the FRET measurements. As in other fluorescence microscopies, brightness and photostability are also important, since the number of photons determines the precision of FLIM-FRET measurement. The acceptor fluorescent protein should be chosen such that the Förster radius is large enough that the FRETing and non-FRETing states can be easily distinguished. Another important factor to consider is the maturation time of the acceptor fluorescent protein. Slow maturation leads to a large fraction of acceptors being unfolded or immature, and therefore results in the reduction of the number of donor molecules that can engage in FRET. The photostability of the acceptor is also essential for prolonged imaging, but the brightness of the acceptor is not crucial, since emission from the acceptor is not measured in FLIM-FRET.

We chose mTurquiose2 (Cyan) and YPet (Yellow) to be the donor and acceptor fluorescent proteins in the Aurora kinase B FRET reporter. mTurquiose2 is suited for FLIM-FRET, because of its monoexponential fluorescence decay, long fluorescence lifetime ($\approx$4 ns), and excellent brightness with the quantum yield of 93% (Goedhart *et al.*, 2012).

2. Make a plasmid that carries the DNA sequence of the desired kinetochore protein tethered to the FRET probe using standard cloning techniques.

3. Transfect cells.

   Since the brightness of the donor fluorescent protein at kinetochores has influence on the precision of FLIM-FRET measurement, high expression of the labeled protein is preferred as long as overexpression doesn't affect its behavior. Transient transfection results in some cells having multiple plasmids, which therefore express the construct at very high level. If transient transfection is difficult or undesirable, stable cells lines can be made using viruses or genome-editing techniques such as CRISPR.

4. Prepare a sample for imaging by culturing cells on a sample coverglass. Incubate in complete media for about two days, at 37 °C, 5% $CO_2$.

5. Switch the complete growth media to the imaging media 30 minutes before imaging.

6. Prepare the FLIM setup

   Turn on and warm up the Ti:sapphire laser, pre-warm the microscope sample chamber and objective lens heater to 37 °C. Check the alignment of the optical system, and choose a proper emission filter. Calibrate the device that modulates the excitation intensity[3].

   The Ti:sapphire laser needs to be set to the optimal two-photon excitation of the donor fluorescent protein, which is 865 nm for mTurquoise2. The optical alignment should always be checked before imaging, since a defective PSF worsens image quality and two-photon excitation efficiency.

   The emission filter must be carefully chosen such to minimize signal from the acceptor, reduce the detected cellular background autofluorescence, and maximize the emission collected from the donor. For the mTurquiose2/YPet pair, we use ET470/40m filter (Chroma).

   The alignment and other imaging setting should be verified by imaging a standard sample before the experiment. We normally use Alexa dye on a coverslip to check the uniformity of the excitation, and 200 nm fluorescent microsphere (T14792, Life Technologies) to check the quality of the point spread function. When the system is aligned properly, the full width at half maximum of the point spread function should be ≈300 nm.

7. Mount the sample on the temperature-controlled microscope chamber

   Layer the coverslip with the imaging media that is equilibrated at 37 °C, 5% $CO_2$, and then cover with mineral oil to prevent evaporation. Clean the bottom of the coverslip with a Kimwipe and ethanol before mounting the chamber to the microscope stage.

8. Acquire FLIM images with the appropriate imaging settings.

[3]We place a linear polarizer, a motorized half-wavelength plate and another linear polarizer in series in the laser path to modulate the excitation intensity; the transmission of the laser changes as the angle of the half-wavelength plate changes. Before every experiment, we create a mapping between the angle of the half-wavelength plate and the excitation laser intensity, by measuring the laser power at the objective lens.

The following is the general guideline of choosing imaging settings: determine the scanning region such that the region of interest just fits into it; using a larger scanning area will lower the frame rate. The pixel size should be chosen so as to conform the Nyquist criterion[4]. That is, if the spatial resolution is ≈300 nm, the pixel size needs to be less than 150 nm. The integration time should be short enough that moving kinetochores are not blurred, and long enough that more than a few hundreds photons per kinetochore are accumulated and kinetochores are clearly distinguished against the background noise.

For kinetochore imaging of U2OS cells, high quality images can be obtained with an NA 1.25, 40x water-immersion objective, a 14 $\mu$m$\times$14 $\mu$m scanning region, 128 $\times$ 128 pixels, and a 3-5 seconds integration time. Smaller regions can be scanned at higher speeds. The repeat time —- the time between two consecutive images —- should be determined according to the aim of the study: studying kinetochore oscillations in metaphase may require a repeat time of as short as 10 seconds, while for studying long-term changes, a repeat time of a few minutes may be preferable, considering the photo-damages due to repeated excitations. The excitation beam power is typically set to 1-2 mW. Higher power may induce photodamage, with symptoms including metaphase arrest, prolonged metaphase, shrinkage of the spindle, and an increase in autofluorescence.

In order to prevent the emergence of artifacts related to photodamage and photobleaching, one should carefully choose appropriate imaging settings by performing negative control experiments. The best negative control sample is cells expressing the protein of interest labeled with only the donor. To test an imaging setting, take images of the negative control sample with the imaging setting, and check whether the observed fluorescence lifetime and/or brightness of the donors change over time. Photodamage is known to result in the increase in autofluorescence (Galli *et al.*, 2014),

[4]The Nyquist criterion requires a sampling interval equal to twice the highest spatial frequency of the specimen to accurately preserve the spatial resolution in the resulting image.

which contaminates the fluorescence signal from donor and may change the observed fluorescence lifetime. Photobleaching may also change the observed fluorescence lifetime as it increases the relative contribution of the autofluorescence. Photodamage and photobleaching are highly nonlinear with excitation intensity, following a power law with the exponent greater than 2, while the two-photon excitation is proportional to intensity squared (Hopt and Neher, 2001; Patterson and Piston, 2000). Therefore, photodamage and bleaching can be significantly suppressed by lowering the excitation intensity, without sacrificing the fluorescence signal from the donor as much. For this reason, as a way to enhance the signal-to-noise ratio, using longer integration time is preferred over using higher excitation intensity.

9. Record the instrument response function (IRF) of the FLIM system by measuring second harmonic generation (SHG).

   The IRF plays a very important role in FLIM analysis, and therefore an accurate measurement of the IRF is crucial. The IRF can easily be recorded by measuring second harmonic generation (SHG) signal from a urea crystal. SHG is a nonlinear optical process in which a material that lacks inversion symmetry converts incident photons into photons with half the wavelength of the incident photons. SHG is an ultrafast scattering process so the FLIM curve of SHG provides an accurate measure of the IRF of the FLIM system.

   To make a urea crystal sample for IRF measurements, dissolve urea in water and drop $\approx$10 $\mu$l of the urea solution on the coverslip. As the water evaporates, it leaves crystalized urea on the coverslip. Put the coverslip on a microscope slide and seal it. This urea crystal IRF standard can be used repeatedly.

   To record the IRF, set up the emission bandpass filter such that it transmits the photon of the wavelength half of the excitation wavelength. For example, 425/30 can be used for 865 nm excitation. Since the IRF is specific to the imaging settings, every imaging setting other than the emission filter must remain the same. Place the urea crystal on the objective, and park the excitation laser where the crystal generates significant SHG.

Make sure that the number of time bins is set to the maximum value. Record SHG for 30-60 seconds, allowing a smooth IRF curve to be generated. When acquiring the IRF using an SHG sample, remove or cover the condenser lens because it may reflect the SHG and cause additional peak in the measured IRF curve.

### 2.3.3 Analysis of Kinetochore FLIM-FRET Imaging

#### FLIM-FRET Models

If there is no donor engaged in FRET, then the number of photons $n(t)$ decays monoexponentially with a long lifetime $\tau_D$:

$$n(t) \propto A \exp(-t/\tau_D) + (1 - A) \tag{2.1}$$

where the parameter $A$, which ranges from 0 to 1, is the fraction of detect photons emitted by the donor. In most applications, the dark noise is low, and thus $A$ is usually very close to 1.

On the other hand, if there is a mixture of donors, with some donors engaged in FRET (all with the same FRET efficiency) and the others not engaging in FRET, then the number of detected photons is a biexponential:

$$n(t) \propto A \left\{ f \exp(-t/\tau_D) + (1 - f) \exp(-t/\tau_{FRET}) \right\} + (1 - A) \tag{2.2}$$

where $f$ is the fraction of donors that are not engaged in FRET, and $\tau_D$ and $\tau_{FRET}$ are the lifetimes of donor not in FRET state and in FRET state, respectively. $\tau_D$ and $\tau_{FRET}$ can be translated into the FRET efficiency by:

$$E_{FRET} = 1 - \frac{\tau_{FRET}}{\tau_D} = \frac{1}{1 + \left(\frac{r}{R_0}\right)^6} \tag{2.3}$$

where $r$ is the separation between donor and acceptor fluorophores and $R_0$ is the Föster radius (Lakowicz, 2011a).

Figure 2.4 shows experimentally measured FLIM curves from two samples, where no

donors are engaging in FRET and where some donors are in a FRET state. It is apparent that the FLIM curve decays faster when there is FRET, as predicted. Upon closer inspection, it is evident that the data significantly departs from the simple exponential model: the real data appears to be shifted and broadened relative to the model. This discrepancy comes from the limited temporal resolution of the FLIM system and from the finite travel time of photons and information in the system. Fortunately, these discrepancies are determined by the instrument configuration, and can be measured and incorporated into the model. These effects are captured by the instrument response function (IRF), which is what the FLIM system would record from a sample with an infinitely short lifetime. As mentioned above, the IRF can be experimentally measured and usually appears to be a sharp, skewed peak, shifted from $t = 0$ by the same extent as the exponential decay in FLIM curve (Figure 2.5).

As illustrated in Figure 2.5, a complete FLIM model can be constructed by convolving the exponential decay model (Eq. 2.1 or 2.2) with the measured IRF:

$$y = C_{norm} \times IRF(t - t_s) \otimes n(t) \tag{2.4}$$

where $C_{norm}$ is a normalization constant, $IRF$ is the measured instrument response function, $t_s$ is the shift of the measured IRF relative to the real IRF, and $n(t)$ is the exponential decay model given by Eq. 2.1 and 2.2. The shift $t_s$ is necessary for precise fitting because the location of the measured IRF may be different by small extent, usually within 100ps, from the real IRF. The constant $C_{norm}$ may be determined by normalizing the area under the curve to the total photon counts, but for some inference methods such as Bayesian analysis, which is introduced in the later section, $C_{norm}$ is not even necessary. Thus, Eq. 2.1 or 2.2 describes the behavior of the donor fluorophore, while the IRF describes the behavior of the FLIM instrument.

The more realistic model of Eq. 2.4 is sufficient to describe experimental data, and can thus be fit to the measured FLIM curves to determine the five FLIM parameters: $t_s$, $A$, $\tau_D$, $f$, and $\tau_{FRET}$.

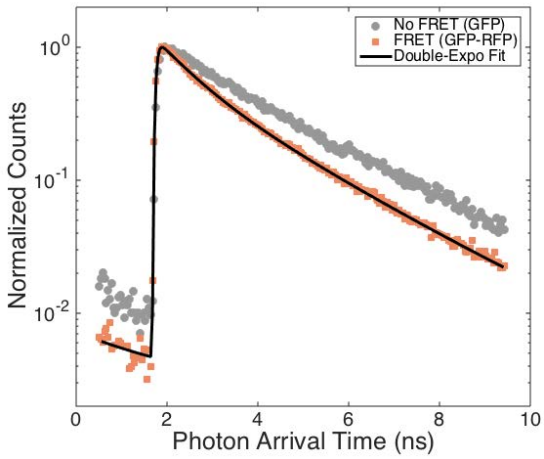


**Figure 2.4:** *Normalized FLIM curve on log-scale of donor when there is no donor engages in FRET (gray) and when some fraction of donors are engages in FRET (orange)*

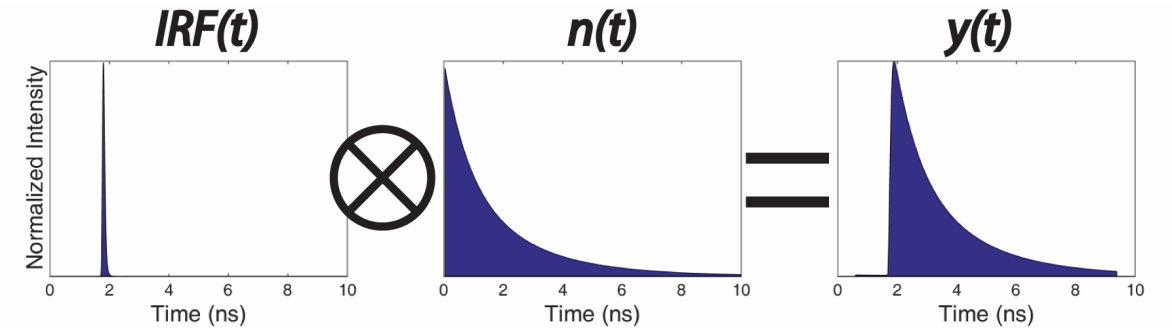


**Figure 2.5:** *The illustration of building a complete FLIM model by convolving IRF and exponential decay model*

### Identification and Tracking of Kinetochores

We developed a MATLAB graphical user interface (GUI) that semi-automatically analyzes kinetochore FLIM-FRET data, which allows high-throughput kinetochore analysis.

First, load FLIM images (Figure 2.6). Then identify and track kinetochores using standard particle tracking techniques. We modified the particle tracking MATLAB codes developed and used in Pelletier *et al.* (2009), and incorporated it into the GUI. As shown in Figure 2.6b, each kinetochore trajectory is automatically labelled with a number, and the GUI enables us to manually modify mislabelled kinetochore features, or remove features that are incorrectly identified as kinetochores. By fitting 2D Gaussian to each kinetochore, the location of the kinetochore can be determined with sub-pixel precision, and can be used for distance and velocity measurements.

### FLIM-FRET Measurement of Kinetochore with Bayesian Analysis

Assuming that the fluorescence lifetimes of FRET and non-FRET states are constant throughout the movie, we can precisely determine the lifetimes by grouping all the FLIM curves from the kinetochores in every image to obtain a FLIM curve with a large number of photons (Figure 2.6c), and make inference using the biexponential FLIM model (Figure 2.6d). In the analysis of FLIM curves in each frame or each kinetochore with a fewer number of photons, we can fix the lifetimes and IRF shift to the values determined from the sum of many FLIM curves, and perform the biexponential FLIM-FRET Bayesian analysis with a reduced number of free parameters to accurately measure the fraction of the donors engaged in FRET at each timepoint or at each kinetochore. (Figure 2.6e,f)

Getting accurate and precise estimation of parameters in a biexponential FLIM-FRET model is not a simple task, especially when the number of photons composing the FLIM curve is small. When the number of photons is of the order of $10^5$ or higher, commonly used nonlinear least-square fitting of the Eq. 2.4 may provide the estimates of the FLIM parameters with reasonable accuracy and small bias. However, when the number of photons is very limted, which is the case for the study of dynamic kinetochores, a Bayesian approach

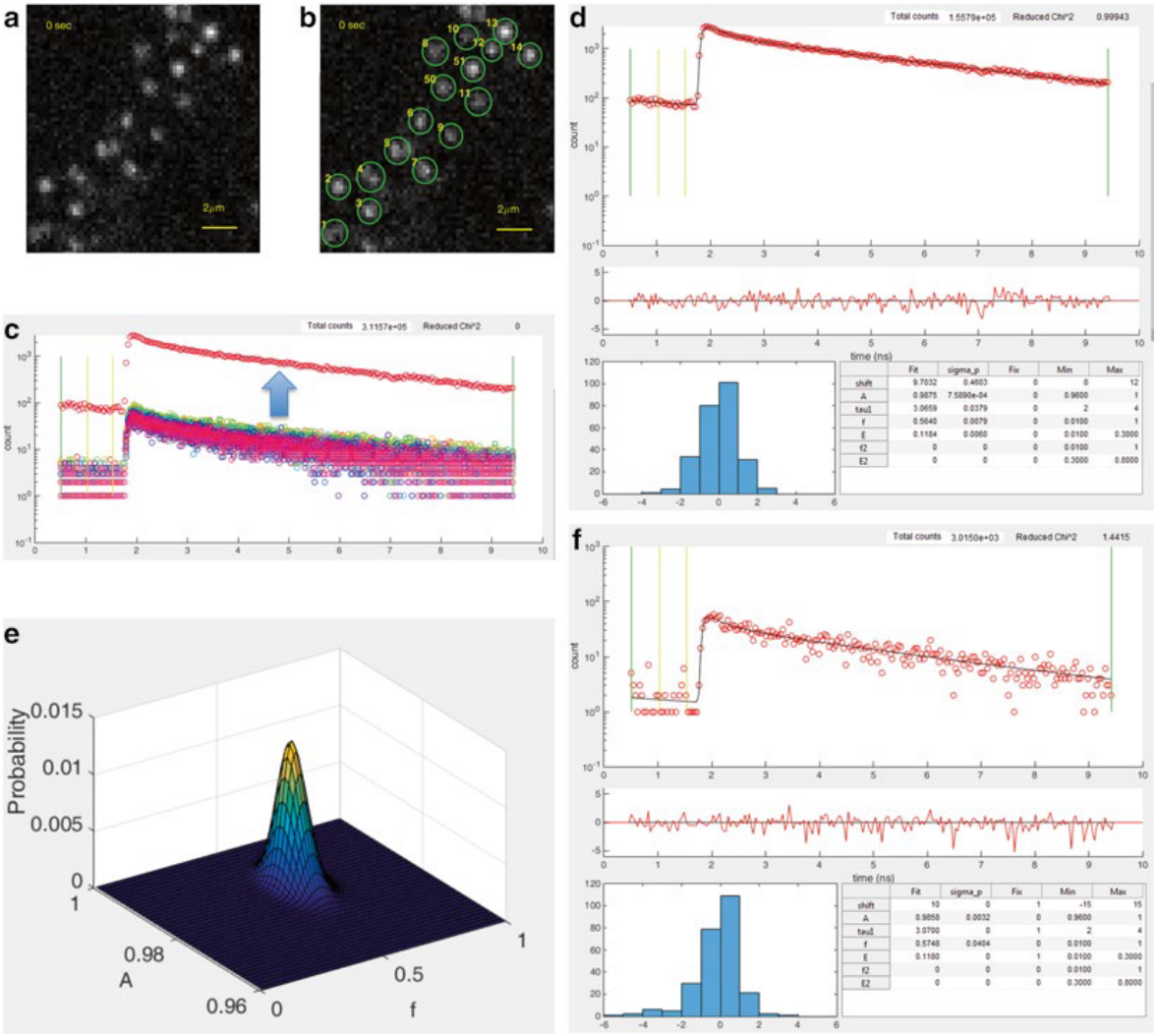


**Figure 2.6:** *Kinetochore FLIM-FRET measurement procedures. (a) Loading FLIM images saved in a special data format. (b) Identification of kinetochores. (c) Summing the FLIM curves obtained from every kinetochore, and (d) determination of the fluorescence lifetimes. (e, f) Bayesian FLIM analysis on the FLIM curve from one frame*

with a complete probabilistic model must be employeed, in order to minimize the bias resulting from the simplified assumption inherent to least-square fitting.

Let $\theta$ be the set of parameters that governs the FLIM model, and $y = [y_i]$ be the observed FLIM data, where $y_i$ is the number of photons detected in $i$-th time bin of the FLIM curve. The aim of Bayesian inference is to obtain the posterior probability distribution of the parameters of interest, $p(\theta|y)$, through the Bayes rule:

$$p(\theta|y) \propto p(y|\theta)p(\theta) \tag{2.5}$$

The common name of the first term in the product $p(y|\theta)$ is the "likelihood function," which is the probability of the observed data $y$ given the parameter values $\theta$. The likelihood function is based on the data generation process. Let $\Delta t$ be the width of the time bin with which the FLIM data is acquired. Then the likelihood function can be written as

$$p(y|\theta) \propto \prod_{i=1}^{N} P\left(t_{ar} \in [(i-1)\Delta t, i\Delta t] \,|\theta\right)^{y_i} \tag{2.6}$$

where $t_{ar}$ is the photon arrival time, and $N$ is the number of time bins. Assuming that the size of the time bin is very small compared to the time scale of fluorescence decay, the probability that the arrival time tar falls in the $i$-th time bin is approximated by a Riemann sum:

$$P\left(t_{ar} \in [(i-1)\Delta t, i\Delta t] \,|\theta\right) \approx \sum_{k=(i-1)K+1}^{iK} h_\theta(k\tilde{\Delta}t)\tilde{\Delta}t \tag{2.7}$$

where $\tilde{\Delta}t$ is the smallest time bins with which IRF is measured, and the ratio $K = \frac{\Delta t}{\tilde{\Delta}t}$ is a positive integer. $h_\theta(k\tilde{\Delta}t)$ in the Eq. 2.7 can be written as:

$$\begin{aligned} h_\theta(k\tilde{\Delta}t) &= \left[IRF \otimes (Ag_\theta + (1-A))\right](k\tilde{\Delta}t) \\ &\approx \sum_l mIRF[l - b_{shift}]\left(Ag_\theta\left((k-l)\tilde{\Delta}t\right) + (1-A)\right) \end{aligned} \tag{2.8}$$

where $mIRF$ is the IRF measured in the finest time bins with size $\tilde{\Delta}t$, and $b_{shift}$ is an integer parameter that determines the approximate shift of measured IRF from the theoretical IRF. The function $g_\theta$ depends on the number of exponentials in the FLIM model. For example, when there are two species of donors, one of which are engaged in FRET with the same

efficiency and the other not, $g_\theta$ is expressed as:

$$g_\theta(t_d) = f \exp(-t_d/\tau_D) + (1-f)\exp(-t_d/\tau_{FRET}) \tag{2.9}$$

We ignored the 'pile-up' effect that results from photons that are emitted from the fluorophores excited in the previous pulses and appear in the current laser period, as typically this effect is very small for commonly used fluorophores with lifetime shorter than 4ns. Eq. 2.8 can be efficiently evaluated by using a fast convolution algorithm combined with fast Fourier transformation, rather than directly carrying out the summation.

The Bayes rule (Eq. 2.5) results in the posterior distribution:

$$p(\theta|y) \propto p(\theta) \prod_{i=1}^{N} P\left(t_{ar} \in [(i-1)\Delta t, i\Delta t] \,|\theta\right)^{y_i} \tag{2.10}$$

The prior distribution $p(\theta)$ is often chosen to be flat between reasonable upper and lower limits of the parameters[5], i.e. $p(\theta) = 1$.

Eq. 2.10 needs to be numerically evaluated, which can be done using a number of different methods. The grid search method is conceptually simple to implement. In this method, a grid is formed by dividing the range of values for each of parameter in $\theta = \{b_{shift}, A, f, \tau_D, \tau_{FRET}\}$ into a number of discrete levels, and the posterior distribution is computed at each grid point. The computation time grows exponentially with the number of free parameters, and therefore the use of this method is restricted to low-dimensional searches. For example, if the values of $b_{shift}$, $\tau_D$, and $\tau_{FRET}$ are known, and a search is performed over the other two parameters, this method works well with a reasonably fine grid and a computation time of few seconds. On the other hand, if there are many free parameters, Markov Chain Monte Carlo (MCMC) is a faster method. The most popular variants of MCMC are Gibbs sampling and Metropolis-Hastings algorithm (Casella and George, 1992; Geman and Geman, 1984; Gelman *et al.*, 2013).

Once the posterior distribution is calculated, a variety of point and interval estimations of

[5]Any prior knowledge can be incorporated into the posterior distribution through the prior distribution. For example, some studies impose an exponential prior on the lifetime, i.e. $p(\theta) = \alpha \exp(-\alpha\tau)$ (Rowley *et al.*, 2011b)

the parameters can readily be made. If the marginalized posterior distribution is symmetric, its mean is a natural point estimate for parameters. If the marginalized posterior distribution is truncated or asymmetric, the posterior mode may be better a point estimate. The Bayesian probability interval, or credible interval, can be also found from the marginal posterior distribution and be used as an interval estimate of parameter.

One essential advantage of using Bayesian analysis is its explicit use of probability for quantifying uncertainty in inferences. This makes the propagation of uncertainty perspicuous, especially when combining estimates from multiple datasets. Another important advantage of Bayesian FLIM analysis is its superior accuracy and precision compared to other fitting methods. It has been shown that Bayesian analysis can be used to determine fluorescence lifetimes of a monoexponential fluorescence decay with no bias with as little as 50 photons, while LS and MLE cause significant bias' at such low photon counts (Rowley *et al.*, 2011b). We also confirmed that when applied to double-exponential fluorescence decay data Bayesian FLIM analysis is capable of estimating the fraction of one exponential component relative to the other with no bias with only 200 photons. Using standard labeling levels and illumination intensities, one photon can be collected from a single kinetochore every microsecond. Thus, with Bayesian FLIM analysis it should be possible to measure the fraction of fluorophores engaged in FRET at a single kinetochore every 200 microsecond, enabling the study of sub-millisecond dynamics of protein behaviors at kinetochores.

## 2.4 Conclusion

FRET has become one of the most popular ways to study the interactions of proteins, and the application of FRET will continue to increase driven by the advances in fluorophores, imaging techniques, and FRET-based biosensors. FLIM provides an accurate and quantitative measurement of FRET with high spatial and temporal resolution. In this chapter, I demonstrated how the live-cell FLIM-FRET experiment is designed, performed, and analyzed for the study of kinetochores. At the end, I introduced the Bayesian approach to analyze the FLIM data. This approach has significant advantages over using simple curve

fitting algorithms, especially in the regime where the number of photon is very low or the FRET population is very small relative to the non-FRET population. These advantages will be demonstrated and discussed in the following chapter.

# Chapter 3

# Developing and Testing a Bayesian Analysis of Fluorescence Lifetime Measurements[1]


## Abstract

FRET measurements can provide dynamic spatial information on length scales smaller than the diffraction limit of light. Several methods exist to measure FRET between fluorophores, including Fluorescence Lifetime Imaging Microscopy (FLIM), which relies on the reduction of fluorescence lifetime when a fluorophore is undergoing FRET. FLIM measurements take the form of histograms of photon arrival times, containing contributions from a mixed population of fluorophores both undergoing and not undergoing FRET, with the measured distribution being a mixture of exponentials of different lifetimes. Here, we present an analysis method based on Bayesian inference that rigorously takes into account several experimental complications. We test the precision and accuracy of our analysis on controlled experimental data and verify that we can faithfully extract model parameters, both in the


[1]Reprinted from Kaye, Foster, Yoo and Needleman (2017). B. Kaye, P. Foster, and T.Y. Yoo contributed equally to the work.

low-photon and low-fraction regimes.

## 3.1 Introduction

Förster resonance energy transfer, or FRET, is a fluorescence technique commonly used to access spatial information on length scales smaller than the diffraction limit of light Roy *et al.* (2008). In standard fluorescence, illuminating light is used to excite a fluorophore into a higher energy state, and the fluorophore subsequently relaxes into its ground state either by emitting a photon or through a non-radiative decay pathway. If another fluorophore is near, typically within $\approx 10$ nm, the two fluorophores can interact through dipole-dipole interactions termed FRET. FRET confers an additional decay path where the excited florophore, termed the donor, can transfer its energy to the nearby, unexcited fluorophore, termed the acceptor, which can then release the energy as a photon or through non-radiative decay. As the emission spectra of commonly used donor and acceptor pairs are spectrally distinct, one common method of measuring the the average FRET efficiency is to compare the relative intensities collected from the two channels. However, this method has drawbacks including spectral bleed-through and a sensitivity to changes in fluorophore concentration and excitation light intensity Wallrabe and Periasamy (2005).

As an alternative to using fluorescence intensity to quantify FRET, fluorescence lifetime imaging microscopy, or FLIM, can be used (Stachowiak *et al.*, 2012; Peter *et al.*, 2005; Yoo and Needleman, 2016; Hinde *et al.*, 2013). FLIM is a general technique that allows changes in a flurophore's local environment to be probed. While use of FLIM is not limited to measuring changes in FRET, it can be used in this context without some of the drawbacks of an intensity based measurement. In time-domain FLIM, a narrow pulse of light is used to excite fluorophores into an excited state. Fluorophores that decay from their excited states can do so by releasing a photon. A subset of the released photons are detected, and for each detected photon, the arrival time is measured relative to the excitation pulse. The amount of time fluorophores spend in their excited state depends on the number of decay paths available. Donor fluorophores are chosen such that when they decay from their excited

states, they do so at a constant rate, leading to photon emission time distributions that are exponential with a single characteristic decay time. This characteristic decay time is known as the fluorescence lifetime and is typically on the order of nanosconds. When donor fluorophores are undergoing FRET, they will spend, on average, a shorter amount of time in their excited states, leading to a reduced lifetime and quantum efficiency (Lakowicz, 2011b). In a sample where only a fraction of donor fluorophores are undergoing FRET, the photon emission time distribution will be the sum of two exponentials with different lifetimes. By comparing the amplitudes of these two exponentials, the relative fraction of donors undergoing FRET can be measured. In practice, additional complications are present, including photons collected from spurious background and time delays introduced by the collection system itself. These effects must be accounted for to infer the relative amplitudes and lifetimes of the emitted photon distributions from the measured photon arrival time histograms. Several approaches have been used in order to estimate these parameters, including least-squares fitting (Chang *et al.*, 2007), rapid lifetime determination (Sharman *et al.*, 1999), phasor methods (Stringari *et al.*, 2011; Colyer and Siegmund, 2012; Chen *et al.*, 2015), and Bayesian approaches (Rowley *et al.*, 2011a), each with their own advantages and disadvantages.

Here we utilize and extend the Bayesian approach previously described (Rowley *et al.*, 2011a) to take into account biexponential decays and additional experimental factors and we test the performance of our method using experimental data.

## 3.2 Materials and Methods

### 3.2.1 Bayesian Framework

Our framework is based on a previously described Bayesian analysis approach for measuring lifetimes from FLIM data (Rowley *et al.*, 2011a). For an introductory overview of Bayesian analysis, we direct the reader to (Sivia and Skilling, 2008). Bayes' Law states that given a set

of data, $t$, and a set of model parameters $\theta$, then,

$$p(\theta|t) \propto p(t|\theta) \times p(\theta) \tag{3.1}$$

where $p(\theta|t)$, the probability of the model parameters given the measured data, is referred to as the posterior distribution, $p(t|\theta)$ is referred to as the likelihood function, and $p(\theta)$ is referred to as the prior distribution. The aim of Bayesian inference approaches is to find the posterior distribution for the given model and data, and hence what the probability is for each possible set of model parameters $\theta$.

In time-domain FLIM measurements, a narrow laser pulse is used to excite fluorophores in the sample, and the arrival times of photons emitted from the fluorophores are recorded. Fluorophores undergoing FRET will have a shorter florescence lifetime compared with fluorophores not undergoing FRET. When only a fraction of fluorophores in the sample are undergoing FRET, the resulting distribution of photon emission will be a sum of exponentials, where each exponential has a different lifetime, and each exponential is weighted by the number of photons collected from the respective source. In addition, there exists a constant background of photons due to noise in the detector and stray light, taken to be from a uniform distribution. In the following, we consider photons from each of these sources separately and construct the likelihood function as follows,

$$p(t|\theta) = f_S \times p_S(t|f_S, \tau_S) + f_L \times p_L(t|f_L, \tau_L) + f_B \times p_B(t|f_B) \tag{3.2}$$

where t is the arrival time of a photon relative to the excitation pulse, $\tau_S$ and $\tau_L$ are respectively the short and long fluorescence lifetimes, $f_S$ and $f_L$ are the fractions of photons from the short and long lifetime distributions respectively, $f_B$ is the fraction of photons from the uniform background given by $f_B = (1 - f_S - f_L)$. Here $p_i(t|f_i)$ is the probability of the photon arriving at time t given that the photon originates from fraction $f_i$.

Equation 3.2 represents the likelihood model when time is taken to be continuous. However, in practice, photon arrival times collected with TCSPC are discretized into bins, and this discretization must be taken into account. If the bins are numbered sequentially

and of width $\Delta t$, such that $b_i$ represents the bin containing photons with arrival time, $(i-1)\Delta t \leq t \leq i\Delta t$, then the likelihood function becomes,

$$p(t|\theta) = \prod_{i=1}^{N} \Big[ f_S \times p_S(t \in b_i | f_S, \tau_S) + f_L \times p_L(t \in b_i | f_L, \tau_L) + f_B \times p_B(t \in b_i | f_B) \Big]^{P_i} \tag{3.3}$$

Thus, Eqn. 3.3 serves as the discrete form of the likelihood function, Eqn. 3.2.

### 3.2.2 Instrument Response Function

One complexity in experimental TCSPC measurements is that a delay is introduced to photon arrival times, termed the Instrument Response Function (IRF). In order to account for this effect, the IRF was experimentally measured (see FLIM Measurements). The measured IRF is then convolved with the idealized probability density functions for the exponential distributions in order to construct the likelihood function. Taking this effect into account leads to,

$$p_j(t \in b_i | f_j, \tau_j) = p_{em,j}(t \in b_i | f_j, \tau_j) \otimes IRF(t) \tag{3.4}$$

where $p_{em,j}$ is the idealized exponential distribution, taken to be $\propto e^{-t/\tau_j}$, where $j \in \{S, L\}$ is an index labeling the exponential distribution and $IRF(t)$ is the experimentally measured instrument response function.

### 3.2.3 Posterior Distribution

Using Eqn. 3.4 in Eqn. 3.3 leads to the final form of our likelihood function,

$$p(t|\theta) = \prod_{i=1}^{N} \Big[ f_S \times p_{em,S}(t \in b_i | f_S, \tau_S) \otimes IRF(t) + f_L \times p_{em,L}(t \in b_i | f_L, \tau_L) \otimes IRF(t) + f_B \times p_B(t \in b_i | f_B) \Big]^{P_i} \tag{3.5}$$

For comparison with experiments using control dyes where the lifetimes of the two molecules are well characterized, we choose a prior distribution such that the distribution is uniform for the fractions in the domain $f_j \in [0, 1]$, and $\tau_S$ and $\tau_L$ are set to the measured values for Coumarin 153 and Erythrosin B respectively. With this choice of prior, Eqn. 3.1 becomes,

$$p(\theta|t) \propto p(t|\theta) \tag{3.6}$$

and hence our posterior distribution is proportional to our likelihood function in the constrained parameter space. To build the posterior distribution, parameter space is searched by evaluating the likelihood function on a grid of uniform spacing. Alternatively, parameter space can be searched stochastically using the Markov chain Monte Carlo method, yielding equivalent results (Figure 3.1).

### 3.2.4 Effects of Periodic Excitation

For a single exponential decay, the probability of measuring a photon at time t, given a decay lifetime, $\tau$, is given by,

$$p_{em}(t|\tau) \propto e^{-\frac{t}{\tau}} \tag{3.7}$$

Where $\tau$ is the lifetime of the fluorophore. In practice, many sequential excitation pulses are used, and it's possible that a fluorophore excited by a given pulse doesn't emit a photon until after a future pulse. Taking this effect into account for a single exponential decay leads to (Rowley *et al.*, 2011a),

$$p_{em}(t|\tau, T) \propto \sum_{k=0}^{\infty} e^{-\frac{t+kT}{\tau}} \tag{3.8}$$

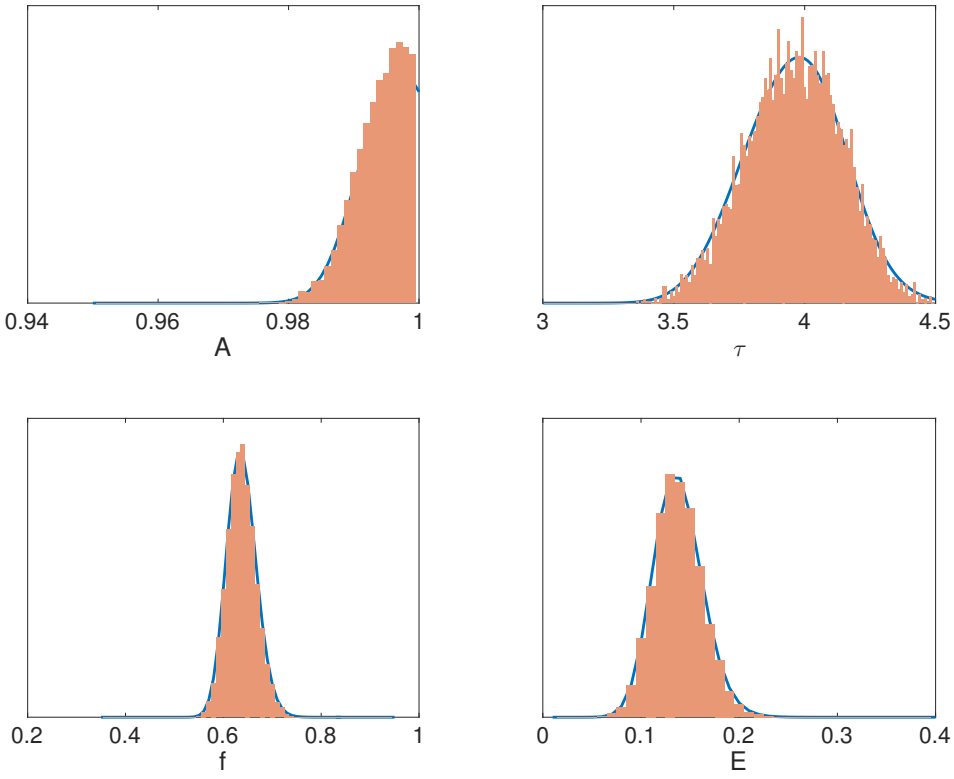


**Figure 3.1:** ***Posterior distributions generated using grid points and stochastic simulation are equivalent.*** *Results from Markov Chain Monte Carlo (red) and grid points (blue) were generated from the same data set.*

where $T$ is the excitation pulse period and $k$ is an index counting previous pulses. The sum is a geometric series, which converges to,

$$p_{em}(t|\tau, T) \propto \frac{1}{1 - e^{\frac{-T}{\tau}}} e^{\frac{-t}{\tau}} \tag{3.9}$$

Thus, accounting for periodic excitations leads to a prefactor $\frac{1}{1-e^{\frac{-T}{\tau}}}$, which for a given $T$ and $\tau$ is constant. As we treat exponentials from populations with short and long lifetimes separately, this factor can safely be absorbed into the normalization constant, leaving the probability distribution unchanged.

### 3.2.5 FLIM Measurements

FLIM measurements were carried out on a Nikon Eclipse Ti microscope using two-photon excitation from a Ti:sapphire pulsed laser (Mai-Tai, Spectra-Physics, 865 nm or 950 nm wavelength, 80 MHz repetition rate, $\approx$ 70 fs pulse width), a commercial scanning system (DCS-120, Becker & Hickl), and hybrid detectors (HPM-100-40, Becker & Hickl). The excitation laser was collimated by a telescope assembly to avoid power loss at the XY galvanometric mirror scanner and to fully utilize the numerical aperture of a water-immersion objective (CFI Apo 40x WI, NA 1.25, Nikon). Fluorescence was imaged with a non-descanned detection scheme with a dichroic mirror (705 LP, Semrock) that was used to allow the excitation laser beam to excite the sample while allowing fluorescent light to pass into the detector path. A short-pass filter was used to further block the excitation laser beam (720 SP, Semrock) followed by an emission filter appropriate for Coumarin and Erythrosin B (550/88nm BP, Semrock, or 552/27nm BP, Semrock). A Becker & Hickl Simple-Tau 150 FLIM system was used for time correlated single photon counting (Becker, 2012b). The instrument response function was acquired using second harmonic generation of a urea crystal (Becker, 2012b).

For the data shown in Figure 3.2, the *TAC range* was set to $7 \times 10^{-8}$ with a *Gain* of 5, corresponding to a 14 ns maximum arrival time. The *TAC offset* was set to 6.27%. The TAC *limit high* and *limit low* were set to 5.88% and 77.25%, respectively, resulting in a 10 ns recording interval. Erythrosin B and Coumarin 153 samples were prepared at 10 mM and

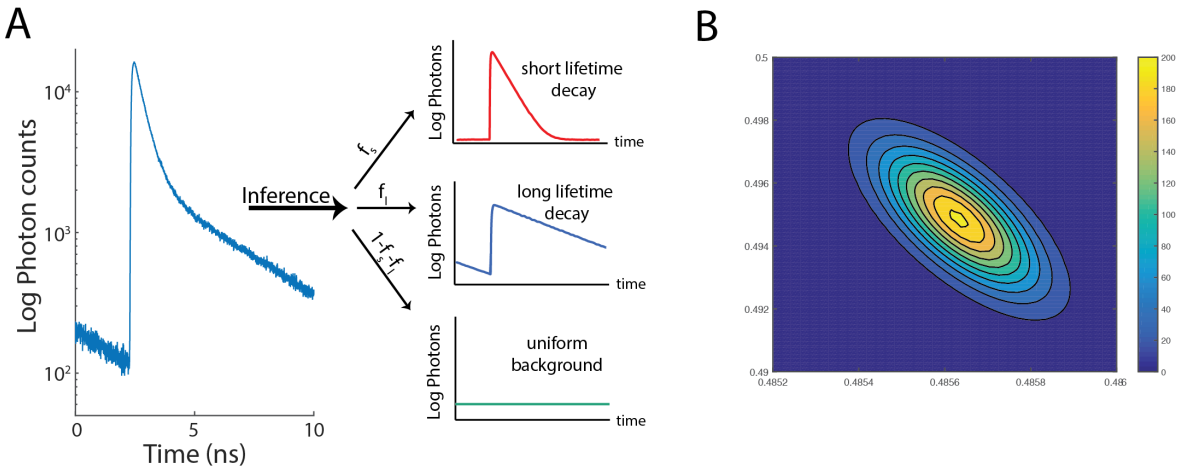


**Figure 3.2:** ***Photon arrival-time histograms are composed of the sum of two exponential distributions.*** *(A) Photon arrival histogram composed of two exponential distributions, with a short-lifetime fraction $f_S$, a long-lifetime fraction $f_L$, and a background fraction $f_B = (1 - f_S - f_L)$. (B) Posterior distribution generated from data in (A).*

15 mM, respectively. Lifetimes were measured and fixed at values of 3.921 ns and 0.453 ns for Coumarin 153 and Erythrosin B respectively.

For the data shown in Figure 3.3, the *TAC range* was set to $5 \times 10^{-8}$ with a *Gain* of 5, corresponding to a 10 ns maximum arrival time. The TAC *limit high* and *limit low* were set to 95.29% and 5.88%, respectively, resulting in a 10 ns recording interval. Illumination intensity was set such that $\approx 2.5 \times 10^5$ photons per second were recorded at the photon detector. Lifetimes were measured and fixed at values of 4.03 ns and 0.48 ns for Coumarin 153 and Erythrosin B respectively.

For the data shown in Figure 3.4, all settings and parameters were the same as for Figure 3.2.

### 3.2.6 *In vivo* FLIM-FRET measurement

U2OS cell line was maintained in Dulbecco's modified Eagle's medium (DMEM, Gibco), supplemented with 10% Fetal Bovine Serum (FBS, Gibco), and 50 IU/mL penicillin and 50 mg/mL streptomycin (Gibco) at 37°C in a humidified atmosphere with 5% CO2. Cells were seeded on a 25-mm diameter, #1.5-thickness, round coverglass coated with poly-D-lysine

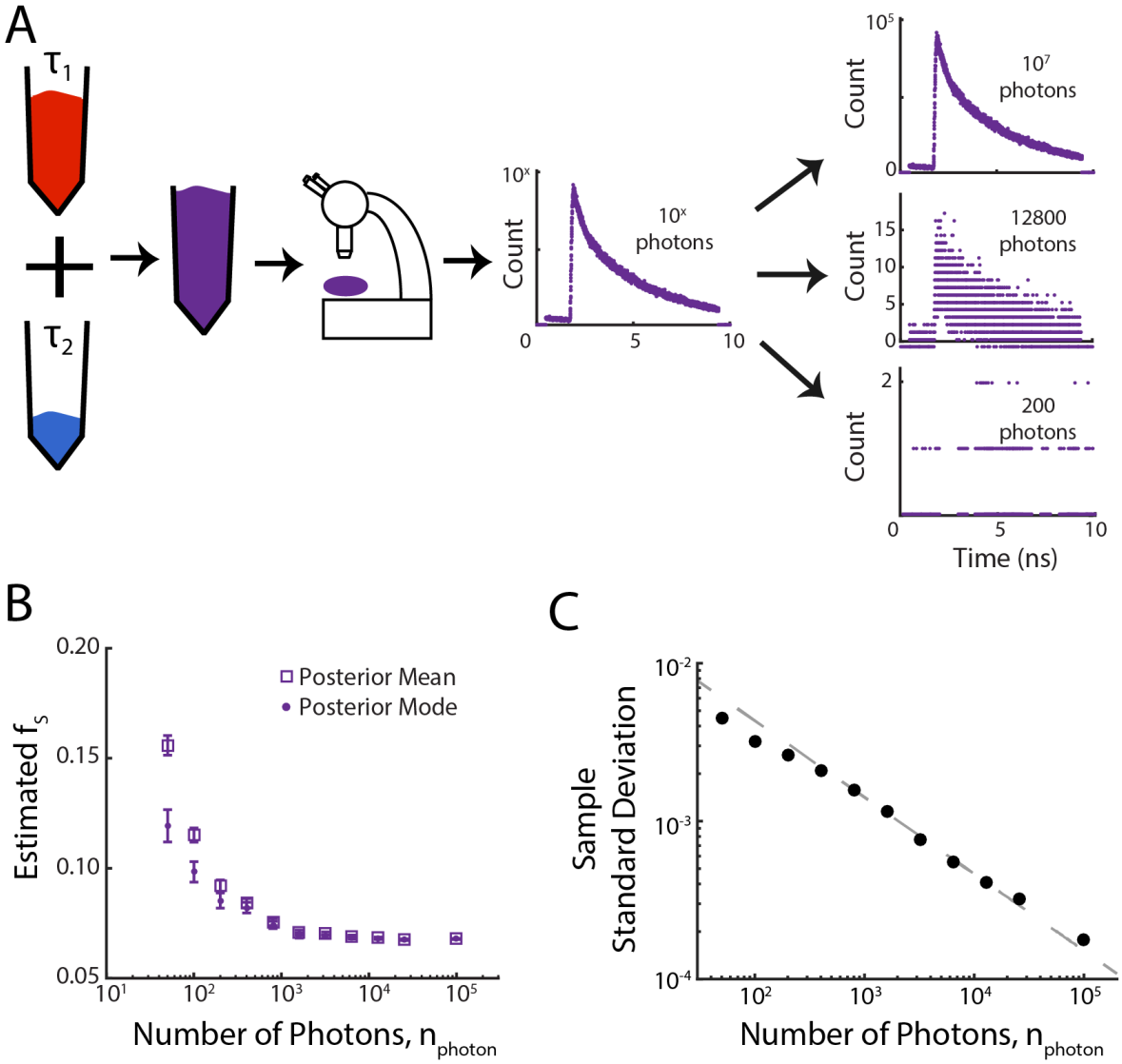


**Figure 3.3:** ***Low-Photon Regime*** *(A) Control dyes having known long (Coumarin 153) and short (Erythrosin B) lifetimes were mixed at a fixed ratio. From the measured master curve of photon arrival times, a variable number of photons are randomly sampled, generating histograms with a variable number of photons. (B) Bias in the estimated short-life photon fraction, $f_S$, decreases with increasing photon number. Data points represent the average of the posterior mean (squares) or mode (circles) for 300 independent samplings for each photon count. Error bars are s.e.m. (C) Black circles: measured sample standard deviations from data in Figure 3.3B averaged across the 300 independent samplings. The sample standard deviation decreases approximately as $\sqrt{n_{photon}}$. Power law fit to $a \times x^b$ for all but the four lowest values of $n_{photon}$ shown in gray, with $a = 0.04 \pm 0.01$ and $b = -0.48 \pm 0.04$ (95% confidence interval)*

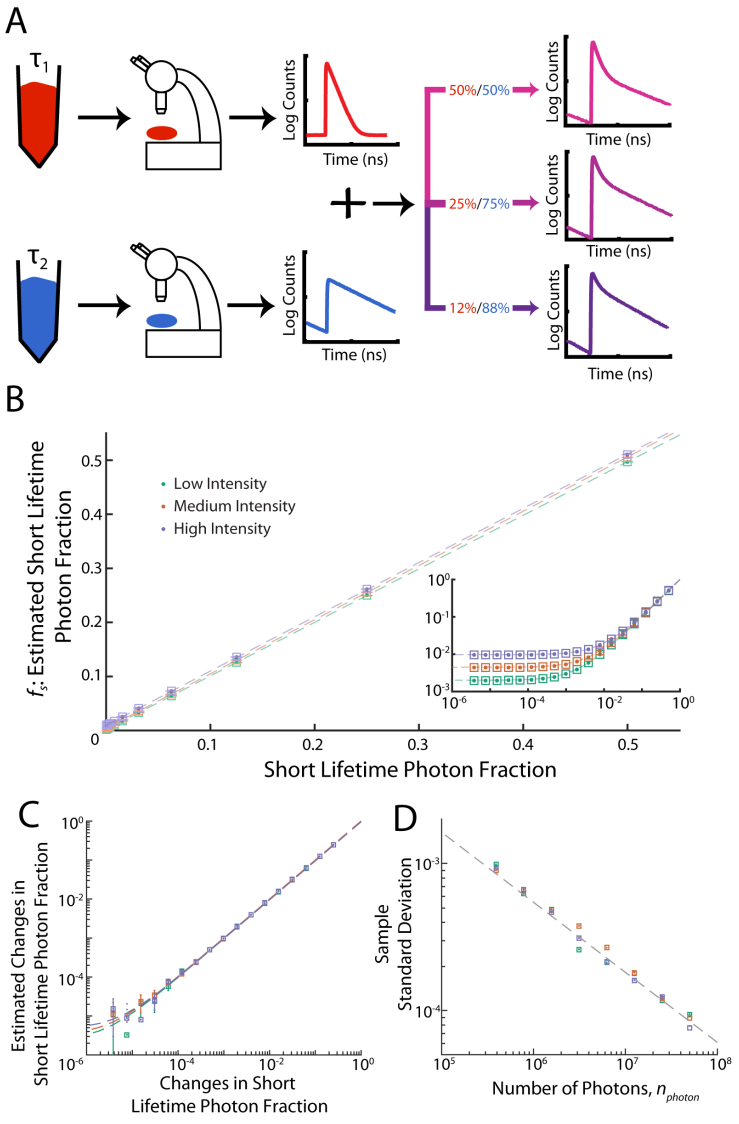


**Figure 3.4:** ***Low-fraction regime*** *(A) Samples of dyes with short-lifetime (Erythrosin B) and long-lifetime (Coumarin 153) were prepared, and fluorescence lifetime measurements were collected for each dye separately, leading to separate master photon histograms. Test histograms were constructed by randomly sampling a fixed number of photons, with varying fractions being drawn from the master lists of short-lifetime and long-lifetime photons. These histograms were then analyzed in order to estimate the fraction of short-lifetime photons,* $f_S$*. (cont'd)*

*(B) The estimated short-lifetime fraction, $f_S$, varies linearly with the constructed short-lifetime fraction for three different total photon numbers, with a small offset. Squares: estimate from posterior mode. Dots: estimate from posterior mean. Dashed lines: linear fits with slopes* $0.9933 \pm 0.0026$, $1.0085 \pm 0.0024$, *and* $1.0106 \pm 0.0031$, *and offsets of* $0.002000 \pm 0.0484 \times 10^{-4}$, $0.004400 \pm 0.0814 \times 10^{-4}$, *and* $0.009500 \pm 0.1992 \times 10^{-4}$ *for low, medium, and high intensities respectively (95% confidence interval). Intensities correspond to data collected at* $\approx 1.5 \times 10^5$, $1.2 \times 10^6$, *and* $4.8 \times 10^6$ *counts per second, for low, medium, and high intensity respectively. Inset: Data from main figure shown on a log-log scale. (C) Changes in the estimated short-lifetime fraction track the known changes in the short-lifetime fraction. Squares: estimate from posterior mode. Dots: estimate from posterior mean. Dashed lines: Linear fits with slopes of* $0.9573 \pm 0.1895$, $1.0013 \pm 0.1445$, *and* $0.9580 \pm 0.1717$, *and offsets of* $(0.2332 \pm 0.3712) \times 10^{-5}$, $(0.3215 \pm 0.3088) \times 10^{-5}$, *and* $(0.4617 \pm 0.4286) \times 10^{-5}$ *for low, medium, and high intensities respectively (95% confidence interval). (D) Sample standard deviations decrease with increasing photon number as* $\approx \sqrt{n_{photon}}$. *Squares: Posterior standard deviation. Dashed line: power law fit to all intensities with exponent* $-0.4764 \pm 0.0471$ *(95% confidence interval).*

(GG-25-1.5-pdl, neuVitro). Transient transfection of pCMV-mTurquoise2-GFP plasmid was done with TransIT-2020 (Mirus), and cells were imaged 24 hours later. During imaging, the cells were maintained at 37°C on a custom-built temperature controlled microscope chamber, while covered with 1.5 ml of imaging media and 2 ml of white mineral oil (VWR) to prevent evaporation. The excitation wavelength was 850 nm, and the emission filter was 470/40 (Chroma). The excitation laser power was adjusted to 4 mW. Becker and Hickl SPCM acquisition parameters were set to 10x zoom, 256x256 image pixels, 5 second integration, and 256 ADC resolution.

### 3.2.7 Software Implementation

All algorithms were implemented in MATLAB. The code used is freely available on Github at `https://github.com/bryankaye1/bayesian-analysis-of-fluorescent-lifetime-data`. Posterior distributions were generated by evaluating the likelihood function in a grid space of parameter values and were marginalized before estimation of the mode and mean for each parameter.

## 3.3 Results

In a sample where only a subset of fluorophores are undergoing FRET, photon emission distributions take the form of a biexponential distribution, with some fraction of the distri-

bution consisting of photons from a short-lifetime exponential, another fraction consisting of photons from a long-lifetime exponential, and some fraction coming from a spurrious background distribution. The goal of FLIM analysis is to infer the relative weights of these distributions, along with the lifetimes of the two exponential distributions, from the measured histogram of photon arrival times (Figure 3.2A). Here we apply an analysis based on Bayesian inference in order to infer the most likely set of parameters from experimentally measured data. The output of our algorithm is a posterior distribution, which gives the relative probability of measuring a given set of parameters (Figure 3.2B). To characterize our approach, we test our analysis in both the low-photon and low-fraction regimes, representing two extremes where data may be collected.

### 3.3.1 Low-Photon Regime

While the biexponential nature of FLIM histograms is apparent when the histogram is constructed using a large number of photons (Figure 3.2A), the histogram's underlying distribution is less obvious when the photon count is low (Figure 3.3A). Previous work has estimated the minimum number of photons necessary to achieve a certain accuracy in determining fluorescence lifetimes from TCSPC measurements(Köllner and Wolfrum, 1992). In this regime it can be difficult to extract accurate estimates of the fraction of short-lifetime photons through methods that rely on histogram fitting. This low-photon regime is relevant in many applications of FLIM, due to the fundamental tradeoff between the number of photons collected and both the spatial-temporal precision of the measurement and the light dose received by the sample. Thus, methods that can improve the precision and accuracy of parameter estimation in the low-photon count regime could potentially lead to a practical increase in spatial-temporal resolution and lower light doses.

In order to test the accuracy and sensitivity of our analysis, fluorescence lifetime measurements were taken using Erythrosin B and Coumarin 153, two reference dyes with well characterized lifetimes of $0.47 \pm 0.02$ ns and $4.3 \pm 0.2$ ns respectively (Boens *et al.*, 2007). These dyes were mixed at a fixed ratio, and fluorescence lifetime measurements were taken

(Figure 3.3A, Materials and Methods) in order to generate a master list of photon arrival times. A fixed number of photons were randomly sampled from the master list in order to construct a histogram of photon arrival times, and analyzed to infer an estimate of the fraction of short-lifetime fluorophores, $f_S$, taken as either the mean or the mode of the posterior distribution, while the known lifetimes were held fixed (Materials and Methods). This process was repeated 300 times in order to produce an error estimate for each given photon count, and was repeated for total photon counts spanning $\approx 3$ orders of magnitude (Figure 3.3B).

We find good agreement between the estimates of the fraction of short-lifetime photons for total photons counts larger than $\approx 200$ photons, using either the posterior mean or posterior mode as a fraction estimate (Figure 3.3B). Slight discrepancies between estimates using the posterior mean and posterior mode are apparent due to truncation and the fact that the posterior distribution is skewed (Figure 3.3B), and thus in general the mode and the mean of the distribution are not equal. As a measure of the error in our parameter estimation, we compute the standard deviation of the estimates from the 300 numerical replicates (Figure 3.3C) for each photon count. Fitting a power law to all data points except for the four smallest photon counts yields an exponent of $-0.48 \pm 0.04$ (95% confidence interval), consistent with the exponent of $-0.5$ predicted from the central limit theorem in the limit of high $n_{photon}$ . This $\sqrt{n_{photon}}$ scaling is also evident for other analysis methods, including the rapid lifetime determination method(Sharman *et al.*, 1999), which has comparable error for high $n_{photon}$.

### 3.3.2 Low-Fraction Regime

We next tested our results in the regime where a relatively large number of photons are collected, but the fraction of photons originating from the short-lifetime component is low. This regime is relevant in systems where a large number of donor molecules are present, but interactions leading to FRET are relatively rare. In order to test the performance of our algorithm in this regime, fluorescence lifetime measurements were taken of Erythrosin B

and Coumarin 153 as representative short- and long-lifetime dyes respectively. Unlike the measurements taken in the low-photon regime, separate fluorescence lifetime measurements were taken for each dye, generating separate master photon histograms (Figure 3.4A). A fixed number of photons could then be numerically sampled from each master histogram in order to create test histograms containing a prescribed fraction of photons originating from the short-lifetime dye, which were then analyzed in order to estimate the short-lifetime fraction while the lifetimes were held fixed at their previously measured values (Materials and Methods). Data was collected at $\approx 1.5 \times 10^5$, $1.2 \times 10^6$, and $4.8 \times 10^6$ counts per second, corresponding to low, medium, and high intensity respectively, and histograms from each intensity were analyzed separately.

Photons were sampled from master curves such that the total number of photons was fixed at $5 \times 10^7$, with a prescribed fraction of photons originating from the short-lifetime distribution. This process was repeated 100 times for each condition. Across orders of magnitude, the short-lifetime fraction estimated from our algorithm varies linearly with the prescribed short-lifetime fraction (Figure 3.4B), with linear fits giving slopes of $0.9933 \pm 0.0026$, $1.0085 \pm 0.0024$, and $1.0106 \pm 0.0031$, and offsets of $0.002000 \pm 0.0484 \times 10^{-4}$, $0.004400 \pm 0.0814 \times 10^{-4}$, and $0.009500 \pm 0.1992 \times 10^{-4}$ for low, medium, and high intensities respectively (95% confidence interval). The estimated short-lifetime fraction differs from the known short-lifetime fraction by a small bias factor, evident by the small positive offsets in the linear fits (Figure 3.4B, Inset). We hypothesize that this offset may be due to a number of factors, including non-monoexponential photon emission from the dyes, slight mischaracterization of the lifetimes or the instrument response function, or an intensity dependence of the FLIM measurement system. While the magnitude of the bias varies with intensity, the magnitude of the bias is relatively small, overestimating the fraction by less than one percent for the highest intensity tested.

In many applications, the changes in FRET fraction are more relevant than the actual fraction values themselves. Thus, we next considered the accuracy of measuring changes in the short-lifetime fraction, which were derived from the results in Figure 3.4B by subtracting

values adjacent on the short-lifetime fraction axis. While the estimated short-lifetime fractions contain a small bias (Figure 3.4B), the bias is largely removed when changes in short-lifetime fraction are considered (Figure 3.4C). Consistent with this removal of bias, fitting linear equations to the estimated changes in short lifetime fraction vs. prescribed short lifetime fraction gives slopes of $0.9573 \pm 0.1895$, $1.0013 \pm 0.1445$, and $0.9580 \pm 0.1717$, and offsets of $(0.2332 \pm 0.3712) \times 10^{-5}$, $(0.3215 \pm 0.3088) \times 10^{-5}$, and $(0.4617 \pm 0.4286) \times 10^{-5}$ for low, medium, and high intensities respectively (95% confidence interval) (Figure 3.4C). These results demonstrate the accuracy and precision of our method for measuring changes in short-lifetime fraction across many orders of magnitude. For a short-lifetime fraction of $2^{-7}$, the sample standard deviation decays with increasing photon number. Fitting a power law yields an exponent of $-0.4764 \pm 0.0471$ (95% confidence interval), consistent with the exponent of $-0.5$ predicted from the central limit theorem and as was the case for the low-photon regime measurements (Figure 3.3C).

### 3.3.3 *In vivo* Testing and Method Comparison

As FLIM is commonly used to measure FRET in living systems between biological fluorophores, which may contain complications not accounted for in our model, we next tested the applicability of our method in living cells. FLIM measurements were carried out on U2OS cells transfected with a plasmid carrying mTurquoise2-4AA-GFP, a fusion between the FRET pair of mTurquoise2 and GFP (Figure 3.4A). As these two fluorophores are physically attached to each other in close proximity, a fraction of the donor mTurquoise2 molecules undergo FRET, and thus have a short lifetime. However, as these fluorophores must undergo maturation before being functional, some fraction of mTurquoise2 molecules will be attached to GFP that are not fully mature and thus will not undergo FRET, leading to a long-lifetime fraction.

To test the performance of our method as a function of the photon number, photon arrival times were pooled within the cell using boxcar windowing, from areas of either 3x3, 7x7, or 11x11 pixels corresponding to average photon counts of 1,087$\pm$260, 5,826$\pm$1,451,

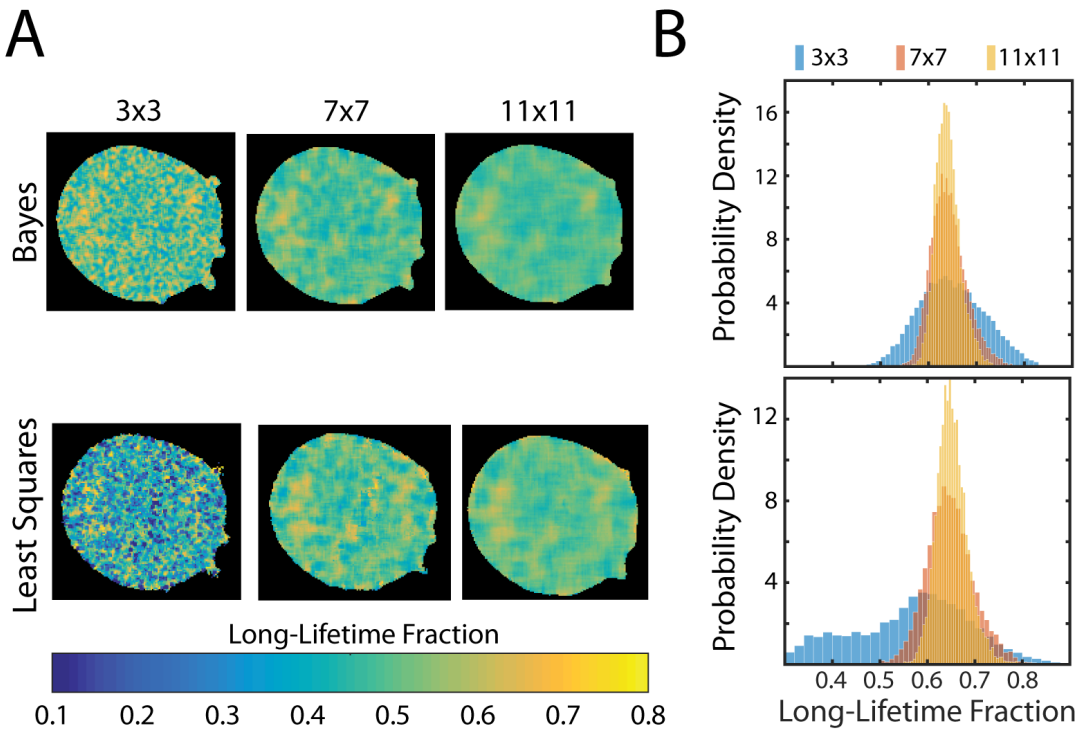


**Figure 3.4:** ***In vivo Testing*** *(A) FLIM images depicting the long-lifetime fraction from measurements of mTurquoise2 in a U2OS cell. Photons were pooled from pixels grouped using boxcar windowing into groups of either 3x3, 7x7, or 11x11 pixels and analyzed using either the Bayesian analysis presented here, or least-squares fitting. (B) Histograms showing the probability density of the long-lifetime fraction from images in (A). The probability density functions from Bayesian analysis were found to have mean values of 0.648±0.069, 0.642±0.037, and 0.640±0.026 (mean ± s.d.) for 3x3, 7x7, and 11x11 binning respectively, while the means values were found to be 0.558±0.137, 0.648±0.050, and 0.652±0.034 (mean ± s.d.) for 3x3, 7x7, and 11x11 binning respectively using least-squares-fitting.*

and 14,105±3,673, respectively (Figure 3.4B). In order to more readily make comparisons with the least-squares method, we here infer the relative amplitudes of the biexponential decay, instead of the relative photon populations previously considered, and thus consider the long-lifetime amplitude fraction instead of the long-lifetime photon fraction considered above. Using the Bayesian method, the distributions of the long-lifetime fraction were found to have mean and standard deviation values of 0.648±0.069, 0.642±0.037, and 0.640±0.026 (mean ± s.d.) for 3x3, 7x7, and 11x11 binning respectively, showing little change for all conditions.

In order to compare the results from the Bayesian method presented here with the more commonly used least-squares fitting method, we repeated our analysis using fitting routines built into the Becker & Hickl software (Figures 3.4A and 3.4B). Mean and standard deviation values of the long-lifetime fraction distributions were found to be 0.558±0.137, 0.648±0.050, and 0.652±0.034 (mean ± s.d.) for 3x3, 7x7, and 11x11 binning respectively. While the mean value for the long-lifetime fraction is similar for higher photon counts, there is significant discrepancy for 3x3 binning, where an asymmetric distribution is evident. Furthermore, for the highest photon counts, the mean values agree within error for the Bayesian method and least-squares fitting, indicating a convergence between the two methods in the limit of high photon number. Thus, for low-photon counts, the Bayesian method presented here provides long-lifetime fraction estimates that are more accurate and precise than the nonlinear least-squares method.

## 3.4 Discussion

Here we presented an extension of previous Bayesian inference approaches to FLIM data analysis that takes into account additional experimental complexities. Using controlled experimental data as a test case, we show that this analysis performs remarkably well in both the low-photon and low-fraction regimes.

In the low-photon regime, we can estimate the low-lifetime fraction, $f_S$, with a precision of 0.003 and a bias of 0.017 using only 200 photons. At a photon collection rate of $2 \times 10^5$

photons per second, this number of photons corresponds to an acquisition time of only 1 millisecond. As the precision scales as $\propto n_{photon}^{-1/2}$ (Figure 3.3C), if one instead wanted a higher precision of 0.001, one could instead collect data for 9 milliseconds. In the low-fraction regime, using $5 \times 10^7$ photons, for a short-lifetime fraction, $f_S$, of 0.0156, we find a precision of 0.000096 and a bias of 0.0046. With an acquisition rate of $1.5 \times 10^6$ photons per second, this corresponds to $\approx$ 33 seconds of acquisition time. As the precision in this regime also scales $\propto n_{photon}^{-1/2}$ (Figure 3.4C), if one requires a higher precision of 0.000032, this could be obtained by acquiring data for nine times as long, or 300 seconds. Thus, in both the low-photon and low-fraction regimes, our results show the required number of photons, and hence the acquisition time, necessary to achieve a given level of precision.

One limitation of our implementation is that we evaluate the posterior distribution at equally spaced points. A large parameter space must be searched, and the analysis presented here is relatively slow compared to other parameter searching techniques. For example, when 4 parameters are searched using a Markov chain Monte Carlo approach to stochastically optimize our likelihood, the computation time is reduced by a factor of $\approx$10-20 with no loss of accuracy (Figure 3.1).

Here we have focused on the use of FLIM to measure changes in FRET, yet it has wider applications, including in metabolic imaging (Bird *et al.*, 2005) and in measuring local changes in environment, including pH (Lin *et al.*, 2003) as well as oxygen (Gerritsen *et al.*, 1997) and $Zn^{2+}$ (Ripoll *et al.*, 2015) concentrations. The analysis presented here is general, and should be applicable to FLIM measurements in these other systems as well.

# Chapter 4

# Measuring NDC80 binding reveals the molecular basis of tension-dependent kinetochore attachments[1]

## 4.1 Introduction

During cell division, chromosome motion is driven by coupling the dynamic ends of microtubules to the kinetochore. Erroneous kinetochore-microtubule attachments are corrected to prevent chromosome mis-segregation. The mechanism of error correction remains poorly understood, but is believed to be based on a tension-dependent interaction between microtubules and the kinetochore (Nicklas and Ward, 1994; Liu *et al.*, 2009; Akiyoshi *et al.*, 2010; Lampson and Cheeseman, 2011; Godek *et al.*, 2014b). The NDC80 complex is the predominant coupler of the kinetochore to microtubules (Cheeseman *et al.*, 2006; DeLuca *et al.*, 2006), and is thus directly implicated in tension sensing for error correction. The lack of techniques to quantify the attachment of the NDC80 complex to microtubules in vivo has been a major obstacle to investigate this possibility. Here, we present a method, based on fluorescence lifetime imaging microscopy and Förster resonance energy trans-

[1]This work is contributed also by Che-Hang Yu and Daniel Needleman.

fer (FLIM-FRET), to quantitatively measure the fraction of NDC80 complexes bound to microtubules at individual kinetochores in living human tissue culture cells. We found that the fraction of NDC80 bound is positively correlated with the distance between sister kinetochores, a proxy for centromere tension. This positive correlation was dependent on the haspin-dependent localization of Aurora B kinase at the centromere. These results argue that error correction results from the tension-dependent modulation of NDC80 binding affinity by centromere-localized Aurora B kinase.

## 4.2 Result

Inspired by previous work (Posch *et al.*, 2010), we sought to develop a Förster Resonance Energy Transfer (FRET) based approach to directly measure the association between the NDC80 complex and kinetochore microtubules (kMTs) in living cells. We engineered U2OS cells stably expressing Nuf2, a subunit of the NDC80 complex, N-terminally labeled with a donor fluorophore, mTurquoise2. In this same cell line, we also inserted a tetracysteine (TC) motif at the C-terminus of $\beta$-tubulin using CRISPR-induced homologous recombination, which becomes a FRET acceptor after binding to the membrane-permeant dye FlAsH (Hoffmann *et al.*, 2005) (Figure 4.1a). The small size of the TC motif minimizes the negative effects of labeling the C-terminus of tubulin, allowing the engineered cells to successfully pass through mitosis (Andresen *et al.*, 2004). We utilized fluorescence lifetime imaging microscopy (FLIM) to quantitatively measure FRET (Berezin and Achilefu, 2010) (Supplementary Figure A.1). To characterize the fluorescence properties of the mTurquoise2-NDC80 complex in the absence of FRET, we first performed FLIM measurement on engineered cells that were not exposed to FlAsH, and found that their fluorescence decay is well-described as a single exponential with a lifetime of 3.75 ns $\pm$ 0.09 ns (s.d.) (Figure 4.1b, Supplementary Figure A.2). After labeling microtubules in the engineered cells with FlAsH, the measured fluorescence decay exhibits significant deviation from a single-exponential model, and is well fit by a sum of two exponentials (Figure 4.1c, Supplementary Figure A.2), one of which has a significantly shorter lifetime than the other (lifetime ratio 0.21 $\pm$ 0.08, s.d.). A

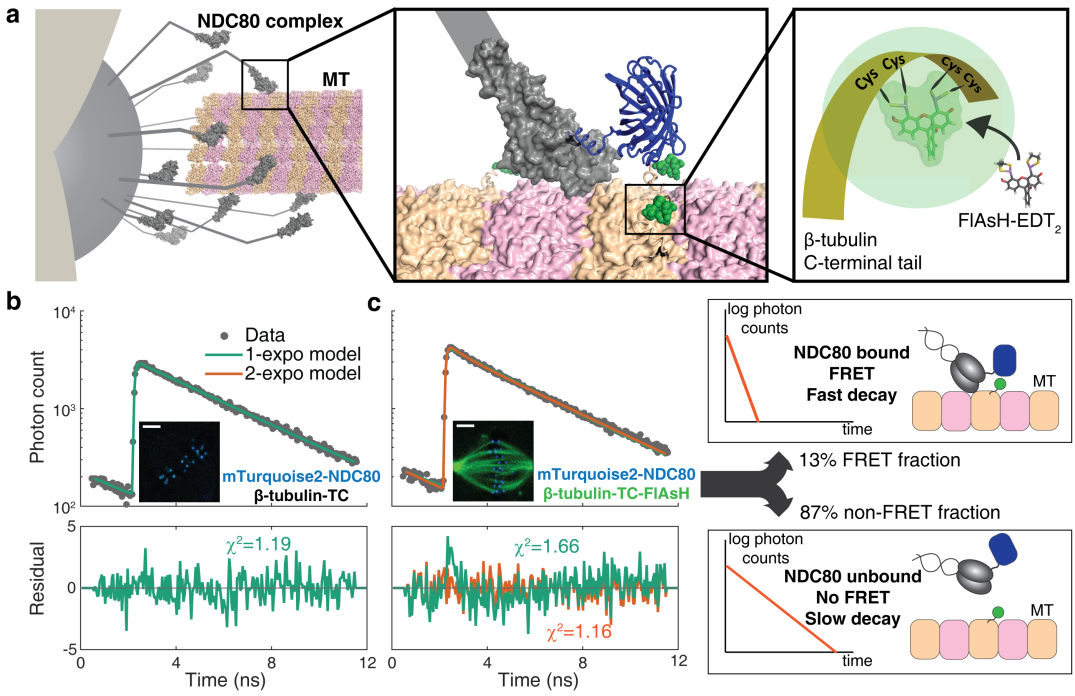


**Figure 4.1:** ***FLIM-FRET measurement of NDC80 binding fraction in human tissue culture cells.*** ***a****, Illustration of mTurquoise2-NDC80 interacting with a microtubule with β-tubulin-TC-FlAsH in the engineered cell line. mTurquoise2 (blue) and TC-FlAsH (green ball).* ***b****, FLIM curves from engineered cells not exposed to FlAsH (gray dots) and* ***c*** *exposed to FlAsH (gray dots). Inserts: images of spindles in the engineered cell lines with or without exposure to FlAsH. 3 µm scale bars. Best estimated single- (green) and double-exponential (orange) models (upper), and associated residuals (lower). The relative amplitude of the fast decay (FRET fraction) in the double-exponential model provides a quantitative measurement of the fraction of NDC80 attached to microtubules.*

two-exponential-decay profile is expected in the presence of FRET, with the longer- and shorter-lifetime exponentials corresponding to the donor fluorophores in a non-FRET state and FRET state, respectively. The relative amplitude of the two decays is a quantitative measurement of the fraction of the donor fluorophores engaged in FRET (Berezin and Achilefu, 2010).

We next investigated the relation between the measured FRET and NDC80-kMT interactions. Cryo-electron microscopy reconstructions indicate that mTurquoise2 N-terminally tagged Nuf2 is only close enough to engage in FRET with TC-FlAsH C-terminally tagged $\beta$-tubulin when the NDC80 complex is bound to the microtubule (Alushin *et al.*, 2010) (Supplementary Figure A.3). An alternative construct with mTurquoise2 conjugated to

the distally located C-terminus of Nuf2 displays only a single long-lifetime state in either the presence or absence of TC-FlAsH at the C-terminus of $\beta$-tubulin (Supplementary Figure A.2), arguing that non-specific interactions do not produce false-positive FRET signals. Taken together, these results demonstrate that the short-lifetime state is the mTurquoise2-NDC80 bound to TC-FlAsH labeled tubulin in kMTs, while the long-lifetime state is the combination of complexes bound to unlabeled tubulin and complexes not bound to kMTs. The relative population of short-lifetime population (referred to as NDC80 FRET fraction) provides a quantitative measurement of the fraction of NDC80 complexes bound to kMTs at kinetochores.

We first used this technique to investigate the regulation of NDC80-kMT binding by Aurora B kinase, a key phosphoregulator in error correction (Cheeseman *et al.*, 2006; DeLuca *et al.*, 2006; Tanaka *et al.*, 2002; Biggins *et al.*, 1999; Ciferri *et al.*, 2008a; Hauf *et al.*, 2003). We added the Aurora B inhibitor, ZM447439, to metaphase cells, and observed an increase in NDC80 FRET fraction over the time course of $\approx$10 minutes, from 12% of complexes bound to $\approx$20% (Figure 4.2a). This result demonstrates that Aurora B-mediated phosphorylation destabilizes NDC80-kMT binding at kinetochores in vivo, which has previously been suggested based on in vitro biochemistry experiments (Cheeseman *et al.*, 2006; Zaytsev *et al.*, 2014, 2015). We performed FLIM measurement on a Nuf2-targeted and cytoplasmic Aurora B FRET biosensor (Fuller *et al.*, 2008), which contains a kinesin-13 family Aurora B substrate whose phosphorylation obstructs intramolecular FRET between mTurquoise2 and YPet. During identical ZM447439 treatment, we found a continual reduction in the fraction of the Aurora B sensors in the non-FRET state, a proxy for Aurora B activity, over a similar time period (Figure 4.2b,c). The non-FRET fraction of the sensor attached to the N-terminus of Nuf2 displayed similar kinetics to that of the cytoplasmic sensor, but consistantly at a higher level, presumably because attaching Nuf2 to YPet impairs the maturation of YPet in the sensor. Plotting the measured NDC80 binding vs. non-FRET fraction of the cytoplamic sensor at each time point revealed a graded relationship between them (Figure 4.2d), consistent with the relationship previously found between the number

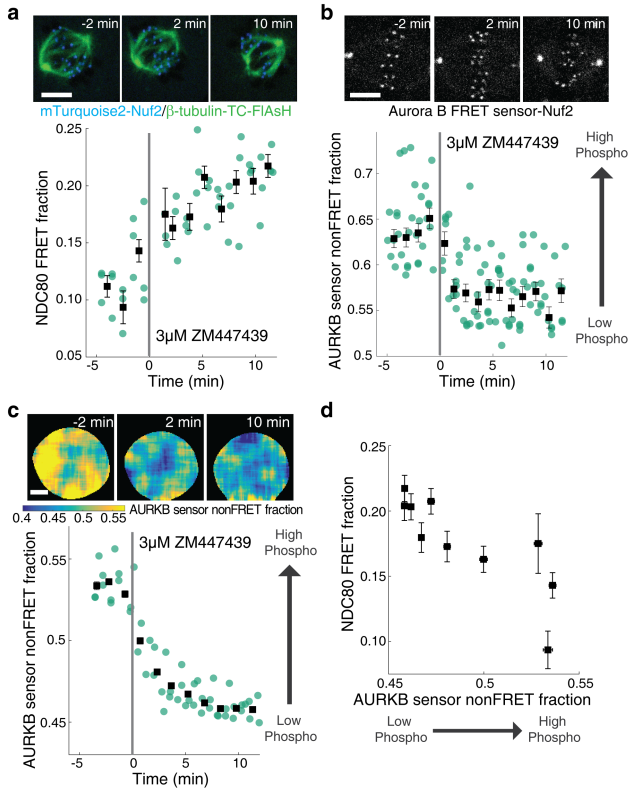


**Figure 4.2:** ***Aurora B regulates NDC80 binding in a graded fashion.*** ***a****, Time course of NDC80 FRET fraction in response to Aurora B inhibition by 3 μM ZM447439 (n = 3 cells). Time course of the non-FRET fraction of the* ***b*** *Nuf2-targeted and* ***c*** *cytoplasmic Aurora B FRET sensor in response to 3 μM ZM447439 (n = 5 and n = 7 cells, respectively). Cells were arrested in metaphase by 10 μM MG-132.* ***d****, NDC80 FRET fraction plotted as a function of cytoplasmic Aurora B FRET sensor non-FRET fraction. Higher non-FRET fraction of the FRET sensor indicates the higher level of phosphorylations by the Aurora B. Black squares and error bars show the weighted mean and the s.d. of the weighted mean of the data points (green circles) in equally spaced time intervals of 1.5 mins for* ***a*** *and* ***c****, or 1 min for* ***b****. 5 μm scale bars.*

of aspartic acid phosphomimetic mutations on truncated NDC80 constructs and their in vitro binding affinity to microtubules (Zaytsev *et al.*, 2014). The increased NDC80-kMT binding after Aurora B inhibition may underlie the reduction in detachment of kMTs from kinetochores after Aurora B inhibition, observed in the measurement of fluorescence activation after photoactivation (Cimini *et al.*, 2006).

To investigate how the NDC80 binding changes in the course of error corrections, we next measured the time course of the NDC80 binding in the cell progressing from prometaphase to metaphase to anaphase. We found that the NDC80 FRET fraction is 7%

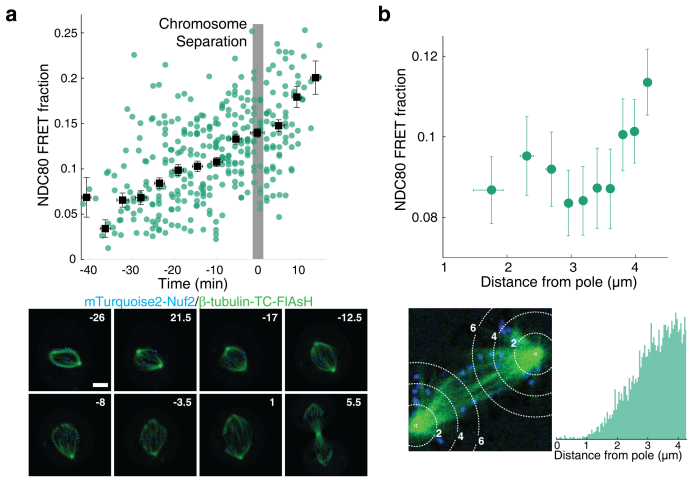


**Figure 4.3:** ***NDC80 binding increases in the course of error correction.*** ***a****, Time course of NDC80 FRET fraction from prometaphase to metaphase to anaphase (23 cells). Black squares and error bars show the weighted mean and the s.d. of the weighted mean of the data points (green circles) in equally spaced time intervals of 4.6 mins. 5 μm scale bar.* ***b****, NDC80 binding fraction as a function of distance between the kinetochore and the closer spindle pole (11 cells, 6265 kinetochores). Data points are the mean within groups of 627 kinetochores with similar distances (except the rightmost point of 622 kinetochores), y-error bars are corresponding s.e.m., and the x-error bars are the standard deviation of distances within that group.*

in early prometaphase, gradually increases to about 14% in late metaphase, and reaches about 20% at the end of anaphase, which is comparable to the level when Aurora B is inhibited (Figure 4.3a). Plotting the NDC80 FRET fraction measured at the kinetochores in prometaphase as a function of distance from the closer spindle pole revealed that NDC80 binding fraction was lower at the kinetochores near the pole. These results suggest that NDC80 binding changes about 2-folds in the course of error correction process, and is regulated differentially at kinetochores in prometaphase. The temporal increase in NDC80-kMT binding may be the basis of the increase in kMT stability from prometaphase to metaphase to anaphase observed in the fluorescence dissipation after photoactivation experiments (Kabeche and Compton, 2013; Zhai *et al.*, 1995).

We next sought to investigate how the interaction between NDC80 and kMTs changes during the chromosome oscillation in metaphase. Chromosome oscillation is associated with the kMT dynamics in a way that the kMTs attached to the kinetochore moving toward (poleward) or away from (anti-poleward) the spindle pole primarily depolymerise and poly-

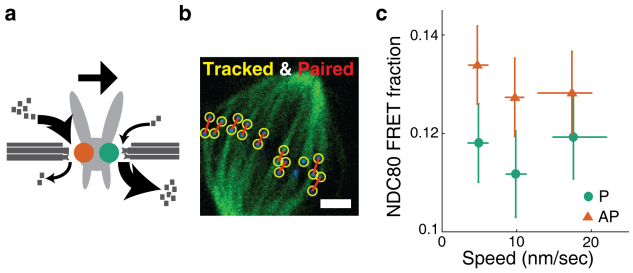


**Figure 4.4:** ***NDC80 complexes preferentially bind to microtubules at anti-poleward-moving kinetochores.*** ***a****, Microtubule depolymerisation is dominant at poleward-moving kinetochore, while polymerisation is dominant at antipoleward-moving kinetochore.* ***b****, Image of a cell with mTurquoise2-NDC80 and β-tubulin-TC-FlAsH, and corresponding kinetochore tracking (yellow circles) and pairing (red lines). 3µm scale bar.* ***c****, NDC80 FRET fraction as a function of kinetochore speed for poleward- (P, green circle) and anti-poleward-moving (AP, orange triangle) kinetochores. Data points are the mean within groups of 681 kinetochores with similar speeds, y-error bars are corresponding s.e.m., and the x-error bars are the standard deviation of speeds within that group.*

merise, respectively (Tirnauer *et al.*, 2002; Armond *et al.*, 2015) (Figure 4.4a). We first asked whether the NDC80 binding is different on the poleward and anti-poleward kinetochores. We acquired time-lapse movies of 17 metaphase cells, tracked their kinetochores, identified sister kinetochores by their relative motions (Figure 4.4b), and quantified the NDC80 binding fraction in groups of kinetochores with similar velocities using FLIM-FRET analysis. We found that the NDC80 binding fraction is higher at anti-poleward kinetochores (12.8% $\pm$ 0.5%, s.e.m.) than poleward kinetochores (11.4% $\pm$ 0.5%, s.e.m.), regardless of their speeds (Figure 4.4c), suggesting that NDC80 preferentially binds to polymerizing kMTs in vivo. The preferential binding is statistically significant ($p<0.05$), yet small, presumably because the anti-poleward and poleward moving kinetochores have a mixture of both polymerising and dispolymerising MTs, rather than MTs purely in either state (Armond *et al.*, 2015). This differential binding of NDC80 provides an explanation for the higher detachment rate of depolymerizing microtubules from kinetochores (Akiyoshi *et al.*, 2010).

The detachment rate of kMTs from kinetochores was shown to also be regulated by tension in classic micromanipulation experiments by Bruce Nicklas (Nicklas and Koch, 1969). Since the NDC80 complex is the predominant coupler of the kinetochore to microtubules (Cheeseman *et al.*, 2006; DeLuca *et al.*, 2006), we hypothesized that the tension-dependent detachment of kMTs results from tension-dependent NDC80-kMT binding. To test this pos-

sibility under physiologically relevant conditions, we investigated the correlation between NDC80 binding and centromere tension, inferred by the distance between sister kinetochores (K-K distance) (Magidson *et al.*, 2011), during chromosome oscillations in metaphase. We used FLIM-FRET analysis to measure the NDC80 binding fraction in groups of sister kinetochores with similar K-K distances, and observed a highly statistically significant positive correlation ($p<0.005$) between NDC80 binding fraction and K-K distance (Figure 4.5a). In the absence of microtubules, the rest length of K-K distance in human cell is 0.73 $\mu$m $\pm$ 0.04 $\mu$m (Tauchman *et al.*, 2015), significantly shorter than the K-K distances during metaphase oscillations. Thus, in order to investigate a wider range of K-K distance, we treated cells with taxol, which reduced K-K distances (0.90 $\mu$m $\pm$ 0.10 $\mu$m, taxol vs. 1.19 $\mu$m $\pm$ 0.19 $\mu$m, untreated, s.d., Figure 4.5b). Combining the data of untreated and taxol-treated cells, we found that the NDC80 binding fraction continually increases with K-K distance over the full range of K-K distance (positive correlation, $p<0.0005$, Figure 4.5a). The extent to which the NDC80 FRET fraction changes from the smallest to the largest K-K distance is comparable to the change from prometaphase to anaphase onset (Figure 4.5a and 4.3a). These results suggest that the tension-dependent detachment of kMTs from kinetochores results from the tension dependency of NDC80-kMT binding, and the tension dependency is strong enough to account for the change in NDC80 binding in the course of error correction.

The mechanism of tension-dependent stabilization of kinetochore-microtubule attachments is controversial (Liu *et al.*, 2009; Akiyoshi *et al.*, 2010; Godek *et al.*, 2014b; Tanaka *et al.*, 2002; Campbell and Desai, 2013; Salimian *et al.*, 2011; Zaytsev *et al.*, 2016). Two different classes of models have been proposed: one based on direct mechanical stabilization (Akiyoshi *et al.*, 2010), and the other by an indirect effect in which tension induces deformation of the centromere which, in turn, alters the phosphoregulation of kinetochores by Aurora B localized at centromeres (Liu *et al.*, 2009; Lampson and Cheeseman, 2011; Salimian *et al.*, 2011; Zaytsev *et al.*, 2016). To test the importance of Aurora B at centromeres, we used the haspin kinase inhibitor, 5-iodotubercidin (5-ITu), which has previously been shown to compromise the recruitment of Aurora B to centromeres by reducing H3T3 phosphorylation

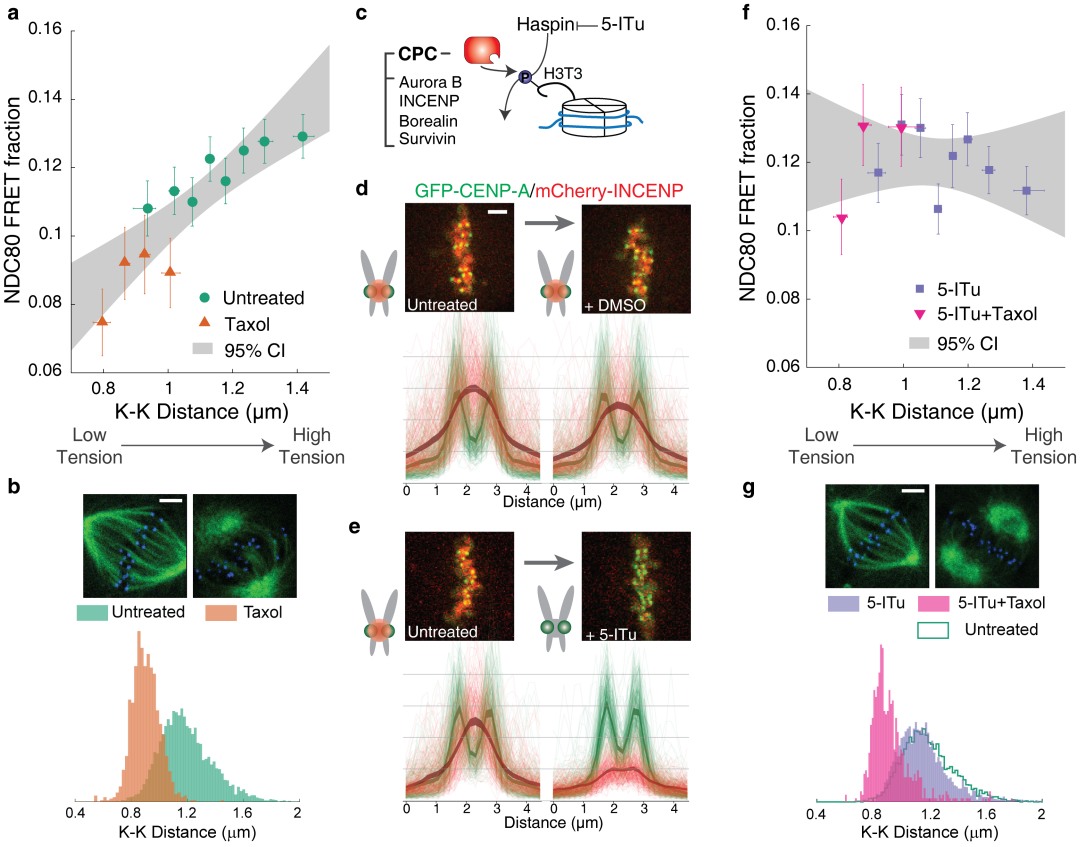


**Figure 4.5:** ***Centromere tension regulates NDC80 binding by the haspin-dependent localization of Aurora B at the centromere.*** *__a__, NDC80 FRET fraction vs. K-K distance for untreated cells (17 cells, 4542 kinetochore pairs, green circle) and cells treated with 10 μM taxol (7 cells, 1113 kinetochore pairs, orange upward triangle), and __b__, corresponding histogram of K-K distances in the same colors. __c__, haspin kinase phosphorylates H3 at Thr3 (H3T3), which recruits the chromosome passenger complex (CPC) to centromeres. 5-Iodotubercidin (5-ITu) inhibits haspin kinase and therefore removes Aurora B localization at centromere. Images of cell with GFP-CENP-A (green) and mCherry-INCENP (red) before and >10 min after __d__ DMSO and __e__ 10 μM 5-ITu treatment, and corresponding intensity profiles along the lines through kinetochore pairs. 3 μm scale bar. __f__, NDC80 FRET fraction vs. K-K distance for cells treated with 10 μM 5-ITu (12 cells, 4540 kinetochore pairs, purple square) and with both 10 μM 5-ITu and 10 μM taxol (3 cells, 702 kinetochore pairs, pink downward triangle). In __a__ and __f__, data points are the mean within groups of kinetochores with similar K-K distances, y-error bars are the corresponding s.e.m., and x-error bar is the standard deviation of K-K distances in each group. Gray regions represent the 95% confidence intervals for the fitted linear models.*

(Wang *et al.*, 2012) (Figure 4.5c). After 10 minutes of exposure of cells to 5-ITu, INCENP, a member of the chromosome passenger complex, which also includes Aurora B (Carmena *et al.*, 2012), was no longer visible at centromeres (Figure 4.5d). Treating cells with 5-ITu for over 15 minutes did not significantly alter the average K-K distances (1.16 $\mu$m $\pm$ 0.18 $\mu$m, 5-ITu-treated vs. 1.19 $\mu$m $\pm$ 0.19 $\mu$m, untreated, s.d.) or the overall average fraction of NDC80 bound to kMTs (11.79% $\pm$ 0.02%, 5-ITu-treated vs. 11.87% $\pm$ 0.02%, untreated, s.e.m.), but eliminated the correlation between K-K distance and NDC80-kMT binding (Figure 4.5f,g). We found that the Aurora B activity at the N-terminus of Nuf2 did not change significantly after 5-ITu treatment (Figure A.4), which accounts for the average NDC80 FRET fraction unaltered after haspin inhibition. In order to investigate a wider range of K-K distance, we treated cells with both taxol and 5-ITu, and found no correlation between NDC80-kMT binding and K-K distance over the full range of K-K distance (Figure 4.5f). Thus, the tension-dependency of NDC80-kMT binding in human tissue culture cells depends on Aurora B localization to centromeres, arguing in favor of models in which phosphorylation plays a central role in chromosome autonomous error correction.

## 4.3 Discussion

To summarize, we have developed a FLIM-FRET based technique to quantitatively measure the fraction of NDC80 complexes attached to kMTs in human tissue culture cells. Using this approach, we found that Aurora B modulates NDC80-kMT binding in a graded fashion in vivo, and that NDC80-kMT binding increases through error correction process from prometaphase to metaphase. Kinetochores in prometaphase displayed different levels of NDC80 binding depending on the distance from the pole. We also observed that NDC80-kMT attachments are dependent on the kMT dynamics, and on the centromere tension in a manner that relies on haspin-dependent Aurora B localization at centromeres. The NDC80 binding at the lowest tension after taxol treatment exhibited the NDC80 binding level in early prometaphase, while at the highest tension the level was similar to that near metaphase to anaphase transition.

Interestingly, the dislocation of Aurora B by the inhibition of haspin did not alter either Aurora B activity at the kinetochores or the binding of NDC80 to the kMTs. This is presumably due to the remaining kinetochore pool of Aurora B recruited by phosphorylated H2AT120, which is generated by kinetochore-localized Bub1 kinase (Yamagishi *et al.*, 2010). Taken together, these results suggest that the haspin-dependent centromere pool of Aurora B provides tension-dependent phosphoregulation of NDC80 as the basis of chromosome autonomous error correction, while the Bub1-dependent kinetochore pool of Aurora B is required to maintain the basal phosphorylation level of NDC80. We believe that the FLIM-FRET technique of measuring NDC80-kMT binding is a powerful tool to further dissect the molecular mechanisms of kinetochore function.

## 4.4 Material and Method

**Cell culture.** U2OS cell lines were maintained in Dulbecco's modified Eagle's medium (DMEM, Gibco) supplemented with 10% Fetal Bovine Serum (FBS, Gibco), and 50 IU $ml^{-1}$ penicillin and 50 g $ml^{-1}$ streptomycin (Gibco) at 37 °C in a humidified atmosphere with 5% $CO_2$. Cells were validated as mycoplasma free by PCR-based mycoplasma detection kit (Sigma Aldrich).

**mTurquoise2-NDC80/$\beta$-tubulin-TC-FlAsH stable cell line.** A tetracysteine (TC) tag, CCPGCC, was genetically attached to the C-terminal end of tubulin beta class I (TUBB), an isotype of $\beta$-tubulin that is predominantly expressed in most cancer cells (Leandro-García *et al.*, 2010). The attachment of the TC tag was achieved by CRISPR-induced homologous recombination to ensure the consistently high expression of labeled $\beta$-tubulin, using the protocol shown in Ran *et al.* (2013). ssDNA (IDT) with the DNA sequence of TC tag (5'-TGCTGTCCCGGCTGTTGC-3') and ∼80 bp-long homology arms was used as a donor DNA. pSpCas9(BB)-2A-GFP (gift from Feng Zhang, Addgene plasmid # 48138) was utilized as a backbone for the plasmid carrying a sgRNA (5'-GAGGCCGAAGAGGAGGCCUA-3') and Cas9. The plasmid and the donor ssDNA were simultaneously delivered into U2OS

cells by nucleofection (Nucleofector 2b, Lonza). The insertion of the TC tag was verified through a PCR-based genotyping with primers 5′-GCATGGACGAGATGGAGTTCAC-3′ and 5′-CCAGCCGTGTTTCCCTAAATAAG-3′ and through a fluorescence imaging after FlAsH-$EDT_2$ staining. The fraction of $\beta$-tubulin labeled with TC-FlAsH was determined to be 26.1% $\pm$ 5.4% (Appendix B).

The U2OS cells expressing TC-tagged $\beta$-tubulin were further engineered to stably express Nuf2 N-terminally labeled with mTurquoise2 by retroviral transfection, three times with different antibiotic selections, 1 $\mu$g $ml^{-1}$ puromycin, 2 $mu$g $ml^{-1}$ blasticidin, and 200 $\mu$g $ml^{-1}$ hygromycin (all from Gibco), in order to achieve a high expression level of the labeled Nuf2. The retroviral vectors and their information are available on Addgene (plasmid #: 80760, 80761, 80762). Monoclonal cell line was obtained by single cell sorting.

**FlAsH-$EDT_2$ staining.** The protocol for the association of FlAsH-$EDT_2$ with $\beta$-tubulin-TC in cell was adapted from Hoffmann *et al.* (2010) so as to maximize the labeling fraction while maintaining cell viability. The U2OS cells expressing $\beta$-tubulin-TC were grown to 80-90% confluency in a 30-mm cell culture dish, and then were gently washed with Opti-MEM (Gibco) twice, and then stained in 2 ml Opti-MEM containing 1 $\mu$M FlAsH-$EDT_2$ (Molecular Probes) for 2 hours. To reduce the non-specific binding of FlAsH, the stained cells were subsequently incubated in Opti-MEM containing 250 $\mu$M 1,2-Ethanedithiol (EDT, Alfa Aesar) for 10 minutes, followed by a gentle wash with Opti-MEM. The cells were incubated in DMEM with 10% FBS for 6-10 hours before imaging, because they were found to be interphase-arrested for the first $\sim$5 hours after the incubation with 250 $\mu$M EDT. Every buffers and media above were pre-warmed at 37 °C before use. All incubation steps were performed at 37 °C in a humidified atmosphere with 5% $CO_2$.

**Aurora B kinase activity measurement.** To measure Aurora B activity in the cytoplasm or at the N-terminus of Nuf2, we used U2OS cells transiently transfected with Aurora B-sensor targeted to Nuf2, or stably expressing Aurora B FRET sensor in the cytoplasm, respectively.

The vectors carrying targeted and untargeted Aurora B FRET sensor (available on Addgene, plasmid # 83286) was modified from the construct developed by Fuller *et al.* (2008) (gift from Michael Lampson, Addgene plasmid # 45215) by replacing CyPet with mTurquoise2. The non-FRET fraction of the Aurora B FRET sensor, which is proportional to the Aurora B activity, was measured by FLIM-FRET with 865 nm exciation laser and 470/40 emission filter (Chroma).

**GFP-CENP-A/mCherry-INCENP line intensity profile measurement.** U2OS cells stably expressing GFP-CENP-A was transiently transfected with mCherry-INCENP (gift from Micheal Lampson). Two-color 3D timelapse fluorescence imaging was performed on spinning disk confocal microscope equipped with objective piezo stage (P-725, Physik Instrumente) and 488-nm and 560-nm excitation lasers. The cells were arrested in metaphase by 10 $\mu$M MG-132 (Sigma Aldrich). Five images were acquired before and 10 mins after DMSO or 10 $\mu$M 5-ITu. Kinetochores were identified by using blob detection algorithm in scikit-image package in Python, and the sister kinetochores were paired based on the pairwise distances and orientations. Intensity profiles along the lines through the paired kinetochores were generated for every detected kinetochore pair. mean $\pm$ 2$\times$s.e.m. region was calculated and presented as shaded region in the figures.

**Live-cell FLIM-FRET measurement.** Detailed instrumental setup and step-by-step protocol are as described previously in Yoo and Needleman (2016). FLIM measurements were performed on a Nikon Eclipse Ti microscope using two-photon excitation from a Ti:Sapphire pulsed laser (Mai-Tai, Spectral-Physics) with an 80-MHz repetition rate and $\sim$70-fs pulse width, a galvanometer scanner (DCS-120, Becker & Hickl), TCSPC module (SPC-150, Becker & Hickl) and hybrid detectors (HPM-100-40, Becker & Hickl). Objective piezo stage (P-725, Physik Instrumente) and motorized stage (ProScan II, Prior Scientific) were used to perform multi-dimensional acquisition, and motor-driven shutter (Sutter Instrument) was used to block the excitation laser between acquisitions. The wavelength of the excitation laser was

set to 865 nm. 470/24 and 525/30 bandpass emission filters (Chroma) and a dichroic beam splitter (FF506-Di03, Semrock) were used for the simultaneous detection of mTurquoise2 and FlAsH fluorescence. The excitation laser was expanded to overfill the back-aperture of a water-immersion objective (CFI Apo 40× WI, NA 1.25, Nikon). The power of the excitation laser was adjusted to 1.1-1.5 mW at the objective. All the electronics were controlled by SPCM software (Becker & Hickl) and $\mu$Manager (Edelstein *et al.*, 2014).

Cells were grown on a 25-mm diameter, #1.5-thickness, round coverglass coated with poly-D-lysine (GG-25-1.5-pdl, neuVitro) to 80-90% confluency. The cells were incubated in imaging media, which is FluoroBrite$^{TM}$ DMEM (Gibco) supplemented with 4 mM L-glutamine (Gibco) and 10 mM HEPES, for 15-30 minutes before imaging. The coverglass was mounted on a custom-built temperature controlled microscope chamber at 37 °C, while covered with 1.5 ml of imaging media and 2 ml of white mineral oil (VWR). An objective heater (Bioptech) was used to maintain the objective at 37 °C. We confirmed that the cells can normally divide longer than 6 hours in this condition. Only metaphase cells displaying proper chromosome alignment and a high expression level of mTurquoise2-Nuf2 were selected for imaging and analysis.

**Kinetochore tracking and pair identification.** We built a MATLAB graphical user interphase (GUI) to import Becker & Hickl FLIM data, track kinetochores, identify kinetochore pairs, extract the FLIM curve from each kinetochore, and estimate the FLIM parameters using a nonlinear least-squared fitting or Bayesian inference. The GUI also allows the users to scrutinize and manually correct the kinetochore trajectories and pairing. The kinetochore tracking algorithm was adapted from a particle tracking algorithm developed by Pelletier *et al.* (2009), and the pair identification was performed by selecting pairs of kinetochores with distances and velocity correlations in certain range. Correction for cell movement is done by measuring correlation between two consecutive spindle images.

**Bayesian FLIM-FRET analysis.** The Bayesian FLIM-FRET analysis was performed as de-

scribed previously (Yoo and Needleman, 2016; Kaye *et al.*, 2017). Negative control FLIM measurements on cells not incubated with FlAsH were performed every day before experiments to determine the long non-FRET lifetime. The short FRET lifetime was estimated by performing a two-exponential FLIM-FRET analysis on the aggregated FLIM data of each cell stained with FlAsH while fixing the non-FRET lifetime to the value pre-determined from the negative control. Then we computed the posterior distribution of the FRET fraction in each kinetochore by performing a two-exponential Bayesian FLIM-FRET analysis while fixing both FRET and non-FRET lifetimes. To compute the mean and the standard error of the mean (s.e.m.) of the FRET fraction in a group of kinetochores, every posterior distribution computed at each kinetochore in the group was multiplied, and the posterior mean and standard deviation were evaluated.

**Drug treatments.** Aurora B inhibition was performed by adding 3 $\mu$M of ZM447439 (Enzo Life Sciences or EMD Millipore) during imaging. Taxol (Sigma Aldrich) treatment was performed at 10 $\mu$M final concentration for >20 minutes. For the haspin kinase inhibition, cells were treated with 10 $\mu$M 5-iodotubercidin (5-ITu, Enzo Life Sciences) for >15 minutes. The double treatment of 5-ITu and taxol shown in Figure 4.5 was performed sequentially by treating cells with 10 $\mu$M taxol and then adding 10 $\mu$M 5-ITu.

**Protein structures.** The protein structures presented in Figure 4.1 and Figure A.3 are based on structure entries in RCSB PDB (www.rcsb.org): PDB ID 3JAS (Zhang *et al.*, 2015) and 3IZ0 (Alushin *et al.*, 2010) for the truncated NDC80 complex and microtubule, and 4B5Y (unpublished) for mTurquoise2. Unknown structures, which includes the linker between mTurquoise2 and Nuf2 (GMDELYKYSDLMET), and C-terminal tail of $\beta$-tubulin with tetracysteine, were predicted by PEP-FOLD3 (Lamiable *et al.*, 2016). Images were rendered by The PyMOL Molecular Graphics System, Version 1.8 Schrödinger, LLC.

# References


Adams, R. R., Wheatley, S. P., Gouldsworthy, A. M., Kandels-Lewis, S. E., Carmena, M., Smythe, C., Gerloff, D. L. and Earnshaw, W. C. (2000). Incenp binds the aurora-related kinase airk2 and is required to target it to chromosomes, the central spindle and cleavage furrow. *Current biology*, **10** (17), 1075–8.

Akiyoshi, B., Sarangapani, K., Powers, A., Nelson, C., Reichow, S., Arellano-Santoyo, H., Gonen, T., Ranish, J., Asbury, C. and Biggins, S. (2010). Tension directly stabilizes reconstituted kinetochore-microtubule attachments. *Nature*, **468** (7323), 576–579.

Alushin, G. M., Ramey, V. H., Pasqualato, S., Ball, D. A., Grigorieff, N., Musacchio, A. and Nogales, E. (2010). The ndc80 kinetochore complex forms oligomeric arrays along microtubules. *Nature*, **467** (7317), 805–810.

Andresen, M., Schmitz-Salue, R. and Jakobs, S. (2004). Short tetracysteine tags to beta-tubulin demonstrate the significance of small labels for live cell imaging. *Molecular biology of the cell*, **15** (12), 5616–22.

Armond, J., Vladimirou, E., Erent, M., McAinsh, A. and Burroughs, N. (2015). Probing microtubule polymerisation state at single kinetochores during metaphase chromosome motion. *Journal of cell science*, **128** (10), 1991–2001.

Asbury, C., Tien, J. and Davis, T. (2011). Kinetochores' gripping feat: conformational wave or biased diffusion? *Trends in cell biology*, **21** (1), 38–46.

Asbury, C. L., Gestaut, D. R., Powers, A. F., Franck, A. D. and Davis, T. N. (2006). The dam1 kinetochore complex harnesses microtubule dynamics to produce force and movement. *Proceedings of the National Academy of Sciences of the United States of America*, **103** (26), 9873–8.

Bakhoum, Thompson and Manning (2009). Genome stability is ensured by temporal control of kinetochore–microtubule dynamics.

Becker, W. (2012a). *The bh TCSPC Handbook*. Becker & Hickl GmbH, 5th edn.

— (2012b). *The bh TCSPC Handbook*. Becker & Hickl GmbH, 5th edn.

Berezin, M. Y. and Achilefu, S. (2010). Fluorescence lifetime measurements and biological imaging. *Chemical Reviews*, **110** (5), 2641–2684.

Bharadwaj, R., Qi, W. and Yu, H. (2004). Identification of two novel components of the human ndc80 kinetochore complex. *Journal of Biological Chemistry*, **279** (13), 13076–13085.

Bianconi, E., Piovesan, A., Facchin, F., Beraudi, A., Casadei, R., Frabetti, F., Vitale, L., Pelleri, M. C., Tassani, S., Piva, F., Perez-Amodio, S., Strippoli, P. and Canaider, S. (2013). An estimation of the number of cells in the human body. *Annals of Human Biology*, **40** (6), 463–471.

Biggins, S., Severin, F., Bhalla, N., Sassoon, I., Hyman, A. and Murray, A. (1999). The conserved protein kinase ipl1 regulates microtubule binding to kinetochores in budding yeast. *Genes & Development*, **13** (5), 532–544.

Bird, D., Yan, L., Vrotsos, K., Eliceiri, K. and Vaughan, E. (2005). Metabolic mapping of MCF10A human breast cells via multiphoton fluorescence lifetime imaging of the coenzyme NADH. *Cancer Research*.

Bishop, J. and Schumacher, J. (2002). Phosphorylation of the carboxy-terminus of incenp by the aurora b kinase stimulates aurora b kinase activity. *Journal of Biological Chemistry*, **277** (31), 27577–27580.

Boens, N., Qin, W., Basarić, N., Hofkens, J., Ameloot, M., Pouget, J., Lefèvre, J. P., Valeur, B., Gratton, E., Martin, v., Silva, N. D., Engelborghs, Y., Willaert, K., Sillen, A., Rumbles, G., Phillips, D., Visser, A. J., van Hoek, A., Lakowicz, J. R., Malak, H., Gryczynski, I., Szabo, A. G., Krajcarski, D. T., Tamai, N. and Miura, A. (2007). Fluorescence lifetime standards for time and frequency domain fluorescence spectroscopy. *Analytical Chemistry*, **79** (5), 2137–49.

Bogdanov, A., Kudryavtseva, E. and Lukyanov, K. (2012). Anti-fading media for live cell gfp imaging. *PLoS ONE*, **7** (12), e53004.

Brinkley, B. R. and Stubblefield, E. (1966). The fine structure of the kinetochore of a mammalian cell in vitro. *Chromosoma*, **19** (1), 28–43.

Campbell, C. and Desai, A. (2013). Tension sensing by aurora b kinase is independent of survivin-based centromere localization. *Nature*, **497** (7447), 118–21.

Carmena, M., Wheelock, M., Funabiki, H. and Earnshaw, W. (2012). The chromosomal passenger complex (cpc): from easy rider to the godfather of mitosis. *Nature reviews. Molecular cell biology*, **13** (12), 789–803.

Casella and George (1992). Explaining the gibbs sampler.

Chang, C., Sud, D. and Mycek, M. (2007). Fluorescence lifetime imaging microscopy. *Methods in cell biology*.

Cheeseman, I., Chappie, J., Wilson-Kubalek, E. and Desai, A. (2006). The conserved kmn network constitutes the core microtubule-binding site of the kinetochore. *Cell*, **127** (5), 983–997.

— and Desai, A. (2008). Molecular architecture of the kinetochore–microtubule interface. *Nature Reviews Molecular Cell Biology*, **9** (1), 33–46.

Chen, W., Gielen, F., Laine, R., Harding, H. and Hollfelder, F. (2015). A method to quantify FRET stoichiometry with phasor plot analysis and acceptor lifetime ingrowth. *Biophysical journal*.

Chen, Y., Saulnier, J., Yellen, G. and Sabatini, B. (2014). A pka activity sensor for quantitative analysis of endogenous gpcr signaling via 2-photon fret-flim imaging. *Frontiers in Pharmacology*, **5**, 56.

Ciferri, C., Pasqualato, S., Screpanti, E., Varetti, G., Santaguida, S., Dos Reis, G., Maiolica, A., Polka, J., De Luca, J. G., De Wulf, P. *et al.* (2008a). Implications for kinetochore-microtubule attachment from the structure of an engineered ndc80 complex. *Cell*, **133** (3), 427–439.

—, —, —, —, —, Reis, G., Maiolica, A., Polka, J., Luca, J., Wulf, P. and et al. (2008b). Implications for kinetochore-microtubule attachment from the structure of an engineered ndc80 complex. *Cell*, **133** (3), 427–39.

Cimini and Degrassi (2005). Aneuploidy: a matter of bad connections.

Cimini, D., Wan, X., Hirel, C. and Salmon, E. (2006). Aurora kinase promotes turnover of kinetochore microtubules to reduce chromosome segregation errors. *Current Biology*, **16** (17), 1711–1718.

Colyer, R. and Siegmund, O. (2012). Phasor imaging with a widefield photon-counting detector. *Journal of Biomedical Optics*.

Cooke, C. A., Heck, M. M. and Earnshaw, W. C. (1987). The inner centromere protein (incenp) antigens: movement from inner centromere to midbody during mitosis. *The Journal of cell biology*, **105** (5), 2053–67.

Coue, M., Lombillo, V. A. and McIntosh, J. R. (1991). Microtubule depolymerization promotes particle and chromosome movement in vitro. *The Journal of Cell Biology*, **112** (6), 1165–1175.

DeLuca, J. G., Gall, W. E., Ciferri, C., Cimini, D., Musacchio, A. and Salmon, E. D. (2006). Kinetochore microtubule dynamics and attachment stability are regulated by hec1. *Cell*, **127** (5), 969–982.

Dong, Y., Vanden Beldt, K. J., Meng, X., Khodjakov, A. and McEwen, B. F. (2007). The outer plate in vertebrate kinetochores is a flexible network with multiple microtubule interactions. *Nature cell biology*, **9** (5), 516–22.

Dumontet, C., Durán, G., Steger, K., Murphy, G., Sussman, H. and Sikic, B. (1996). Differential expression of tubulin isotypes during the cell cycle. *Cell Motility and the Cytoskeleton*, **35** (1), 49–58.

Earnshaw, W. C. and Rothfield, N. (1985). Identification of a family of human centromere proteins using autoimmune sera from patients with scleroderma. *Chromosoma*, **91** (3-4), 313–21.

Ebrecht, R., Paul, C. and Wouters, F. (2014). Fluorescence lifetime imaging microscopy in the medical sciences. *Protoplasma*, **251** (2), 293–305.

Edelstein, A. D., Tsuchida, M. A., Amodaj, N., Pinkard, H., Vale, R. D. and Stuurman, N. (2014). Advanced methods of microscope control using $\mu$manager software. *Journal of biological methods*, **1** (2).

Espenel, C., Acharya, B. R. and Kreitzer, G. (2013). A biosensor of local kinesin activity reveals roles of pkc and eb1 in kif17 activation. *The Journal of cell biology*, **203** (3), 445–55.

Festy, F., Ameer-Beg, S., Ng, T. and Suhling, K. (2007). Imaging proteins in vivo using fluorescence lifetime microscopy. *Molecular bioSystems*, **3** (6), 381–91.

Fuller, B., Lampson, M., Foley, E., Rosasco-Nitcher, S., Le, K., Tobelmann, P., Brautigan, D., Stukenberg, T. and Kapoor, T. (2008). Midzone activation of aurora b in anaphase produces an intracellular phosphorylation gradient. *Nature*, **453** (7198), 1132–1136.

Galli, R., Uckermann, O., Andresen, E., Geiger, K., Koch, E., Schackert, G., Steiner, G. and Kirsch, M. (2014). Intrinsic indicator of photodamage during label-free multiphoton microscopy of cells and tissues. *PLoS ONE*, **9** (10), e110295.

Gavet, O. and Pines, J. (2010). Progressive activation of cyclinb1-cdk1 coordinates entry to mitosis. *Developmental Cell*, **18** (4), 533–543.

Gelman, A., Carlin, J. B., Stern, H. S., Dunson, D. B., Vehtari, A. and Rubin, D. B. (2013). *Bayesian Data Analysis*. Chapman & Hall/CRC Texts in Statistical Science (Book 106), Chapman and Hall/CRC, 3rd edn.

Geman, S. and Geman, D. (1984). Stochastic relaxation, gibbs distributions, and the bayesian restoration of images. *IEEE Transactions on pattern analysis and machine intelligence*, (6), 721–741.

Gerritsen, H., Sanders, R., Draaijer, A. and Ince, C. (1997). Fluorescence lifetime imaging of oxygen in living cells. *Journal of Fluorescence*.

Godek, Kabeche and Compton (2014a). Regulation of kinetochore-microtubule attachments through homeostatic control during mitosis.

—, — and — (2014b). Regulation of kinetochore-microtubule attachments through homeostatic control during mitosis.

Goedhart, J., von Stetten, D., Noirclerc-Savoye, M., Lelimousin, M., Joosen, L., Hink, M., van Weeren, L., Gadella, T. and Royant, A. (2012). Structure-guided evolution of cyan fluorescent proteins towards a quantum yield of 93%. *Nature communications*, **3**, 751.

Gordon, Resio and Pellman (2012a). Causes and consequences of aneuploidy in cancer.

—, — and — (2012b). Causes and consequences of aneuploidy in cancer.

Grishchuk, E. and McIntosh, R. (2006). Microtubule depolymerization can drive poleward chromosome motion in fission yeast. *The EMBO journal*, **25** (20), 4888–4896.

Gruneberg, U., Neef, R., Honda, R., Nigg, E. A. and Barr, F. A. (2004). Relocation of aurora b from centromeres to the central spindle at the metaphase to anaphase transition requires mklp2. *The Journal of cell biology*, **166** (2), 167–72.

Guimaraes, G. J., Dong, Y., McEwen, B. F. and Deluca, J. G. (2008). Kinetochore-microtubule attachment relies on the disordered n-terminal tail domain of hec1. *Current biology*, **18** (22), 1778–84.

Hauf, S., Cole, R., LaTerra, S., Zimmer, C., Schnapp, G., Walter, R., Heckel, A., van Meel, J., Rieder, C. and Peters, J.-M. (2003). The small molecule hesperadin reveals a role for aurora b in correcting kinetochore–microtubule attachment and in maintaining the spindle assembly checkpoint. *The Journal of Cell Biology*, **161** (2), 281–294.

Hess, S. and Webb, W. (2002). Focal volume optics and experimental artifacts in confocal fluorescence correlation spectroscopy. *Biophysical journal*, **83** (4), 2300–17.

Hill, T. L. (1985). Theoretical problems related to the attachment of microtubules to kinetochores. *Proceedings of the National Academy of Sciences of the United States of America*, **82** (13), 4404–8.

Hiller, G. and Weber, K. (1978). Radioimmunoassay for tubulin: a quantitative comparison of the tubulin content of different established tissue culture cells and tissues. *Cell*, **14** (4), 795–804.

Hinde, E., Digman, M. and Hahn, K. (2013). Millisecond spatiotemporal dynamics of FRET biosensors by the pair correlation function and the phasor approach to FLIM. *Proceedings of the National Academy of Sciences of the United States of America*.

Hoffmann, C., Gaietta, G., Bünemann, M., Adams, S., Oberdorff-Maass, S., Behr, B., Vilardaga, J.-P., Tsien, R., Ellisman, M. and Lohse, M. (2005). A flash-based fret approach to determine g protein-coupled receptor activation in living cells. *Nature methods*, **2** (3), 171–6.

—, —, Zürn, A., Adams, S., Terrillon, S., Ellisman, M., Tsien, R. and Lohse, M. (2010). Fluorescent labeling of tetracysteine-tagged proteins in intact cells. *Nature protocols*, **5** (10), 1666–77.

Honda, R., Körner, R. and Nigg, E. A. (2003). Exploring the functional interactions between aurora b, incenp, and survivin in mitosis. *Molecular biology of the cell*, **14** (8), 3325–41.

Hopt, A. and Neher, E. (2001). Highly nonlinear photodamage in two-photon fluorescence microscopy. *Biophysical Journal*, **80** (4).

Howe, M., McDonald, K., Albertson, D. and Meyer, B. (2001). Him-10 is required for kinetochore structure and function on caenorhabditis elegans holocentric chromosomes. *The Journal of Cell Biology*, **153** (6), 1227–1238.

Inoué, S. and Salmon, E. (1995). Force generation by microtubule assembly/disassembly in mitosis and related movements. *Molecular Biology of the Cell*, **6** (12), 1619–1640.

Kabeche, L. and Compton, D. (2013). Cyclin a regulates kinetochore microtubules to promote faithful chromosome segregation. *Nature*, **502** (7469), 110–113.

Kaitna, S., Mendoza, M., Jantsch-Plunger, V. and Glotzer, M. (2000). Incenp and an aurora-like kinase form a complex essential for chromosome segregation and efficient completion of cytokinesis. *Current biology*, **10** (19), 1172–81.

Kapoor, T., Lampson, M., Hergert, P. and Cameron, L. (2006). Chromosomes can congress to the metaphase plate before biorientation. . . . .

Kaye, B., Foster, P., Yoo, T. and Needleman, D. (2017). Developing and testing a bayesian analysis of fluorescence lifetime measurements. *PLOS ONE*, **12** (1), e0169337.

Kelly, A. E., Ghenoiu, C., Xue, J. Z., Zierhut, C., Kimura, H. and Funabiki, H. (2010). Survivin reads phosphorylated histone h3 threonine 3 to activate the mitotic kinase aurora b. *Science (New York, N.Y.)*, **330** (6001), 235–9.

Köllner, M. and Wolfrum, J. (1992). How many photons are necessary for fluorescence-lifetime measurements? *Chemical Physics Letters*, **200** (1), 199–204.

Koshland, D. E., Mitchison, T. J. and Kirschner, M. W. (1988). Polewards chromosome movement driven by microtubule depolymerization in vitro. *Nature*, **331** (6156), 499–504.

Lakowicz, J. R. (2011a). *Principles of Fluorescence Spectroscopy*. Springer, 3rd edn.

— (2011b). *Principles of Fluorescence Spectroscopy*. Springer, 3rd edn.

Lamiable, A., Thévenet, P., Rey, J., Vavrusa, M., Derreumaux, P. and Tufféry, P. (2016). Pep-fold3: faster de novo structure prediction for linear peptides in solution and in complex. *Nucleic acids research*, **44** (W1), W449–54.

Lampson, M. and Cheeseman, I. (2011). Sensing centromere tension: Aurora b and the regulation of kinetochore function. *Trends in cell biology*, **21** (3), 133–40.

Leandro-García, L., Leskelä, S., Landa, I. n., Montero-Conde, C., López-Jiménez, E., Letón, R., Cascón, A., Robledo, M. and Rodríguez-Antona, C. (2010). Tumoral and tissue-specific expression of the major human $\beta$-tubulin isotypes. *Cytoskeleton*, **67** (4), 214–223.

Li, R. and Murray, A. W. (1991). Feedback control of mitosis in budding yeast. *Cell*, **66** (3), 519–31.

Lin, H., Herman, P. and Lakowicz, J. (2003). Fluorescence lifetime-resolved pH imaging of living cells. *Cytometry Part A*.

Liu, D., Vader, G., Vromans, M., Lampson, M. and Lens, S. (2009). Sensing chromosome bi-orientation by spatial separation of aurora b kinase from kinetochore substrates. *Science (New York, N.Y.)*, **323** (5919), 1350–3.

Magidson, V., O'Connell, C., Lončarek, J., Paul, R., Mogilner, A. and Khodjakov, A. (2011). The spatial arrangement of chromosomes during prometaphase facilitates spindle assembly. *Cell*, **146** (4), 555–567.

Mandelkow, E. M., Mandelkow, E. and Milligan, R. A. (1991). Microtubule dynamics and microtubule caps: a time-resolved cryo-electron microscopy study. *The Journal of cell biology*, **114** (5), 977–91.

McCleland, M. L., Kallio, M. J., Barrett-Wilt, G. A., Kestner, C. A., Shabanowitz, J., Hunt, D. F., Gorbsky, G. J. and Stukenberg, P. T. (2004). The vertebrate ndc80 complex contains spc24 and spc25 homologs, which are required to establish and maintain kinetochore-microtubule attachment. *Current Biology*, **14** (2), 131–137.

McEwen, B. F. and Dong, Y. (2010). Contrasting models for kinetochore microtubule attachment in mammalian cells. *Cellular and molecular life sciences: CMLS*, **67** (13), 2163–72.

—, — and VandenBeldt, K. J. (2007). Using electron microscopy to understand functional mechanisms of chromosome alignment on the mitotic spindle. *Methods in cell biology*, **79**, 259–93.

Miller, S., Johnson, M. and Stukenberg (2008). Kinetochore attachments require an interaction between unstructured tails on microtubules and ndc80(hec1). *Current biology*, **18** (22), 1785–91.

Miranda, J. J., De Wulf, P., Sorger, P. K. and Harrison, S. C. (2005). The yeast dash complex forms closed rings on microtubules. *Nature structural & molecular biology*, **12** (2), 138–43.

Mitchison, T. J. (1988). Microtubule dynamics and kinetochore function in mitosis. *Annual review of cell biology*, **4**, 527–49.

Molodtsov, M. I., Grishchuk, E. L., Efremov, A. K., McIntosh, J. R. and Ataullakhanov, F. I. (2005). Force production by depolymerizing microtubules: a theoretical study. *Proceedings of the National Academy of Sciences of the United States of America*, **102** (12), 4353–8.

Musacchio, A. and Salmon, E. (2007). The spindle-assembly checkpoint in space and time. *Nature reviews. Molecular cell biology*, **8** (5), 379–93.

Nicklas (1983). Measurements of the force produced by the mitotic spindle in anaphase. *The Journal of Cell Biology*, **97** (2), 542–548.

— and Koch (1969). Chromosome micromanipulation iii. spindle fiber tension and the reorientation of mal-oriented chromosomes.

— and Ward (1994). Elements of error correction in mitosis: microtubule capture, release, and tension.

Obuse, C., Yang, H., Nozaki, N., Goto, S., Okazaki, T. and Yoda, K. (2004). Proteomics analysis of the centromere complex from hela interphase cells: Uv-damaged dna binding protein 1 (ddb-1) is a component of the cen-complex, while bmi-1 is transiently co-localized with the centromeric region in interphase. *Genes to cells: devoted to molecular & cellular mechanisms*, **9** (2), 105–20.

Patterson and Piston (2000). Photobleaching in two-photon excitation microscopy.

Pelletier, V., Gal, N., Fournier, P. and Kilfoil, M. (2009). Microrheology of microtubule solutions and actin-microtubule composite networks. *Physical review letters*, **102** (18), 188303.

Pereira, A. M., Tudor, C., Kanger, J. S., Subramaniam, V. and Martin-Blanco, E. (2011). Integrin-dependent activation of the jnk signaling pathway by mechanical stress. *PloS one*, **6** (12), e26182.

Peter, M., SM, A., Hughes, M. and Keppler, M. (2005). Multiphoton-FLIM quantification of the EGFP-mRFP1 FRET pair for localization of membrane receptor-kinase interactions. *Biophysical journal*.

Petrásek, Z. and Schwille, P. (2008). Precise measurement of diffusion coefficients using scanning fluorescence correlation spectroscopy. *Biophysical journal*, **94** (4), 1437–48.

Posch, M., Khoudoli, G., Swift, S., King, E., DeLuca, J. and Swedlow, J. (2010). Sds22 regulates aurora b activity and microtubule–kinetochore interactions at mitosis. *The Journal of Cell Biology*, **191** (1), 61–74.

Powers, A., Franck, A., Gestaut, D., Cooper, J., Gracyzk, B., Wei, R., Wordeman, L., Davis, T. and Asbury, C. (2009). The ndc80 kinetochore complex forms load-bearing attachments to dynamic microtubule tips via biased diffusion. *Cell*, **136** (5), 865–75.

Rajagopalan, H. and Lengauer, C. (2004). Aneuploidy and cancer. *Nature*, **432** (7015), 338–341.

Ran, Hsu, P., Wright, J., Agarwala, V., Scott, D. and Zhang, F. (2013). Genome engineering using the crispr-cas9 system. *Nature protocols*, **8** (11), 2281–308.

Ripoll, C., Martin, M., Roldan, M. and Talavera, E. (2015). Intracellular zn 2+ detection with quantum dot-based FLIM nanosensors. *Chemical Communications*.

Rowley, M., Barber, P. and Coolen, A. (2011a). Bayesian analysis of fluorescence lifetime imaging data. *SPIE BiOS*.

Rowley, M. I., Barber, P. R., Coolen, A. C. and Vojnovic, B. (2011b). Bayesian analysis of fluorescence lifetime imaging data. pp. 790325–790325.

Roy, R., Hohng, S. and Ha, T. (2008). A practical guide to single-molecule FRET. *Nature Methods*, **5** (6), 507–516.

Salimian, K., Ballister, E., Smoak, E., Wood, S., Panchenko, T., Lampson, M. and Black, B. (2011). Feedback control in sensing chromosome biorientation by the aurora b kinase. *Current Biology*, **21** (13), 1158–1165.

Santaguida, S. and Amon, A. (2015). Short- and long-term effects of chromosome mis-segregation and aneuploidy. *Nature Reviews Molecular Cell Biology*, **16** (8), 473–485.

Sessa, F., Mapelli, M., Ciferri, C., Tarricone, C., Areces, L., Schneider, T., Stukenberg, T. and Musacchio, A. (2005). Mechanism of aurora b activation by incenp and inhibition by hesperadin. *Molecular Cell*, **18** (3), 379–391.

Sharman, K., Periasamy, A. and Ashworth, H. (1999). Error analysis of the rapid lifetime determination method for double-exponential decays and new windowing schemes. *Analytical Chemistry*.

Sivia, D. S. and Skilling, J. (2008). *A Bayesian Tutorial*. Oxford University Press, 2nd edn.

Slep, K. and Vale, R. (2007). Structural basis of microtubule plus end tracking by xmap215, clip-170, and eb1. *Molecular cell*.

Stachowiak, J., Schmid, E., Ryan, C. and Ann, H. (2012). Membrane bending by protein–protein crowding. *Nature cell Biology*.

Stringari, C., Cinquin, A. and Cinquin, O. (2011). Phasor approach to fluorescence lifetime microscopy distinguishes different metabolic states of germ cells in a live tissue. *Proceedings of the National Academy of Sciences of the United States of America*.

Sundin, L., Guimaraes, G. and DeLuca, J. (2011). The ndc80 complex proteins nuf2 and hec1 make distinct contributions to kinetochore–microtubule attachment in mitosis. *Molecular Biology of the Cell*, **22** (6), 759–768.

Suzuki, A., Badger, B. and Salmon, E. (2015). A quantitative description of ndc80 complex linkage to human kinetochores. *Nature Communications*, **6**, 8161.

Tan, L. and Kapoor, T. (2011). Examining the dynamics of chromosomal passenger complex (cpc)-dependent phosphorylation during cell division. *Proceedings of the National Academy of Sciences of the United States of America*, **108** (40), 16675–80.

Tanaka, T. U., Rachidi, N., Janke, C., Pereira, G., Galova, M., Schiebel, E., Stark, M. J. and Nasmyth, K. (2002). Evidence that the ipl1-sli15 (aurora kinase-incenp) complex promotes chromosome bi-orientation by altering kinetochore-spindle pole connections. *Cell*, **108** (3), 317–329.

Tauchman, E., Boehm, F. and DeLuca, J. (2015). Stable kinetochore-microtubule attachment is sufficient to silence the spindle assembly checkpoint in human cells. *Nature Communications*, **6**, 10036.

Tirnauer, J., Canman, J., Salmon and Mitchison, T. (2002). Eb1 targets to kinetochores with attached, polymerizing microtubules. *Molecular biology of the cell*, **13** (12), 4308–16.

Tran, P. T., Joshi, P. and Salmon, E. D. (1997). How tubulin subunits are lost from the shortening ends of microtubules. *Journal of structural biology*, **118** (2), 107–18.

Tsukahara, T., Tanno, Y. and Watanabe, Y. (2010). Phosphorylation of the cpc by cdk1 promotes chromosome bi-orientation. *Nature*, **467** (7316), 719–23.

Violin, J. D., Zhang, J., Tsien, R. Y. and Newton, A. C. (2003). A genetically encoded fluorescent reporter reveals oscillatory phosphorylation by protein kinase c. *The Journal of cell biology*, **161** (5), 899–909.

Wallrabe, H. and Periasamy, A. (2005). Imaging protein molecules using FRET and FLIM microscopy. *Current opinion in biotechnology*.

Wang, F., Dai, J., Daum, J. R., Niedzialkowska, E., Banerjee, B., Stukenberg, P. T., Gorbsky, G. J. and Higgins, J. M. (2010). Histone h3 thr-3 phosphorylation by haspin positions aurora b at centromeres in mitosis. *Science (New York, N.Y.)*, **330** (6001), 231–5.

—, Ulyanova, N., Daum, J., Patnaik, D., Kateneva, A., Gorbsky, G. and Higgins, J. (2012). Haspin inhibitors reveal centromeric functions of aurora b in chromosome segregation. *The Journal of Cell Biology*, **199** (2).

Wei, R., Sorger, P. and Harrison, S. (2005). Molecular organization of the ndc80 complex, an essential kinetochore component. *Proceedings of the National Academy of Sciences of the United States of America*, **102** (15), 5363–7.

Welburn, J., Grishchuk, E., Backer, C., Wilson-Kubalek, E., III, J. and Cheeseman, I. (2009). The human kinetochore ska1 complex facilitates microtubule depolymerization-coupled motility. *Developmental Cell*, **16** (3).

—, Vleugel, M., Liu, D., Yates, J., Lampson, M., Fukagawa, T. and Cheeseman, I. (2010). Aurora b phosphorylates spatially distinct targets to differentially regulate the kinetochore-microtubule interface. *Molecular Cell*, **38** (3), 383–392.

Westermann, S., Avila-Sakar, A., Wang, H.-W. W., Niederstrasser, H., Wong, J., Drubin, D. G., Nogales, E. and Barnes, G. (2005). Formation of a dynamic kinetochore-microtubule interface through assembly of the dam1 ring complex. *Molecular cell*, **17** (2), 277–90.

—, Wang, H.-W. W., Avila-Sakar, A., Drubin, D. G., Nogales, E. and Barnes, G. (2006). The dam1 kinetochore ring complex moves processively on depolymerizing microtubule ends. *Nature*, **440** (7083), 565–9.

Wigge, P. A. and Kilmartin, J. V. (2001). The ndc80p complex from saccharomyces cerevisiae contains conserved centromere components and has a function in chromosome segregation. *The Journal of cell biology*, **152** (2), 349–60.

Wilson-Kubalek, E., Cheeseman, I., Yoshioka, C., Desai, A. and Milligan, R. (2008). Orientation and structure of the ndc80 complex on the microtubule lattice. *The Journal of Cell Biology*, **182** (6), 1055–1061.

Yamagishi, Y., Honda, T., Tanno, Y. and Watanabe, Y. (2010). Two histone marks establish the inner centromere and chromosome bi-orientation. *Science (New York, N.Y.)*, **330** (6001), 239–43.

—, Yang, C.-H. H., Tanno, Y. and Watanabe, Y. (2012). Mps1/mph1 phosphorylates the kinetochore protein knl1/spc7 to recruit sac components. *Nature cell biology*, **14** (7), 746–52.

Ye, A., Deretic, J., Hoel, C., Hinman, A., Cimini, D., Welburn, J. and Maresca, T. (2015). Aurora a kinase contributes to a pole-based error correction pathway. *Current Biology*, **25** (14), 1842–1851.

Yen, T. J., Compton, D. A., Wise, D., Zinkowski, R. P., Brinkley, B. R., Earnshaw, W. C. and Cleveland, D. W. (1991). Cenp-e, a novel human centromere-associated protein required for progression from metaphase to anaphase. *The EMBO journal*, **10** (5), 1245–54.

Yoo, T. and Needleman, D. (2016). Studying kinetochores in vivo using FLIM-FRET. *The Mitotic Spindle: Methods and Protocols*, p. 169–186.

Zaytsev, A., Mick, J., Maslennikov, E., Nikashin, B., DeLuca, J. and Grishchuk, E. (2015). Multisite phosphorylation of the ndc80 complex gradually tunes its microtubule-binding affinity. *Molecular Biology of the Cell*, **26** (10), 1829–1844.

—, Segura-Peña, D., Godzi, M., Calderon, A., Ballister, E., Stamatov, R., Mayo, A., Peterson, L., Black, B., Ataullakhanov, F. and et al. (2016). Bistability of a coupled aurora b kinase-phosphatase system in cell division. *eLife*, **5**, e10644.

—, Sundin, L., DeLuca, K., Grishchuk, E. and DeLuca, J. (2014). Accurate phosphoregulation of kinetochore–microtubule affinity requires unconstrained molecular interactions. *The Journal of Cell Biology*, **206** (1), 45–59.

Zhai, Kronebusch and Borisy (1995). Kinetochore microtubule dynamics and the metaphase-anaphase transition. *The Journal of Cell Biology*, **131** (3), 721–734.

Zhang, R., Alushin, G. M., Brown, A. and Nogales, E. (2015). Mechanistic origin of microtubule dynamic instability and its modulation by eb proteins. *Cell*, **162** (4), 849–59.

Zheng, L., Chen, Y. and Lee, W.-H. (1999). Hec1p, an evolutionarily conserved coiled-coil protein, modulates chromosome segregation through interaction with smc proteins. *Molecular and Cellular Biology*, **19** (8), 5417–5428.

# Appendix A

# Appendix to Chapter 4: Supplementary Figures

## A.1 Supplementary Figures

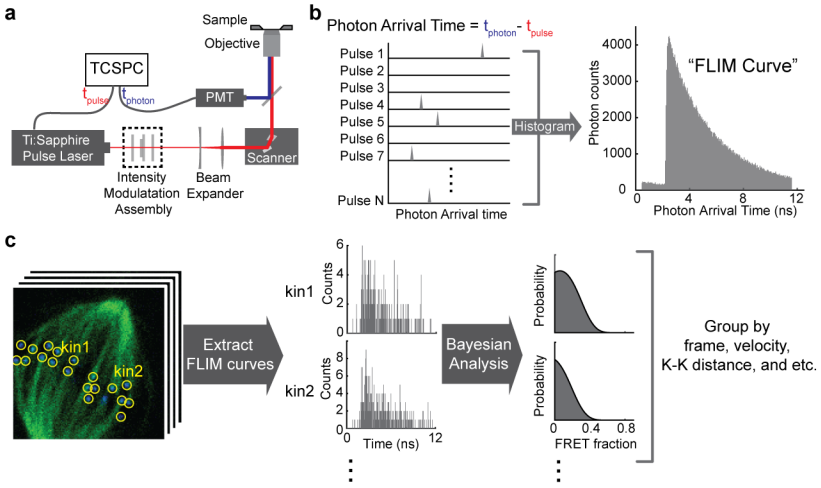


**Figure A.1:** ***Kinetochore FLIM-FRET measurement***. ***a***, *Schematic diagram of two-photon FLIM-FRET system.* ***b***, *The photon arrival time, the difference in timing between the detection of emitted photon and the generation of excitation laser pulse, is measured by time-correlated single photon counting (TCSPC) for each detected emitted photon. A FLIM curve is constructed by making a histogram of photon arrival times measured over many laser repetition periods.* ***c***, *FLIM data contains FLIM curves at each pixel, and the total photon counts in each pixel form a typical fluorescence intensity image. To quantify FRET fraction at each kinetochore, kinetochores are identified from the intensity image, then the FLIM curves are summed over the pixels within each kinetochore. The posterior distribution of the FRET fraction was computed by Bayesian inference on the FLIM curve at each kinetochore. The posterior distributions of the kinetochores in a group are combined to compute the mean and the standard deviation of the mean of the FRET fraction in the group.*

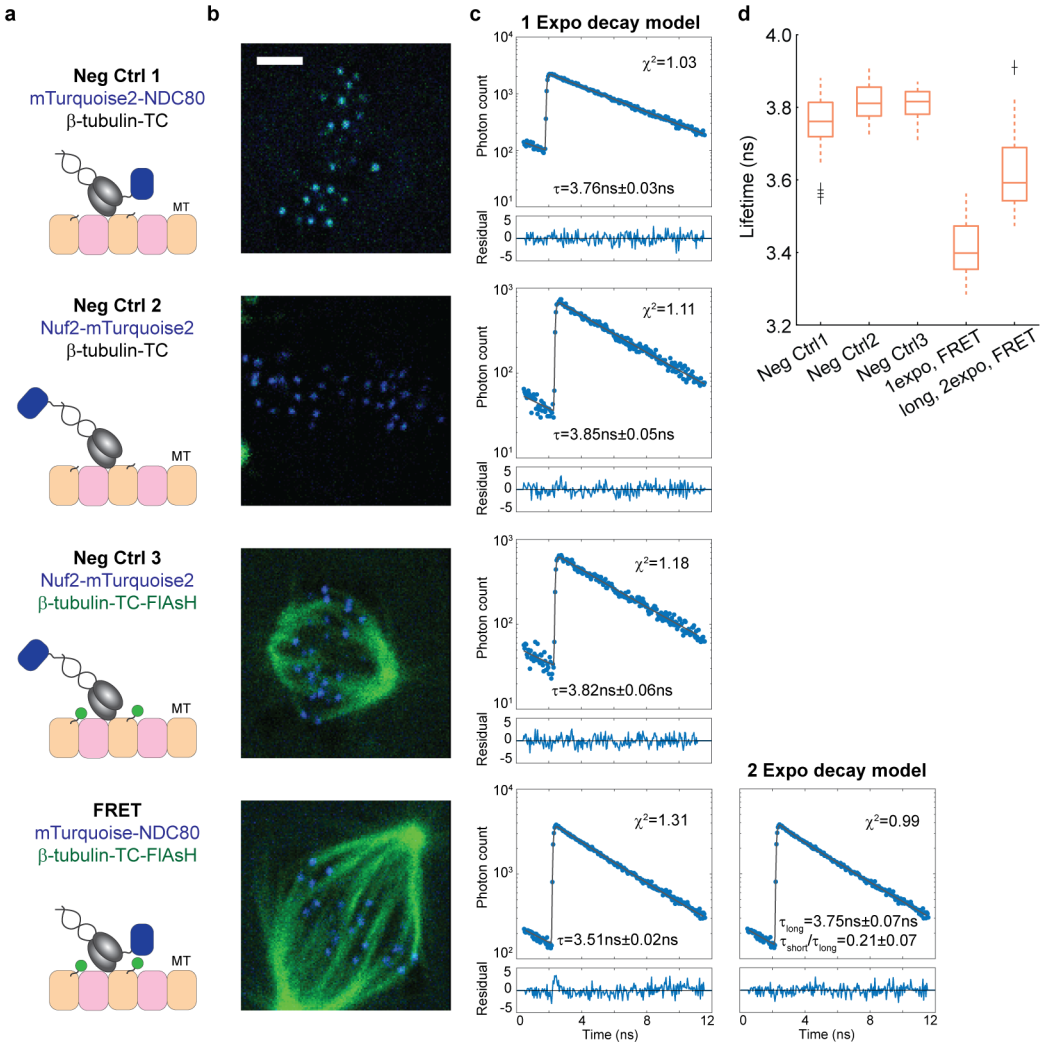


**Figure A.2:** *Negative controls for FLIM-FRET NDC80 binding measurements.* ***a****, Schematic description of three different FRET-negative control experiments and a FRET-positive experiment.* ***b****, Example cell image of each experiment. 3 µm scale bar.* ***c****, Example FLIM curves for each experiment (blue circles), the best estimated exponential model (gray line), and the associated weighted residual.* ***d****, Boxplot showing the distribution of fluorescence lifetimes estimated in each experiment. For Neg Ctrl 1 3 and 1expo, FRET, the lifetimes in the best estimated single-exponential models are reported, while for long, 2expo, FRET, the longer lifetimes in the best estimated double-exponential models are reported. $n = 32$, 11, 6, and 40 cells for Neg Ctrl 1, 2, 3, and FRET experiments, respectively.*

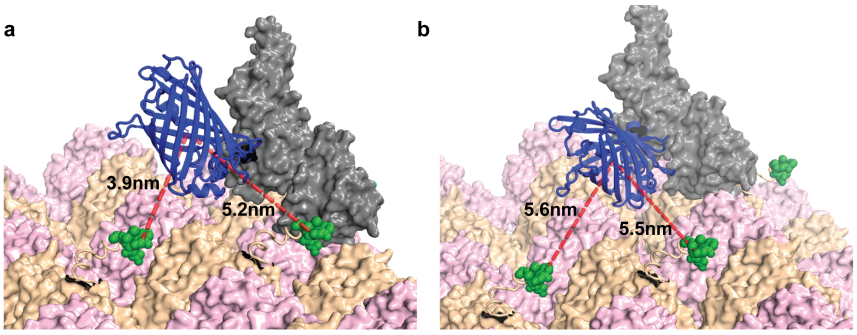


**Figure A.3:** ***Predicted distance between mTurquoise2 and TC-FlAsH***. *Predicted distances between mTurquoise2 (blue cartoon) and TC-FlAsH (green ball) when mTurquoise2-NDC80 is attached to a microtubule (pink and yellow surface) labeled with TC-FlAsH at* ***a*** *intra-dimer and* ***b*** *inter-dimer interphases.*

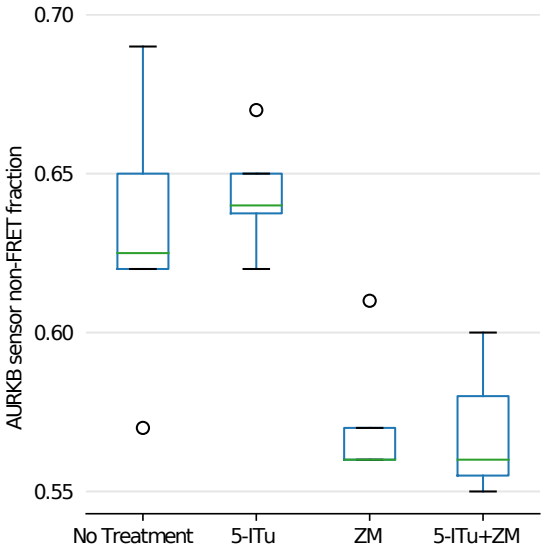


**Figure A.4:** ***The effect of haspin inhibition on Aurora B activity***. *Boxplots of the non-FRET fraction of Aurora B sensor targeted at the N-terminus of Nuf2 in untreated cells (8 cells) and the cells treated with 10 µM 5-ITu (8 cells), 3 µM ZM447439 (5 cells), and both (3 cells).*

# Appendix B

# Appendix to Chapter 4: Supplementary Text

## B.1 Measurement of the fraction of $\beta$-tubulin labeled with TC-FlAsH

To measure the fraction of $\beta$-tubulin labeled with TC-FlAsH, we sought to determine the concentration of labeled $\beta$-tubulin in the cell, and divide it by the total concentration of $\beta$-tubulin. We calculated the concentration of labeled $\beta$-tubulin by combining 3D fluorescence microscopy, to measure the total fluorescence of $\beta$-tubulin-TC-FlAsH per cell, and fluorescence correlation spectroscopy (FCS) to measure the fluorescence per molecule of TC-FlAsH.

**3D fluorescence microscopy**. We acquired z-stacks of $\beta$-tubulin-TC-FlAsH in mitotic cells using two-photon fluorescence microscopy (Supplementary Figure B.1a), and then segmented the 3D images (Supplementary Figure B.1b). Assuming that the cytoplasmic background results from FlAsH binding specifically to monomeric $\beta$-tubulin and nonspecifically to cysteine-rich proteins freely diffusing in the cytoplasm, the average number of photons emitted from $\beta$-tubulin-TC-FlAsH in microtubules is the difference between the average

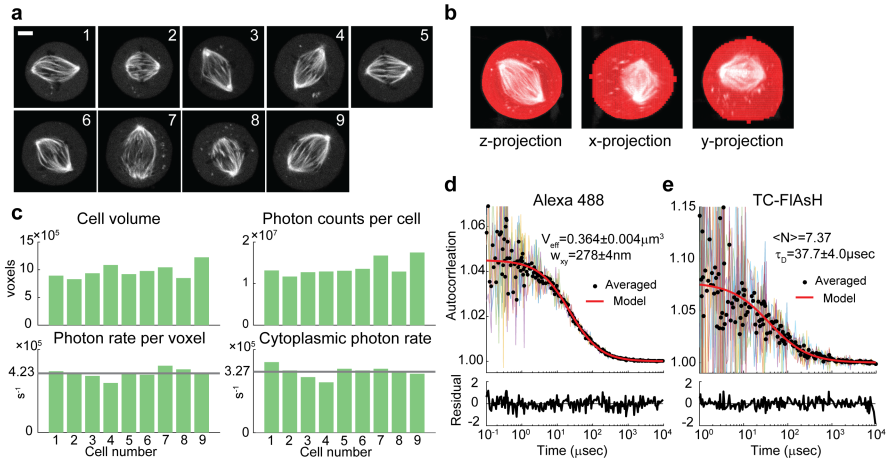


**Figure B.1:** *β-tubulin labeling fraction measurement.* ***a****, Two-photon fluorescent microscopy images of 9 mitotic cells with β-tubulin-TC-FlAsH. 5 μm scale bar.* ***b****, Example 3D segmentation.* ***c****, the number of voxels in segmented 3D cell images (top left), the total number of photons collected from entire cells (top right), the total number of photons divided by the number of voxels and the measurement time (bottom left), and the number of photons collected per second at a voxel in the cytoplasmic region (bottom right). Gray lines represent the average over the 9 different cells.* ***d*** *and* ***e****, FCS measurements on Alexa Fluor 488 and TC-FlAsH in solution, respectively. Black circles are averages over 5 or 6 autocorrelation functions, and red lines are the FCS model fit to the averages.*

photon rate throughout the entire cell (423 $\pm$ 33 ms$^{-1}$) and the average photon rate in the cytoplasm (327 $\pm$ 30 ms$^{-1}$), which is 96 $\pm$ 12 ms$^{-1}$ (Supplementary Figure B.1c).

**Fluorescence correlation spectroscopy**. To convert the measured photon rate from fluorescence microscopy to a measurement of the absolute concentration of $\beta$-tubulin-TC-FlAsH, we used two-photon FCS to determine the volume of the point spread function (PSF) and the molecular brightness (i.e. the number of photons emitted per molecule per second) of TC-FlAsH (Hess and Webb, 2002). First, we performed an FCS measurement on 97-nM Alexa Fluor 488, of which diffusion coefficient is known to be 435 $\mu$m$^2$/s (Petrásek and Schwille, 2008), and found that the effective volume of the PSF, $V_{eff}$, and the lateral beam waist, $w_{xy}$, are 0.364 $\pm$ 0.004 $\mu$m$^3$ and 278 $\pm$ 4 nm, respectively (Supplementary Figure B.1d). Then we performed an FCS measurement on a synthesized peptide labeled with TC-FlAsH, based on which the molecular brightness was estimated to be 233.4 $\pm$ 9.3 s$^{-1}$. Using the estimated molecular brightness and the effective volume of PSF, we calculated the average

concentration of the polymerized $\beta$-tubulin-TC-FlAsH to be

$$\frac{9.6 \times 10^4\ s^{-1}}{(233.4\ s^{-1})(0.364\ \mu m^3)} = 1.88\ \pm\ 0.13\ \mu M \tag{B.1}$$

**Calculating labeling ratio**. A previous study (Dumontet *et al.*, 1996) estimated the percentage of polymerized $\beta$-tubulin in a mitotic human tissue culture cell to be 36% $\pm$ 7%. Combining this information with our estimate of an average concentration of polymerized $\beta$-tubulin-TC-FlAsH of 1.88 $\pm$ 0.13 $\mu$M leads to a total concentration of $\beta$-tubulin-TC-FlAsH of 1.88 $\mu$M$\times$100/36 $\approx$ 5.22 $\pm$ 1.08 $\mu$M. Since the total concentration of tubulin dimer in a tissue culture cell is $\sim$20 $\mu$M (Hiller and Weber, 1978), we estimated the fraction of labeled $\beta$-tubulin to be 5.22 $\mu$M/20 $\mu$M $\approx$ 26.1% $\pm$ 5.4%.

## B.2 The conversion of FRET fraction to NDC80 binding fraction

The probability that the mTurquoise2-NDC80 bound to a microtubule engages in FRET with $\beta$-tubulin-TC-FlAsH depends on 1) $F_{label}$, the fraction of $\beta$-tubulins that are labeled with FlAsH, and 2) $N_{partner}$, the number of C-termini of $\beta$-tubulins in close enough proximity to the mTurquoise2 to engage in FRET. Though we obtained an estimate for $F_{label}$ as described above, we do not know the exact value of $N_{partner}$ because the conformation of the disordered C-terminal tail of $\beta$-tubulin interacting with NDC80 has not been determined, and the position and orientation of mTurquoise2 relative to NDC80 is unknown. Based on previous cryo-EM results (Alushin *et al.*, 2010), we speculate that when NDC80 is attached to a microtubule, mTurquoise2 fused to the N-terminus of Nuf2 could be within 6 nm of 1 or 2 $\beta$-tubulin C-terminal tails, regardless of whether the binding happens at the inter-dimer or intra-dimer interface (Supplementary Figure A.3). The NDC80 binding fraction that is reported throughout this paper was converted from the FRET fraction on the assumption that $N_{partner} = 1$ (i.e. 100% NDC80 binding fraction corresponds to $F_{label} = 26.1\%$ FRET fraction). If $N_{partner}$ was equal to 2, then the ratio of NDC80 binding fraction to FRET fraction would decrease by factor of 2. The conversion factor between FRET fraction and

NDC80 binding fraction is bound by measurements to be between 20:100 and 26.1:50, on the one end by our calculation of up to 100% NDC80 binding (Figure 4.2a) and on the other end by the structural information for cryo-EM. Values between these two limits would be possible if, during binding, there are significant conformation fluctuations in the C-terminal tail of $\beta$-tubulin or the mTurquoise2 connected to Nuf2.

## B.3 Supplementary Materials and Methods

# Appendix C

# List of plasmids and stable cell lines used in this work

**Table C.1:** *List of plasmids*

| Name | Backbone | Insert | Note | Antibiotics Resistance | Comment |
|---|---|---|---|---|---|
| pTY01 | pcDNA3.1 | mTurq2-FHA-Aurora B substrate-sREACh | Soluble AURKB sensor (mTurq2/sREACh from Addgene) | Amp | 11 extra residues after sREACh and before STOP codon |
| pTY02 | pcDNA3.1 | mTurq2-FHA-Aurora B substrate-sREACh-Hec1 | AURKB sensor at N-terminus of Hec1 | Amp | |
| pTY03 | pLSSmOrange-C1 (from Addgene) | CENPC (from Cheeseman Lab) | N-terminally labeled CENPC | Kan | Localization observed, though very rare |
| pTY04 | pLSSmOrange-C1 (from Addgene) | CENPH (from Cheeseman Lab) | N-terminally labeled CENPH | Kan | Couldn't observe the localization |
| pTY05 | pLSSmOrange-N1 (from Addgene) | CENPC (from Cheeseman Lab) | C-terminally labeled CENPC | Kan | LSSmOrange localized at kinetochores in mitotic cell observed, though it's very rare |
| pTY06 | pBABE-puro | CENPC-LSSmOrange (copied from pTY05) | C-terminally labeled CENPC | Amp | |
| pTY07 | pBABE-puro | LSSmOrange-CENPA (with Kozak seq) | N-terminally labeled CENPA | Amp | |
| pTY08 | pBABE-puro | mBeRFP-CENPA | N-terminally labeled CENPA | Amp | |

Continued on next page

**Table C.1:** *(continued)*

| Name | Backbone | Insert | Note | Antibiotics Resistance | Comment |
|---|---|---|---|---|---|
| pTY09 | pEGFP-C1 | CENPC (from Cheeseman Lab) | N-terminally labeled CENPC | Kan | Aggregation, mislocalization is observed for some cells. Normal localization is observed too. |
| pTY10 | pEGFP-C1 | CENPH (from Cheeseman Lab) | N-terminally labeled CENPH | Kan | Often localize with high background, weak signal at kinetochore. |
| pTY11 | pJAG98 | mTurq2-FHA-Aurora B substrate-sREACh | Soluble AURKB sensor (mTurq2/sREACh from Addgene) | Amp | |
| pTY12 | pcDNA3.1 | mTurq2-SkaI | N-terminally labled SkaI | Amp | |
| pTY13 | pcDNA3.1 | SkaI-mTurq2 | C-terminally labeled SkaI | Amp | |
| pTY14 | pLSSmOrange-N1 (from Addgene) | 9A-Hec1 | C-terminally labeled 9A-Hec1 | Kan | |
| pTY15 | pLSSmOrange-N1 (from Addgene) | 9D-Hec1 | C-terminally labeled 9D-Hec1 | Kan | |
| pTY16 | pLSSmOrange-N1 (from Addgene) | Hec1 (WT) | C-terminally labeled Hec1 | Kan | |
| pTY17 | pLSSmOrange-C1 (from Addgene) | MAD2L1 | N-terminally labeled Mad2 | Kan | |

Continued on next page

**Table C.1:** *(continued)*

| Name | Backbone | Insert | Note | Antibiotics Resistance | Comment |
|---|---|---|---|---|---|
| pTY18 | pBABE-puro | sfGFP-CENPA | N-terminally labeled CENPA | Amp | |
| pTY19 | pBABE-puro | CENPH-LSSmOrange | C-terminally labeled CENPH | Amp | |
| pTY20 | pBABE-puro | LSSmOrange-CENPA (without Kozak seq) | N-terminally labeled CENPA (without Kozak) | Amp | |
| pTY21 | pBABE-puro | hmKeima8.5-CENPA | N-terminally labeled CENPA | Amp | hmKeima8.5 from Shah group |
| pTY22 | pmTFP1.0-C1 | Ran | N-terminally labeled Ran | Kan | |
| pTY23 | phmKeima8.5-C1 | importin beta | N-terminally labeled importin beta | Kan | |
| pTY24 | pmTFP1.0-C1 | Linker-hmKeima8.5 | mTFP1.0-Linker-hmKeima8.5 (for dual color FCS control) | Kan | |
| pTY25 | phmKeima8.5-C1 | importin alpha | N-terminally labeled importin alpha | Kan | |
| pTY26 | phmKeima8.5-C1 | RanGAP | N-terminally labeled RanGAP | Kan | |

Continued on next page

**Table C.1:** *(continued)*

| Name | Backbone | Insert | Note | Antibiotics Resistance | Comment |
|---|---|---|---|---|---|
| pTY27 | phmKeima8.5-C1 | RanBP1 | N-terminally labeled RanBP1 | Kan | |
| pTY28 | phmKeima8.5-C1 | Aurora B | N-terminally labeled Aurora B | Kan | |
| pTY29 | psfGFP-C1 | Aurora B | N-terminally labeled Aurora B | Kan | |
| pTY30 | phmKeima8.5-C1 | Ran | N-terminally labeled Ran | Kan | |
| pTY31 | pLSSmOrange-C1 (from Addgene) | Aurora B | N-terminally labeled Aurora B | Kan | |
| pTY32 | pmTFP1.0-C1 | importin alpha | N-terminally labeled importin alpha | Kan | |
| pTY33 | pmTFP1.0-C1 | RanGAP | N-terminally labeled RanGAP | Kan | |
| pTY34 | pmTFP1.0-C1 | RanBP1 | N-terminally labeled RanBP1 | Kan | |
| pTY35 | phmKeima8.5-C1 | Aurora B 4KEN6->AAN | N-terminally labeled Aurora B with KEN->AAN | Kan | |

Continued on next page

**Table C.1:** *(continued)*

| Name | Backbone | Insert | Note | Antibiotics Resistance | Comment |
|---|---|---|---|---|---|
| pTY36 | phmKeima8.5-C1 | Aurora B 26QRVL29->AAAA | N-terminally labeled Aurora B with 26QRVL29->AAAA | Kan | |
| pTY37 | psfGFP-C1 | Aurora B 4KEN6->AAN | N-terminally labeled Aurora B with KEN->AAN | Kan | |
| pTY38 | psfGFP-C1 | Aurora B 26QRVL29->AAAA | N-terminally labeled Aurora B with 26QRVL29->AAAA | Kan | |
| pTY39 | pBABE-puro | sfGFP-H2A | N-terminally labeled H2A | Amp | |
| pTY40 | pBABE-puro | EGFP-hCentrin2 | N-terminally labeled human centrin 2 | Amp | |
| pTY41 | pcDNA | Plk1 FRET sensor (from Addgene) | Plk1 FRET sensor c-jun substrate, | Amp | based on http://www.addgene.org/45203/ |
| pTY42 | pJAG98 | mTagRFP-T-alpha-tubulin | N-terminally labeled alpha tubulin (TUBA1B) | Amp | |
| pTY43 | pBABE-hygro | Halo-H2A | N-terminally labeled Histone A | Amp | |

Continued on next page

**Table C.1:** *(continued)*

| Name | Backbone | Insert | Note | Antibiotics Resistance | Comment |
|---|---|---|---|---|---|
| pTY44 | pBABE-hygro | Halo-TUBB | N-terminally labeled TUBB (mouse gene) | Amp | |
| pTY45 | pBABE-hygro | Halo-alpha-tubulin | N-terminally labeled alpha tubulin (TUBA1B) | Amp | |
| pTY46 | pBABE-hygro | EGFP-hCentrin2 | N-terminally labeled human centrin 2 | Amp | |
| pTY47 | pBABE-hygro | TH-PanCen-HaloTag | TALEColor-Pan-Centromere-Halo | Amp | based on TH-PanCen-mVenus from Addgene (https://www.addgene.org/49640/) |
| pTY48 | pBABE-hygro | SNAPtag-alpha-tubulin | SNAPtag-alpha-tubulin | Amp | based on pSNAPf-C1-tubulin from Addgene (https://www.addgene.org/58197/) |
| pTY49 | pmCherry-C1 | Borealin | Borealin N-terminally labeled with mCherry | Kan | Borealin copied from pIC247 (addgene) |
| pTY50 | pJAG98 | TagRFP-T-Borealin | Borealin N-terminally labeled with TagRFP-T | Amp | |
| pTY51 | pcDNA4 | TH-PanCen-HaloTag | TALEColor-Pan-Centromere-Halo | Amp | |

Continued on next page

**Table C.1:** *(continued)*

| Name | Backbone | Insert | Note | Antibiotics Resistance | Comment |
|---|---|---|---|---|---|
| pTY52 | mTurquoise2-C1 | Hec1 (WT) | N-terminally labeled Hec1 (WT) | Kan | |
| pTY53 | mTurquoise2-C1 | Nuf2 | N-terminally labeled Nuf2 | Kan | |
| pTY54 | pcDNA3.1 | mTurq2-FHA-Aurora B substrate-YPet-Nuf2 | N-terminally labeled Nuf2 | Amp | |
| pTY55 | pcDNA5/FRT/TO (from addgene) | Hec1-EGFP | C-terminally labeled WT Hec1 | Amp | |
| pTY56 | pcDNA5/FRT/TO (from addgene) | 9A-Hec1-EGFP | C-terminally labeled 9A-Hec1 | Amp | |
| pTY57 | pcDNA5/FRT/TO (from addgene) | 9D-Hec1-EGFP | C-terminally labeled 9D-Hec1 | Amp | |
| pTY58 | pcDNA5/FRT/TO (from addgene) | S8,62D-Hec1-EGFP | C-terminally labeled S8,62D-Hec1 | Amp | |
| pTY59 | pcDNA5/FRT/TO (from addgene) | S15D-Hec1-EGFP | C-terminally labeled S15D-Hec1 | Amp | |
| pTY60 | pJAG98 | mEOS3.2-alpha-tubulin | N-terminally labeled alpha tubulin (TUBA1B) | Amp | |

Continued on next page

**Table C.1:** *(continued)*

| Name | Backbone | Insert | Note | Antibiotics Resistance | Comment |
|---|---|---|---|---|---|
| pTY61 | pJAG98 | mMaple3-alpha-tubulin | N-terminally labeled alpha tubulin (TUBA1B) | Amp | |
| pTY62 | pJAG98 | Dendra2-alpha-tubulin | N-terminally labeled alpha tubulin (TUBA1B) | Amp | |
| pTY63 | pcDNA3.1 | mEOS3.2-alpha-tubulin | N-terminally labeled alpha tubulin (TUBA1B) | Amp | |
| pTY64 | pcDNA3.1 | mMaple3-alpha-tubulin | N-terminally labeled alpha tubulin (TUBA1B) | Amp | |
| pTY65 | pcDNA3.1 | Dendra2-alpha-tubulin | N-terminally labeled alpha tubulin (TUBA1B) | Amp | |

**Table C.2:** *List of stable cell lines*

| Name | Cell Type | Selection Marker | Note |
|---|---|---|---|
| cTY01 | U2OS | Blast, Puro, Hygro | TUBB-TC CRISPR (cTY20)+ mTurquiose2-Nuf2_blast/puro/hygro polyclonal |
| cTY02 | U2OS | Puro | LSSmOrange-CENPA polyclonal |
| cTY03 | U2OS | Puro | CENPC-LSSmOrange polyclonal |
| cTY04 | U2OS | Blast, Puro | cTY02 + mTurquiose2-FHA2-AURKB substrate-sREACh biosensor (pTY11) |
| cTY05 | U2OS | Blast, Puro | mTurq2-FHA2-AURKB substrate-YPet biosensor (polyclonal, Blast) + LSSmOrange-CENPA (pTY07) |
| cTY06 | U2OS | Blast, Puro | mTurq2-FHA2-AURKB substrate-YPet biosensor T417A (polyclonal, Blast) + LSSmOrange-CENPA (pTY07) |
| cTY07 | U2OS | Puro | sfGFP-CENPA (pTY18) |
| cTY08 | U2OS | Puro | hmKeima8.5-CENPA polyclonal |
| cTY09 | U2OS | Puro | mCherry-alpha-tubulin + sfGFP-CENPA (pTY18) |
| cTY10 | U2OS | Puro | EGFP-H2A (pTY39) |
| cTY11 | U2OS | Puro | mCherry-alpha-tubulin + EGFP-H2A (pTY39) |
| cTY12 | U2OS | Puro | EGFP-hCentrin2 (pTY40) |

Continued on next page

**Table C.2:** *(continued)*

| Name | Cell Type | Selection Marker | Note |
|---|---|---|---|
| cTY13 | U2OS | Puro | mCherry-alpha-tubulin + EGFP-hCentrin2 (pTY40) |
| cTY14 | U2OS | Blast | TUBB-TC CRISPR + mTurquiose2-Nuf2_blast polyclonal |
| cTY14H20,30 | U2OS | Blast | TUBB-TC CRISPR + mTurquiose2-Nuf2_blast polyclonal, selected in 20ug/ml or 30ug/ml Blast for >2 weeks |
| cTY15 | U2OS | Puro, Blast, Hygro | sfGFP-CENPA (pTY18) + mTagRFP-T-alpha-tubulin (pTY42) + Halo-H2A (pTY43) |
| cTY20 | U2OS | none | TUBB-TC CRISPR, sgRNA #9 line 11, monoclonal |
| cTY21 | U2OS | Puro, Hygro | mCherry-alpha-tubulin + sfGFP-CENPA (pTY18) + EGFP-hCentrin2 (pTY46) |
| cTY22 | U2OS | Puro, Hygro | mCherry-alpha-tubulin + EGFP-H2A (pTY39) + EGFP-hCentrin2 (pTY46) |
| cTY23 | U2OS | Hygro | SNAPtag-alpha-tubulin (pTY48) |
| cTY24 | U2OS | Puro, Hygro | sfGFP-CENPA (pTY18) + SNAPtag-alpha-tubulin (pTY48) |
| cTY25 | U2OS | Puro, Blast, Hygro | sfGFP-CENPA (pTY18) + mTagRFP-T-alpha-tubulin (pTY42) + SNAPtag-alpha-tubulin (pTY48) |
| cTY27 | U2OS | none | TUBB-TC CRISPR line + mTurq2-Nuf2 CRISPR (poly) (very low fraction of positive cells) |